10/28-94 8S(1)
12

**CONTRACTOR REPORT**

SAND93—7109
Unlimited Release
UC—814

**Yucca Mountain Site Characterization Project**

# Development of Models for Fast Fluid Pathways Through Unsaturated Heterogeneous Porous Media

Thomas H. Robey
Spectra Research Institute
1613 University Blvd., NE
Albuquerque, NM 87102

Prepared by Sandia National Laboratories Albuquerque, New Mexico 87185 and Livermore, California 94550 for the United States Department of Energy under Contract DE-AC04-94AL85000

Printed November 1994

"Prepared by Yucca Mountain Site Characterization Project (YMSCP) participants as part of the Civilian Radioactive Waste Management Program (CRWM). The YMSCP is managed by the Yucca Mountain Project Office of the U.S. Department of Energy, DOE Field Office, Nevada (DOE/NV). YMSCP work is sponsored by the Office of Geologic Repositories (OGR) of the DOE Office of Civilian Radioactive Waste Management (OCRWM)."

Issued by Sandia National Laboratories, operated for the United States Department of Energy by Sandia Corporation.



Available to DOE and DOE contractors from
Office of Scientific and Technical Information
PO Box 62
Oak Ridge, TN 37831

Prices available from (615) 576-8401, FTS 626-8401

Available to the public from
National Technical Information Service
US Department of Commerce
5285 Port Royal Rd
Springfield, VA 22161

NTIS price codes
Printed copy: A06
Microfiche copy: A01

SAND93-7109
Unlimited Release
Printed November 1994

Distribution
Category UC-814

# Development of Models for Fast Fluid Pathways Through Unsaturated Heterogeneous Porous Media

Thomas H. Robey
Spectra Research Institute
1613 University Blvd., NE
Albuquerque, NM 87102

Abstract

Geologic systems are inherently heterogeneous systems. Heterogeneity plays an important role in scaling, creating regions of local saturation and channeling flow. Previous modeling efforts of unsaturated flow at Yucca Mountain have used homogeneous models. This report examines heterogeneity and develops two-dimensional numerical methods that may be appropriate for calculation of ground water travel times. Numerical methods investigated include geostatistics, adaptive grids, upscaling and flow modeling. The numerical approaches are tested in a model predicting volumetric water contents at USW UZ-16 for the Yucca Mountain test case of the INTRAVAL project. The predicted values of volumetric water content generally compare well with the measured volumetric water contents. Inclusion of heterogeneity in the two-dimensional models results in regions of local saturation; such regions could result in channeling and fast paths important to ground water travel time analyses. This report forms the technical basis for a two-dimensional heterogeneous model to be used in future ground water travel time studies.

This report was prepared under the Yucca Mountain Project WBS number 1.2.5.4.4. The data in this report was not subject to QA controls since it is part of the INTRAVAL project.

# Acknowledgments

The modeling efforts at Sandia National Laboratories for the INTRAVAL project involved several people: Christopher Rautman provided much of the guidance for geostatistics, Sharon Shannon created many of the graphics appearing in this report, and Paul Kaplan initiated the effort and, through many discussions, helped focus the ideas. Also, Mario Martinez, George Perkins and Ralston Barnard provided advice in the writing of this document.

# Contents

# Illustrations

# Tables

# Introduction

## Purpose

The pre-waste-emplacement ground water travel time requirement is a regulatory criterion that specifies ground water travel time to the accessible environment shall be greater than 1,000 years. The Nuclear Regulatory Commission (1983) regulation states that "The geologic repository shall be located so that pre-waste-emplacement groundwater travel time along the fastest path of likely radionuclide travel from the disturbed zone to the accessible environment shall be at least 1,000 years or such other travel time as may be approved or specified by the Commission." A review of the implications of the ground water travel time regulations is given in Kaplan, *et al.* (1989). Satisfying the ground water travel time criterion for the potential repository at Yucca Mountain requires the study of fast travel path formation in the unsaturated zone and development of models that simulate the formation of fast paths.

Conceptual models for unsaturated flow that have been used for total-systems performance assessment generally fall into the categories of composite-porosity or fracture models. The composite-porosity models are based on the assumption of local capillary pressure equilibrium in the rock matrix and fractures (Peters and Klavetter, 1988). With the current magnitude of flux thought to occur at Yucca Mountain, composite-porosity models exhibit matrix-dominated flow and slow travel times (Barnard, *et al.*, 1991). Fracture-flow models (Gauthier, *et al.*, 1992 and Nitao and Buscheck, 1991) can exhibit very fast travel times but either ignore imbibition of water into the matrix or require an unrealistic supply of water at the upper boundary. The actual hydrologic conditions at Yucca Mountain are thought to lie somewhere between the extremes of these two types of models. The current study considers the effects of heterogeneities on composite-porosity models and seeks to develop numerical methods (and models) that can produce locally saturated zones where fracture flow can occur. The credibility of the model and numerical methods is investigated by using test data from the INTRAVAL project (Swedish Nuclear Inspectorate, 1992) to attempt to predict in-situ volumetric water content at specific locations in Yucca Mountain. Work based on the numerical methods presented in this study is eventually intended to allow the calculation of ground water travel times in heterogeneous media.

Prior ground water travel time calculations (Kaplan, 1993) used one-dimensional models to describe the flow at Yucca Mountain. Although one-dimensional calculations are useful

due to their speed and utility in sensitivity analyses, the lack of a lateral dimension often forces the flow through less permeable materials or into fractures in an unrealistic manner. It is difficult, if not impossible, to include heterogenities into one-dimensional calculations. Two-dimensional calculations provide a lateral dimension and alternate flow paths. While it may eventually be necessary to perform three-dimensional calculations, reasonable boundary conditions are difficult to obtain and the larger elements required to make three-dimensional calculations computationally feasible would make resolution of some of the geologic structure and physical processes more difficult. Thus, the effects of heterogeneities are considered in terms of two dimensional flow models.

Uniformity of material properties in a unit suppresses preferential pathways and tends to make two-dimensional calculations appear one-dimensional. Heterogeneity is a fundamental part of the physical processes investigated since it allows development of preferential pathways that are important in two-dimensional calculations. These pathways or channels are important because of the nonlinear nature of unsaturated flow. For example, studies of the influence of obstructions on meter-scale models shows that for some regions of the moisture retention curve the average flux is nearly independent of the obstruction size (Eaton, 1993), which implies a substantial decrease in travel times as the obstruction size increases. Channeling may allow fast transport and is also important in initiating fracture flow. Fast transport, which may imply failure to meet the ground water travel time criterion, is unlikely under uniform flow, so it is important to allow, and not suppress, channeling in the model if performance is to be evaluated. Studies involving meter-scale models of heterogeneity show that for a 50% simple binary mix, the travel times may vary as much as a factor of 8 due to channeling (Eaton, 1993). Although Eaton concludes that an effective conductivity can be obtained, then only the average flux is calculated. Average flux is useful in calculation of cumulative releases, but may greatly underestimate mechanical dispersion which is important in dose calculations. For ground water travel time an average flux is of little use in ascertaining fast paths.

Three aspects of heterogeneity are considered: location of hydrogeologic unit boundaries, intraformational variation of hydrologic properties, and variation of hydrologic properties due to scale. The geometry of the boundaries of the hydrogeologic units cannot be captured in one dimension, yet this geometry is very important to the flow in two dimensions. Because of lack of knowledge of unit boundaries at locations other than drill holes, it may also be important to include geometric uncertainty in the flow models. Variation of hydrologic parameters is based almost entirely on data collected at Yucca Mountain. Linear

correlations between hydrologic parameters are used to model heterogeneities as realistically as possible. Heterogeneity also introduces the problem of scale into the model. Upscaling methods are used for deriving hydrologic property values at the computational scale from the small core scale measurements at which the data were acquired.

Developing a model for flow in unsaturated heterogeneous media at Yucca Mountain requires the development of numerical methods to carry out the modeling. Introducing heterogeneity poses problems for flow codes currently used on Yucca Mountain. To describe the geometry of the hydrogeologic boundaries and intraformational heterogeneities, adaptive grids are required that often can be quite distorted. In addition, every element will have different properties which creates problems for typical flow codes that require clustering of nodes or elements near material interfaces. Most flow codes based on capillary pressure as the primary variable require clustering of nodes or elements near channeling, which is difficult when local zones of saturation are not known *a priori*. Flow codes developed for the current work are based on the dual variable (Darcy fluxes) and avoid the latter two problems without clustering of nodes or elements.

## Numerical Methods for Heterogeneous Media

Geostatistical methods are used to model the location of hydrogeologic boundaries in a systematic fashion that is consistent with the data. Several realizations of the hydrogeologic units are constructed, which allows geologic uncertainty to be assessed. The geometry may serve to focus the flow and determine where lateral flow is forced downward through less permeable layers.

Porosity is chosen as the fundamental hydrologic property. Probability distribution functions are constructed for the hydrogeologic units or subunits. A deterministic trend is also added into the model for one subunit. Most of the rest of the hydrologic properties are generated using linear correlations with porosity.

The flow grid employed is coarser than the detailed grid used for geostatistics and generation of material properties. In order to allow the geometry of the hydrogeologic units to be captured by the flow grid, an adaptive grid is used. The adapted grid is fitted using the criterion of minimizing heterogeneity. Porosity is used in the measure of heterogeneity, although the technique can easily be extended to other hydrologic properties, such as saturated hydraulic conductivity, or combinations of hydrologic properties. Minimizing heterogeneity within flow elements allows the geometry to be captured and also reduces the errors in upscaling the hydrologic properties from the geostatistical grid to the flow grid.

## INTRAVAL Test Problem

Simple homogeneous test problems have been found to be of limited usefulness in developing numerical methods for heterogeneous porous media. Modeling of simple problems does not allow adequate allow testing of numerical approaches for nonlinearity, channeling and scaling parameters from laboratory to computational dimensions. For example, an adaptive grid that minimizes heterogeneity within elements is difficult to test on homogeneous problems. Heterogeneous problems are inherently complex and the different numerical methods are interdependent and cannot be easily tested alone. An example is that testing a numerical flow code designed for heterogeneous media requires a numerical method for adequately generating heterogeneous domains. Another example is that different aspects of heterogeneity cannot be evaluated for sensitivity unless numerical flow simulations and travel time calculations are available for heterogeneous media. Prior ground water travel time analyses (Kaplan, 1993 and Prindle and Hopkins, 1990) used simple homogeneous domains. The Yucca Mountain test case of INTRAVAL (discussed more fully below) offers an opportunity to use an extensive data set to investigate both the data uncertainty and heterogeneity issues.

The models employed emphasize wherever possible the use of data that actually can be measured. The resulting models are then testable in that data can be collected that prove or disprove the components of the models. For example, it is difficult and perhaps impossible to measure flux; thus the models are based on saturation data for the boundary conditions.

Two test problems are included in the Yucca Mountain test case. The first problem is intended for calibration of the models employed by the participants and is thus referred to as the calibration problem. As mentioned above, the models employed in this study use saturations for boundary conditions and thus they do not have to be calibrated by adjusting the infiltration flux. The calibration problem covers only a small region which is useful for initial development and testing of the numerical approaches.

The second test problem included in the Yucca Mountain test case involves the prediction of volumetric water contents at drill hole USW UZ-16 and is called the INTRAVAL problem. The model domain used in this study is a full two-dimensional cross section running from Ghost Dance fault on the west to Bow Ridge fault on the east. Although prediction of volumetric water contents is a simpler task than travel times, volumetric water content describes the hydrologic state of the tuffs and thus is a necessary condition for developing an adequate model that can eventually be used in ground water travel time

calculations. The results show that the heterogeneous models can reasonably simulate in-situ volumetric water contents.

## INTRAVAL Data

INTRAVAL is an international cooperative project focusing on evaluation of conceptual and mathematical models for ground water flow and transport in the context of performance assessment of geologic repositories. INTRAVAL consists of many test cases and involves 26 participating parties from 12 countries and 11 field experiments. The primary objective of INTRAVAL is to increase scientific confidence in approaches to modeling flow and transport in a variety of geologic settings. The first phase began in October 1987, consisting of both numerical modeling and experimental work. The results of the first phase, completed in September 1990, showed a need for closer collaboration between experiments and models. The second phase began in October 1990 with modelers attempting to predict the results of experiments. Comparisons of predictions with laboratory or field measurements are used to evaluate the current scientific understanding of flow and transport and the conceptual models employed.

The INTRAVAL data for the Yucca Mountain test case consisted of four data sets and the final release of data from USW UZ-16. There was a great deal of interaction between the U. S. Geological Survey (USGS) and other participants regarding usefulness of issued data and desired data. Review of the data by the modelers led to some of the data being measured again using a different laboratory technique. Also, the interaction among modelers and experimentalists identified additional data needs beyond the initial data sets. The USGS, where possible, augmented the data sets to respond to the needs of the modelers. The data sets were released for use by participants in the Yucca Mountain test case but are considered preliminary. Much of the data may eventually be officially released in a similar form for use by the Yucca Mountain project.

The first data set was released on June 15, 1992 (Voss, 1992a). Data from a composite surface transect were provided that covered surficial samples from all stratigraphic units likely to be needed for modeling. Rock matrix properties provided were bulk density, porosity available to water, particle density, saturated conductivity, relative-humidity-dried sorptivity (sorptivity of a sample after it has been dried by long exposure to low humidity) and moisture retention data. Additional data were provided from three drill holes. Properties from USW GU-3 were bulk density, porosity, particle density and relative-humidity-dried sorptivity. Drill holes USW UZN-54 and USW UZN-55 provided data using both relative-humidity-

drying and 105°C oven-drying. The properties measured were bulk density, porosity, particle density, in-situ volumetric water content, and in-situ saturation (calculated). The lithology was also provided. Also, the predicted stratigraphy for USW UZ-16 was included in the data set.

The second data set was released October 30, 1992 (Voss, 1992b). A map was provided of topographic regions thought to have different infiltration properties. An addition was provided to the composite transect consisting of sorptivity measured at a higher saturation value. For vitric caprock in the composite transect, porosity, particle density and bulk density were provided. Data from USW UZN-53 were provided with the same properties measured as for USW UZN-54 and USW UZN-55.

The third data set was released on February 15, 1993 (Voss, 1993a). The moisture retention data for the composite transect were redone in response to criticism regarding lack of data at higher suction pressures. Also, property data were provided for USW UZN-53 for 11 additional core samples.

The fourth data set was released on June 23, 1993 (Voss, 1993b). These data were from USW UZ-16 and included bulk density, porosity and particle density. Also, the lithology was included. The stratigraphy differed significantly from the predicted stratigraphy by including a significant section of Prow Pass. On August 3, 1993 the final data set was released (Voss, 1993c). These data provided the in-situ volumetric water content and in-situ saturation (calculated) for USW UZ-16.

## Overview

A schematic outline of the modeling process used in this study is shown in Figure 1. In the modeling process, two-dimensional heterogeneous numerical models are developed and applied to an INTRAVAL test problem. The process begins by using geostatistical methods to generate simulations of the stratigraphy at Yucca Mountain. Then the stratigraphic units assigned to the grid nodes are used to randomly generate the corresponding porosities using the appropriate probability distribution. For the calibration problem, geostatistical methods are used to directly generate porosities. Observed correlations of matrix porosity with the rest of the material property data are then used to generate the material properties. A two-dimensional flow grid is overlaid on the cross section of porosity and adapted to the cross section to minimize heterogeneity within each element. Element matrix properties are obtained by upscaling the properties from the smaller scale used for geostatistics. The final step is application of a flow code designed to model unsaturated heterogeneous flow.

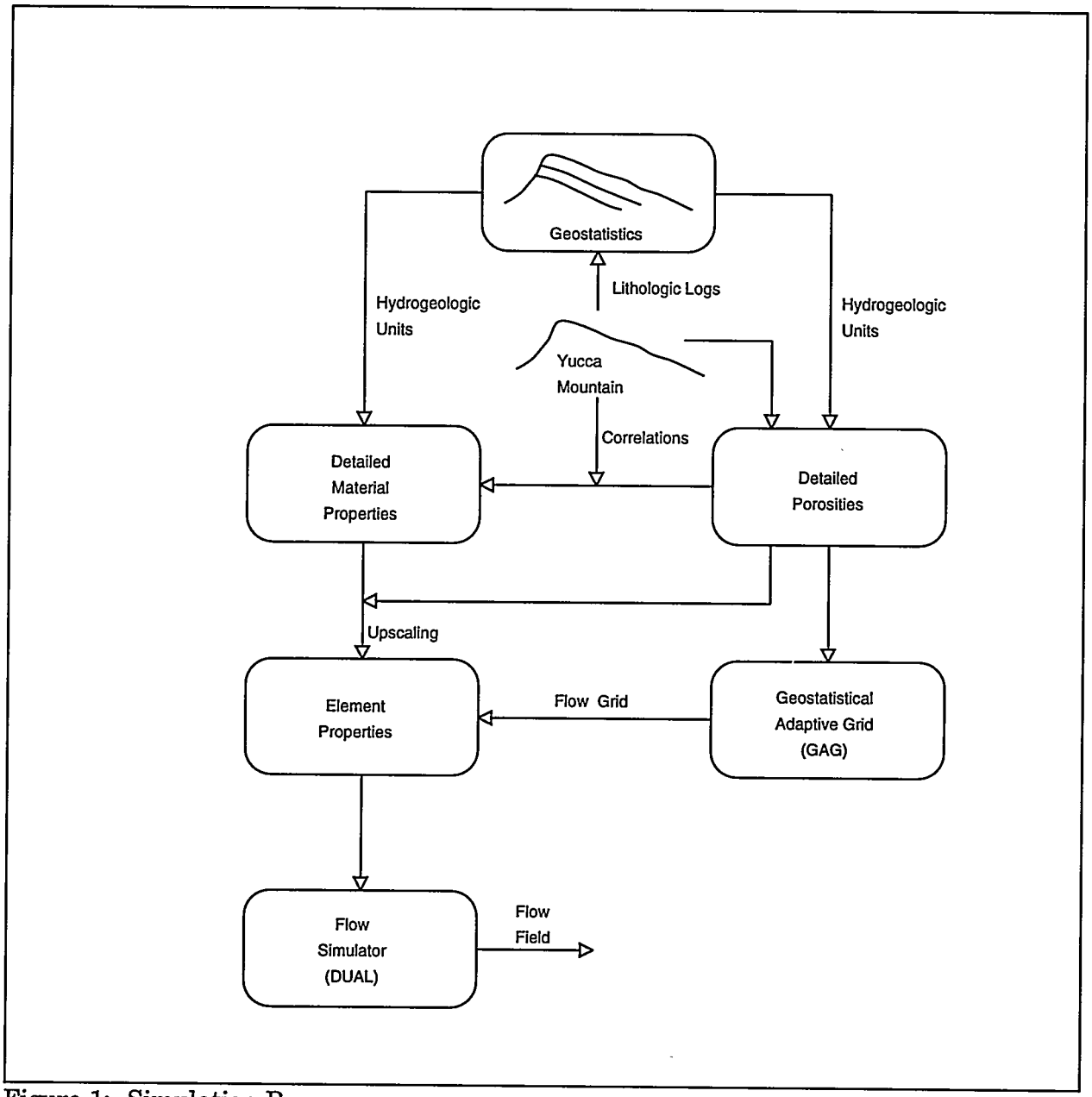


Figure 1: Simulation Process

# Geostatistical Simulation

Data from Yucca Mountain generally are obtained from drill holes that are sparsely distributed on and around the mountain. The data from these drill holes convey information about likely values of properties at nearby points. The **range**, or **correlation length**, is the distance over which the data convey information; i.e., the uncertainty in the derived properties increases with distance from the measurement location to a maximum uncertainty associated with the distribution of possible values far from any data. The range, in general, is not isotropic but, in three dimensions, is described by two anisotropy ratios and three angles. Also required in a model of spatial continuity is a function describing how the influence of the data deteriorates as the distance varies from 0 to the range.

**Kriging** uses the above model of spatial continuity and the data to arrive at the most likely values for the properties at each node of a specified grid. The kriging process tends to average values and underestimates heterogeneity (Journel and Alabert, 1989). In contrast, **geostatistical simulation** constructs a probability density function based on a model of spatial continuity and the data and then randomly samples to determine properties over a specified grid. Simulation produces more realistic heterogeneity in the simulated values than kriging and can easily produce multiple realizations that are equally probable given the input information. Thus geological uncertainty can be incorporated by using a Monte Carlo approach.

Geostatistical simulation begins by choosing the property to be simulated. Two types of properties are considered: quantitative properties such as laboratory measurements of hydrologic properties on core samples and qualitative properties such as lithologic log descriptions of core. Sequential Gaussian simulation is selected for use with quantitative properties. For qualitative properties, sequential indicator simulation is used (Deutsch and Journel, 1992).

The second step is defining a grid for the geostatistical simulation. The grid ideally should be of a similar scale as that of the data for the hydrologic properties. Computational limits still require some difference in the geostatistical scale and core scale but the potential changes in hydrologic properties are much less than assuming core scale properties directly apply at the computational flow scale. Also, the size of geologic features should be considered in order that the grid can resolve those features.

The next step is to construct a model of spatial continuity. If there are sufficiently detailed data, then the model can be matched to the data. If sufficient data are unavailable, then deterministic models (models expressing the expected values of a property) may be another source to obtain a spatial continuity model.

Next, the simulation is done by sampling all points in the grid. Both the Gaussian and indicator simulations are sequential in order that the problem is computationally feasible. A sequential simulation chooses a random path through the geostatistical grid. Then for each node, a search is conducted for nearby data and a probability density function is constructed based on the model for spatial continuity. The probability density function is then randomly sampled to determine the value or category assigned to the node which then becomes part of the data.

## Sequential Gaussian Simulation

The quantitative property chosen for geostatistical simulation is porosity since it is a commonly measured hydrologic property. The correlation length for porosity is a few hundred meters (Rautman and Flint, 1992). Thus, sequential Gaussian simulation is appropriate for regions where data are separated at most on the order of a few hundred meters. Gaussian simulation allows for detailed spatial resolution of the geologic structure and excels at complicated structures.

The INTRAVAL calibration problem, where in-situ saturations are provided for calibrating the models, involves two drill holes (USW UZN-54 and USW UZN-55) in the southeastern portion of Yucca Mountain, as shown in Figure 2. The drill holes are located 70.5 meters apart parallel to the predominant strike of the Yucca Mountain units; defining a north-south cross section. The southern drill hole, USW UZN-54, is located in the alluvium of a wash. The northern drill hole, USW UZN-55, is located on the adjacent south-facing sideslope.

The two drill holes are 70 to 80 meters in depth penetrating the welded and nonwelded tuffs of the Miocene Paintbrush Tuff as shown in Figure 3. The uppermost tuff is from the welded Tiva Canyon member. It is underlain by a series of bedded and nonwelded tuffs that are referred to as the Paintbrush nonwelded interval. The drill holes end in the welded Topopah Spring member.

Hydraulic properties were measured in the laboratory on core collected from the two drill holes on average intervals of less than a meter. Thus, detailed vertical porosity profiles are available at two locations as shown in Figure 4. Since the calibration cross section is less

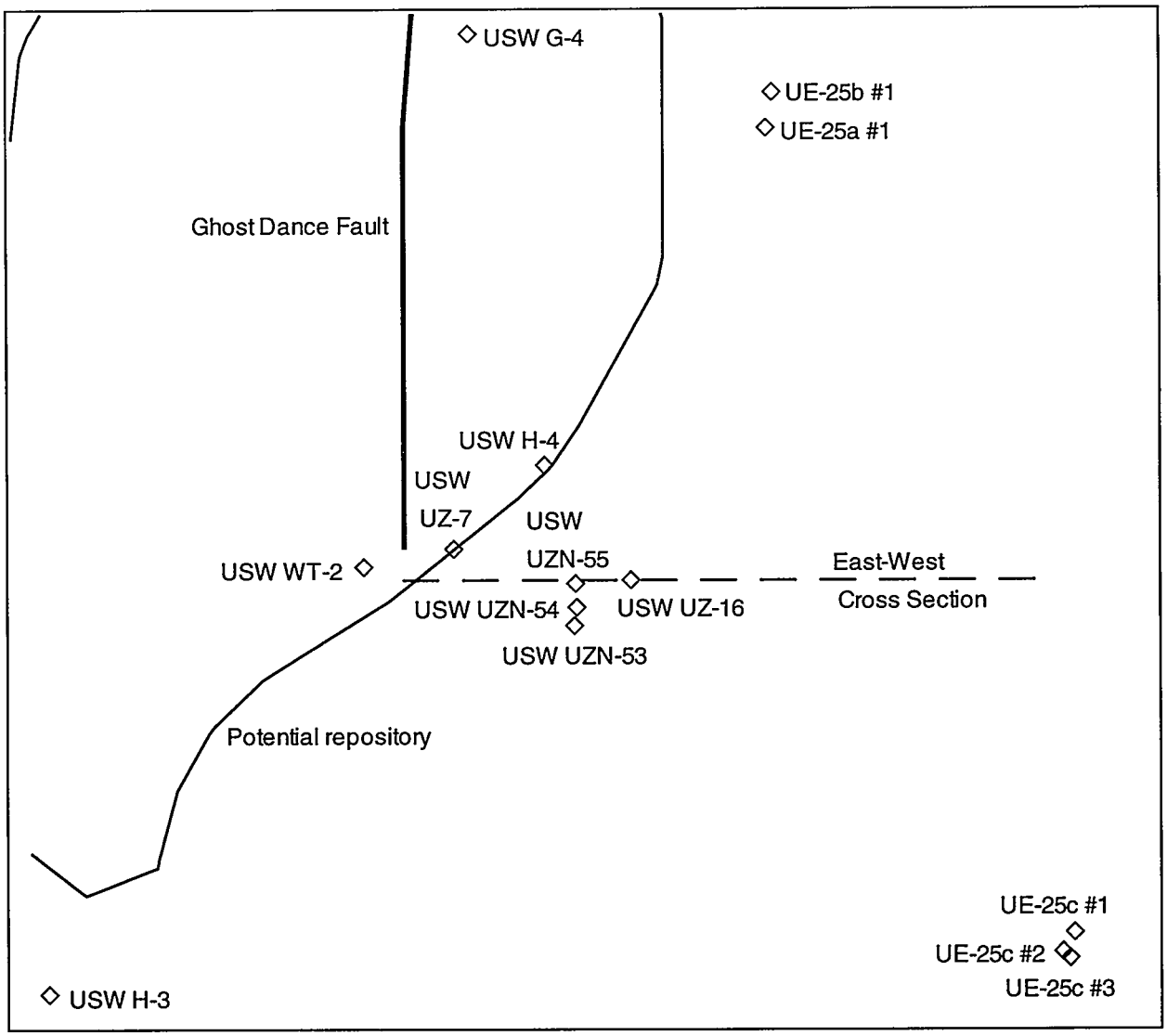

Figure 2. Drill Holes

than the estimated horizontal correlation length of 150 meters (Rautman and Flint, 1992 and Istok, *et al.*, 1991) use of Gaussian simulation to generate several realizations of the porosities throughout the cross section is appropriate. The vertical correlation length is 37 meters. The seven two-dimensional realizations are shown in Figure 5. Note that the welded Topopah Spring is not laterally intact in simulations 2 and 7. Also, the Paintbrush nonwelded interval varies in shape and thickness. There is a tendency for higher porosity to show up in the center of the top of the figure due to lack of conditioning data on one side.

## Sequential Indicator Simulation

Available drill holes in the vicinity of USW UZ-16 are shown in Figure 2. Many of the drill holes do not reach the water table and the few drill holes east of USW UZ-16 are located

far from the cross section. Also, many of the drill holes do not have porosity measurements. Thus, use of Gaussian simulation for porosity is not appropriate. Yet, the spatial continuity of the units is quite good. Thus, indicator simulation is selected. The lithologic categories chosen are welded, nonwelded, and zeolitic materials. The logic for this division is that there is an inverse correlation between the degree of welding and porosity/permeability and there is an alteration of pore structure in zeolitic materials that reduces permeability.

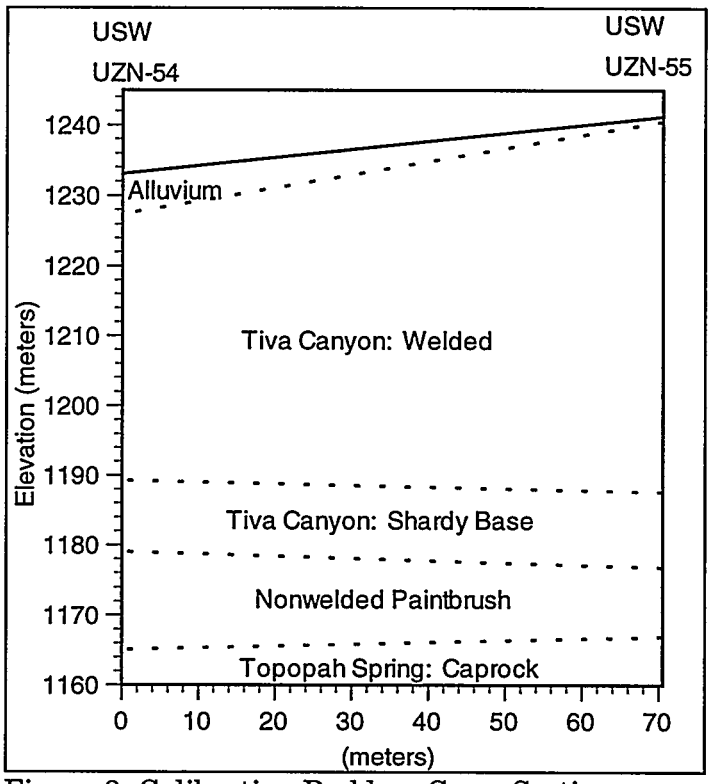

Figure 3. Calibration Problem Cross Section

The average bedding angle is 6.7° dipping to the east. The overall percentages for the categories are 70% welded, 22% zeolitic, and 8% nonwelded. The details regarding the development of the model of spatial continuity are given in TSPA 1993 (Wilson, *et al.*, 1994). The lateral anisotropy is adjusted to 1.0 for these simulations to allow the data on the west side of the cross section to propagate to the east rather than emphasizing the data to the north and south. Note that this may overstate the spatial continuity, although the results should be similar to that expected for the repository region where more data are available. The radius used for searching for nearby data also has been increased to 3350 meters. Also, an unlimited number of data are allowed from each quadrant.

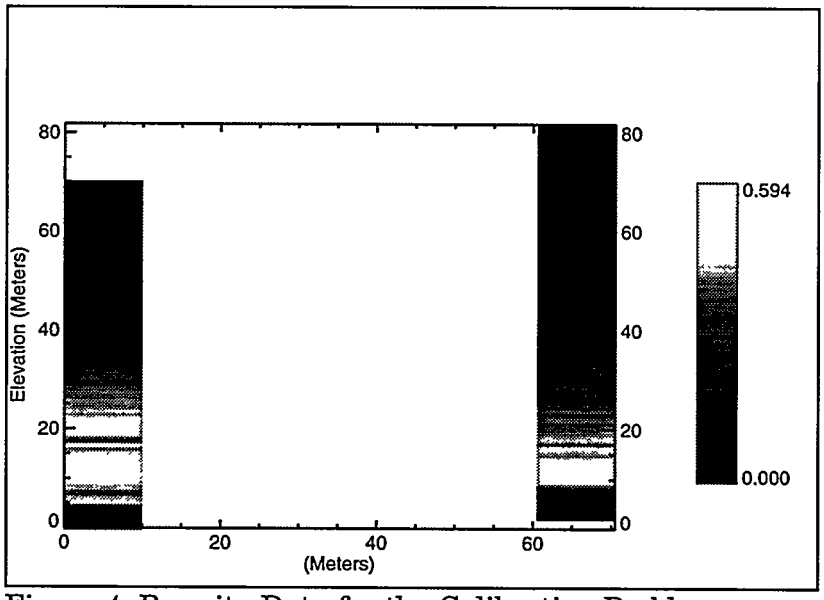

Figure 4. Porosity Data for the Calibration Problem

A three-dimensional grid is defined for the indicator

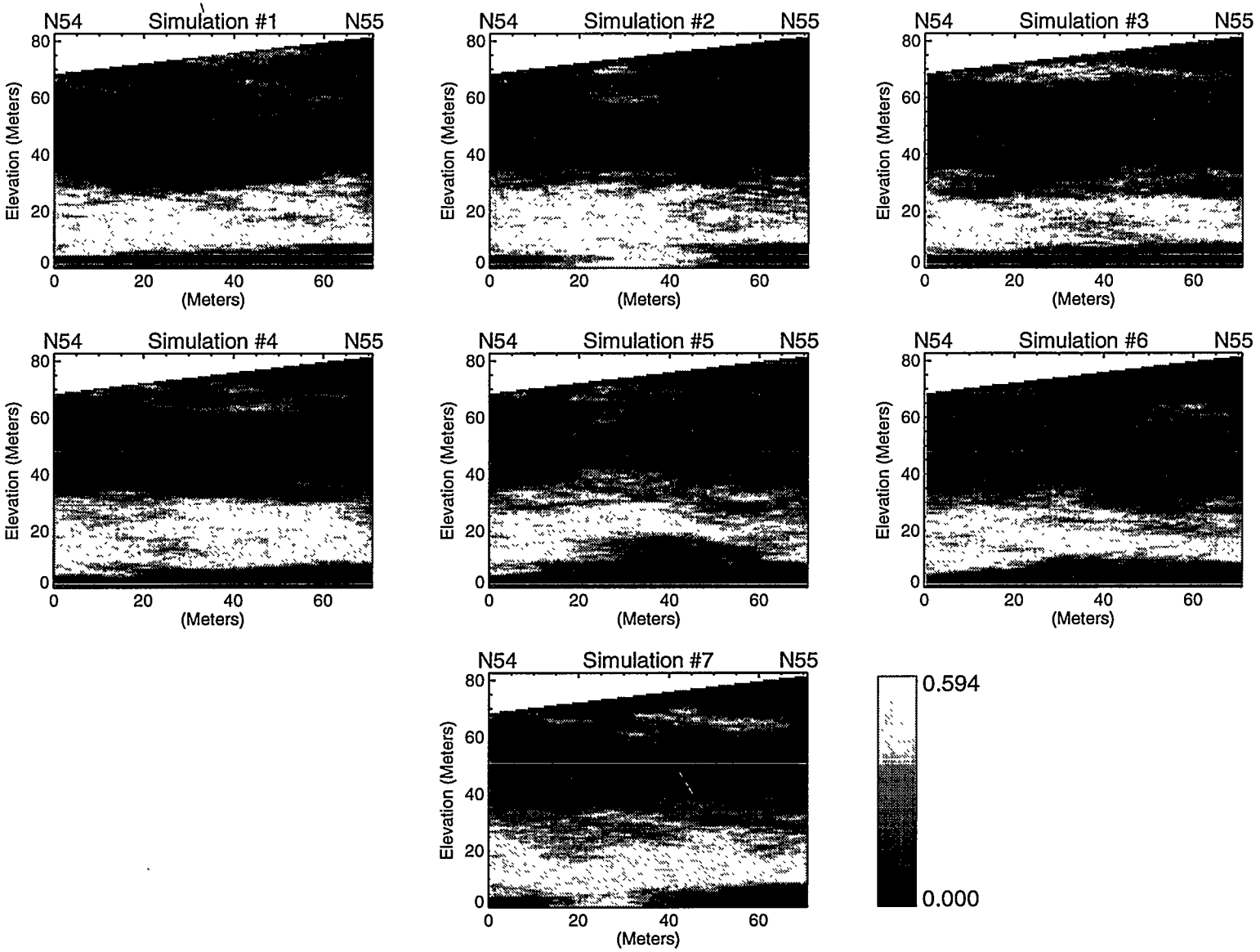


Figure 5. Simulated Porosity Cross-Sections for the Calibration Problem

simulation. The eastings range from 171,405.96 to 173,539.56 meters. A range of 231,712.11 to 232,169.31 meters is used for the northings. For the elevations, a range of 730.00 to 1309.12 meters is used. The grid nodes are 140 x 30 x 190 with the 30 nodes in the north-south direction used to help in identification of stratigraphic units. Horizontal node spacing is 15.24 meters in both directions and the vertical spacing is 3.05 meters apart.

# Stratigraphy and Flow Grid

The flow simulation uses a flow grid that typically is coarser than the grid used for the geostatistical simulations. In modeling unsaturated flow, one of the most important factors is to correctly describe the geometry. The geostatistical simulations provide detailed geometric information for each realization. Adaptive grids allow a great deal of the geometry to be portrayed. The flow grid is adapted to make the heterogeneity in each element proportional to the area of the element. By reducing heterogeneity within each element, the error involved in upscaling material properties is greatly reduced.

## Unit Stratigraphy

The indicator simulation produces layers of the three lithologic categories. The categories have to be split up into stratigraphic units. The process begins by searching for the Calico Hills and Prow Pass consisting of the vitric nonwelded or zeolitic nonwelded categories. Starting from either a vitric nonwelded or zeolitic nonwelded node, all connecting nodes from the same categories are identified as a potential unit. The search is repeated to construct several potential units. The largest of these potential units is then selected as the Calico Hills/Prow Pass and two units (vitric and zeolitic) are constructed. Nonwelded nodes are converted into the Calico Hills vitric unit and the zeolitic nodes are converted into the Calico Hills and Prow Pass nonwelded zeolitic unit. Then a sweep is made to find any welded nodes appearing in the Prow Pass. Any nodes of the welded category falling 200 feet below the top of the Calico Hills are converted to the welded Prow Pass unit.

The second step in the identification of units is to delineate the nonwelded Paintbrush. The largest unit of contiguous nonwelded nodes is selected. Then the grid is checked for any offset nonwelded nodes that may be due to a simulated fault. Each easting is checked for nodes from the selected unit and, if none exist, a search is conducted for contiguous sets of nonwelded nodes. The largest set is then added to the selected set. Any nonwelded nodes or zeolitic nodes that are not part of the selected units are regarded as noise generated by the geostatistical procedure and are converted to the welded category. The midpoint of the nonwelded Paintbrush is determined and used to separate the welded Tiva Canyon and welded Topopah Spring units.

The result is a stratigraphy of six units for three simulations shown in Figures 6 through 8. For geostatistical simulations where the units are not well formed due to

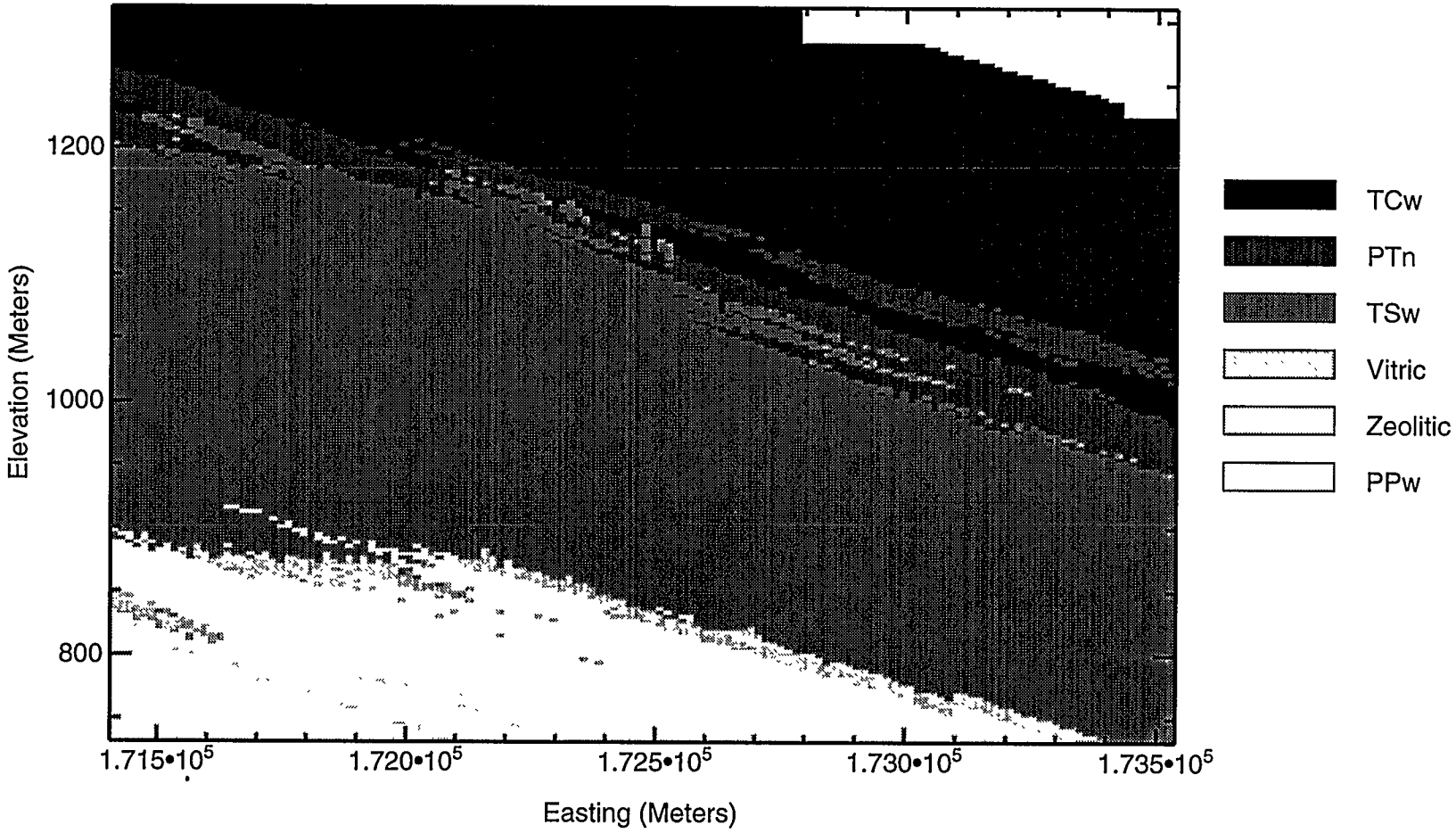


Figure 6. Unit Stratigraphy for the INTRAVAL Problem, Simulation #1

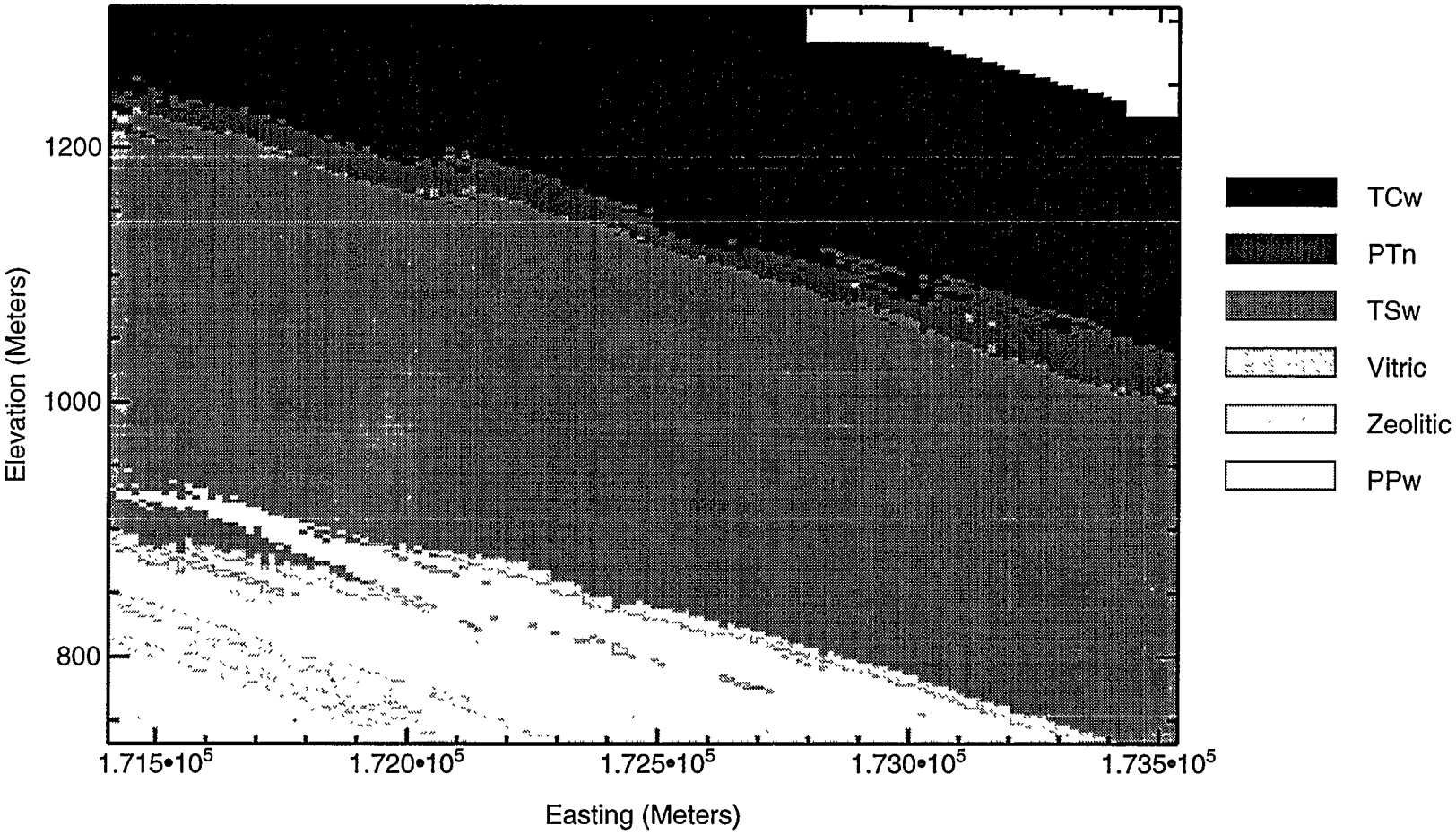


Figure 7. Unit Stratigraphy for the INTRAVAL Problem, Simulation #2

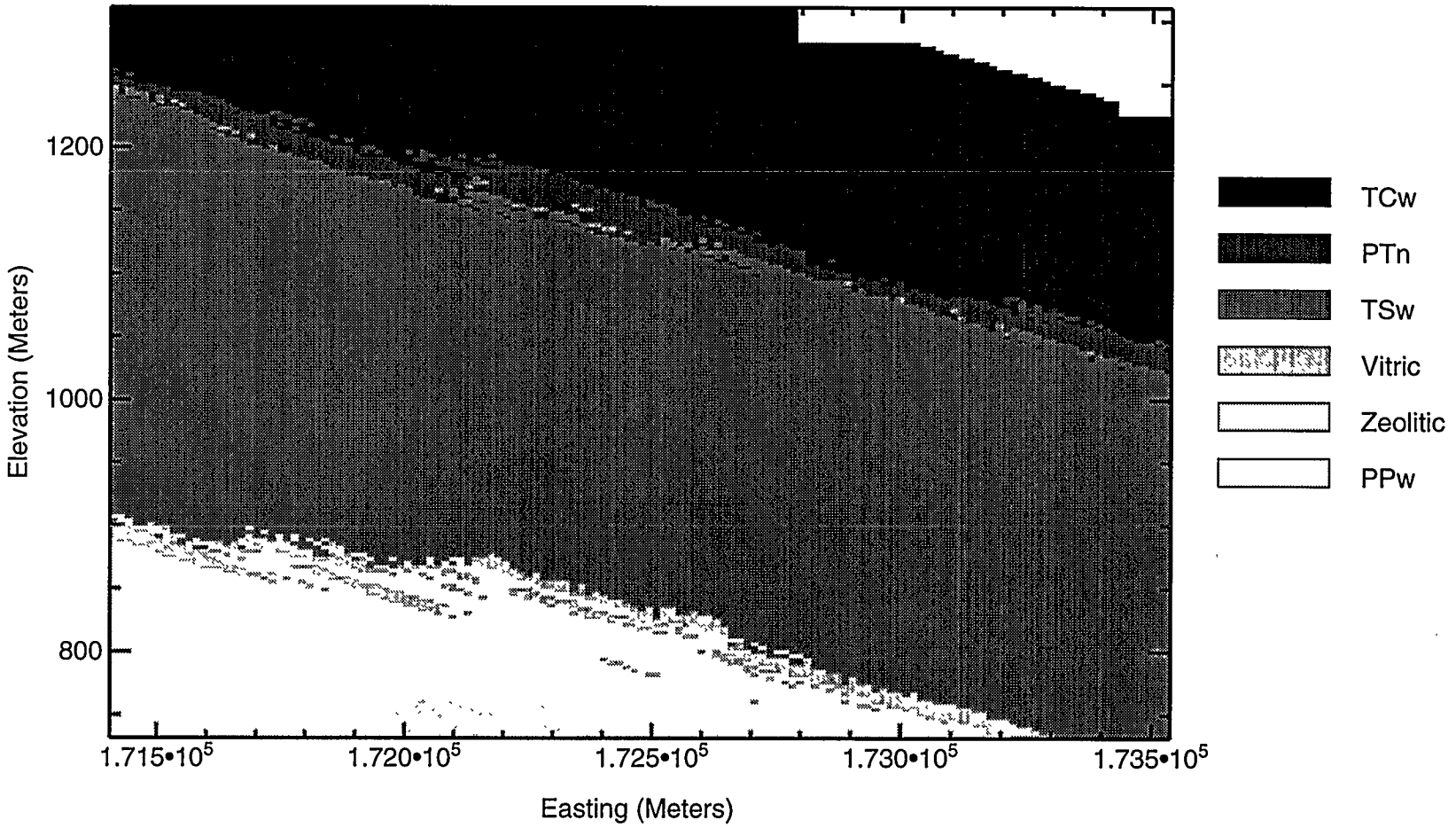


Figure 8. Unit Stratigraphy for the INTRAVAL Problem, Simulation #3

insufficient data, the conversion process to stratigraphic units may be flawed but it is objective and automatic. As more data are obtained the conversion process improves.

## Generating Porosity Values

Porosity has been chosen to be the fundamental hydrologic property in these simulations. The stratigraphies must be converted into porosities before the flow grid is adapted to the cross section. Statistics gathered for each unit are used. Also, deterministic trends can be incorporated to allow detailed features of the stratigraphy to be added. The generated porosities are not conditioned to the porosity data; the simulated porosity, in general, will not exactly match the measured porosities of the core samples at the original location of the core. Also, the spatial correlations for porosity are ignored since it is expected the scale of the elements will be of the order of the correlation length of porosity.

The welded Tiva Canyon unit, vitric nonwelded Calico Hills unit, zeolitic nonwelded unit and the Prow Pass welded unit are all treated as single units. The Topopah Spring welded unit and nonwelded Paintbrush units are split into subunits. The Topopah Spring welded unit has a densely welded vitric caprock at the top and a basal vitrophyre and shardy base at the bottom. The basal vitrophyre is below the potential repository and may be important to travel times. These subunits are too thin to be explicitly considered in the geostatistical stratigraphy, thus the percentages are based on thicknesses at USW UZ-16 (Voss, 1993b). The top 1.10% below the nonwelded Paintbrush is considered vitric caprock. The bottom 3.67% is considered nonwelded Topopah Spring shardy base and then above the shardy base is the basal vitrophyre subunit with 5.60% of the thickness. The nonwelded Paintbrush is split up into a bedded subunit (bottom 58.2%) and shardy base subunit (part of the Tiva Canyon ash flow).

The porosity of the shardy base subunit is modeled with a deterministic linear vertical change in porosity, $\phi$, similiar to Rautman, *et al.* (1993)

$$\phi = 0.46653 - 0.28946z + 0.057025g(), \tag{1}$$

where $z$ is the normalized elevation in the shardy base (bottom of shardy base is 0 while the top has an elevation of 1) and $g()$ is the unit Gaussian deviate (normal distribution with a standard deviation of 1). The porosities for the other units and subunits are computed using the expected value and the standard deviation computed from the INTRAVAL data and shown in Table 1. Thus the scatter is assumed to be normally distributed. The results of the

conversion are shown in Figures 9 through 11 (the grids shown are discussed later in the section on adaptive grids). The sources for the porosity data used are listed in Table 2.

Table 1: Porosities

| Unit (Symbol) | Subunit | Average | Standard Deviation |
|---|---|---|---|
| welded Tiva Canyon (TCw) | | 0.0697 | 0.0302 |
| nonwelded Paintbrush (PTn) | shardy base | 0.1771 | see Equation (1) |
| nonwelded Paintbrush (PTn) | bedded | 0.4504 | 0.1054 |
| Topopah Spring (TSw) | vitric caprock | 0.0565 | 0.0393 |
| Topopah Spring (TSw) | welded main | 0.1297 | 0.0369 |
| Topopah Spring (TSw) | basal vitrophyre | 0.0641 | 0.0434 |
| Topopah Spring (TSw) | nonwelded shardy base | 0.2363 | 0.0572 |
| vitric nonwelded Calico Hills (vitric) | | 0.3664 | 0.0742 |
| zeolitic nonwelded (zeolitic) | | 0.3053 | 0.0460 |
| welded Prow Pass (PPw) | | 0.1941 | 0.0575 |

The average porosity for the welded Tiva Canyon and welded Topopah Spring units were less than those in data developed for TSPA 1993 (Schenker, *et al.*, 1994). One possible reason is that older measurements included nonconnected pores and/or water bound up in minerals. The variation of porosity for the zeolitic unit is significantly less than that used for TSPA 1993. The average Prow Pass porosity is 0.1941 versus 0.292 for TSPA 1993 which could be due to the small amount of data available, difficulty in clearly distinguishing the vertical extent of the welded unit, and/or the variation in welding in Prow Pass in its horizontal extent.

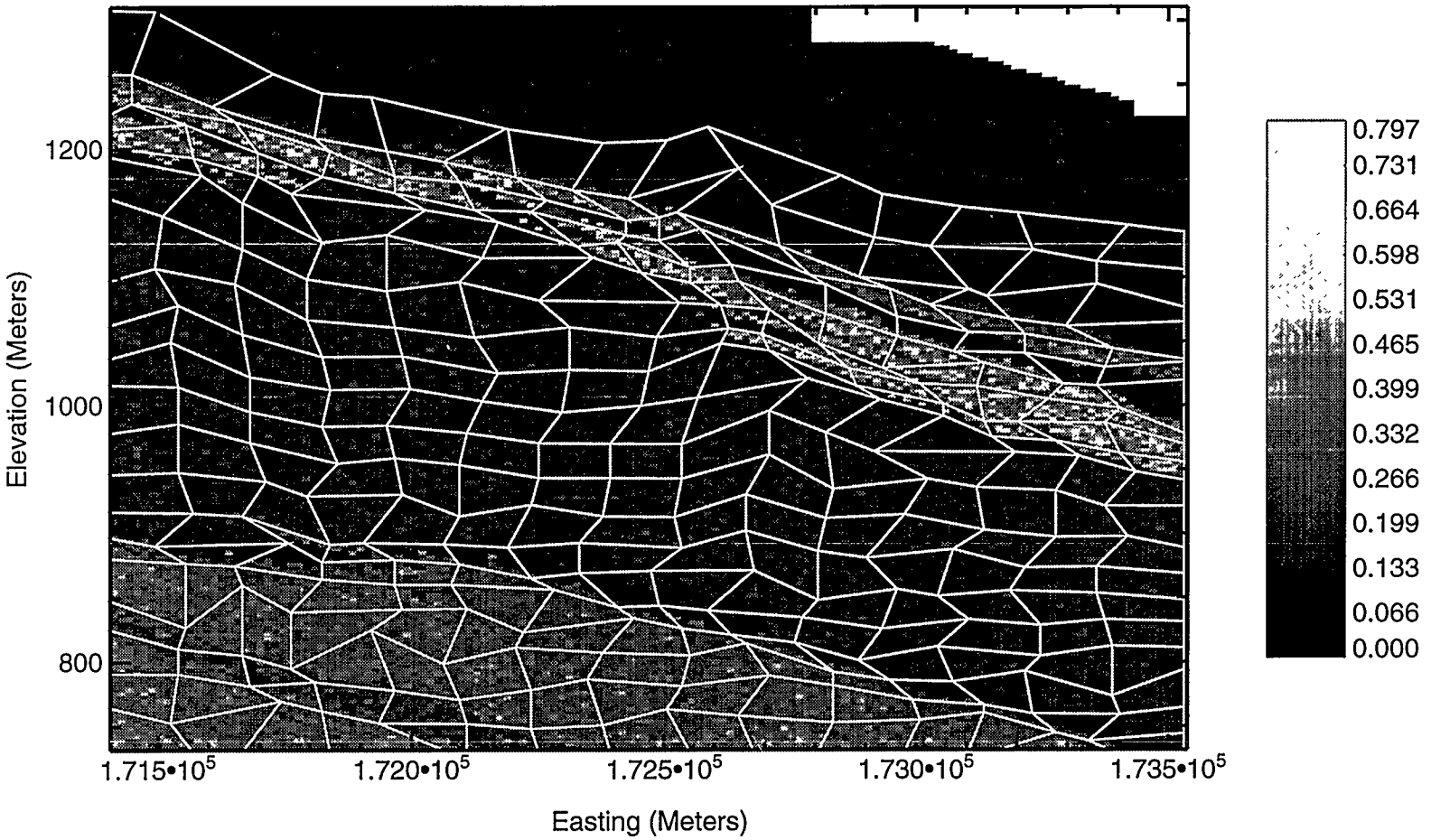


Figure 9. Detailed Porosities and Adapted Grid for the INTRAVAL Problem, Simulation #1

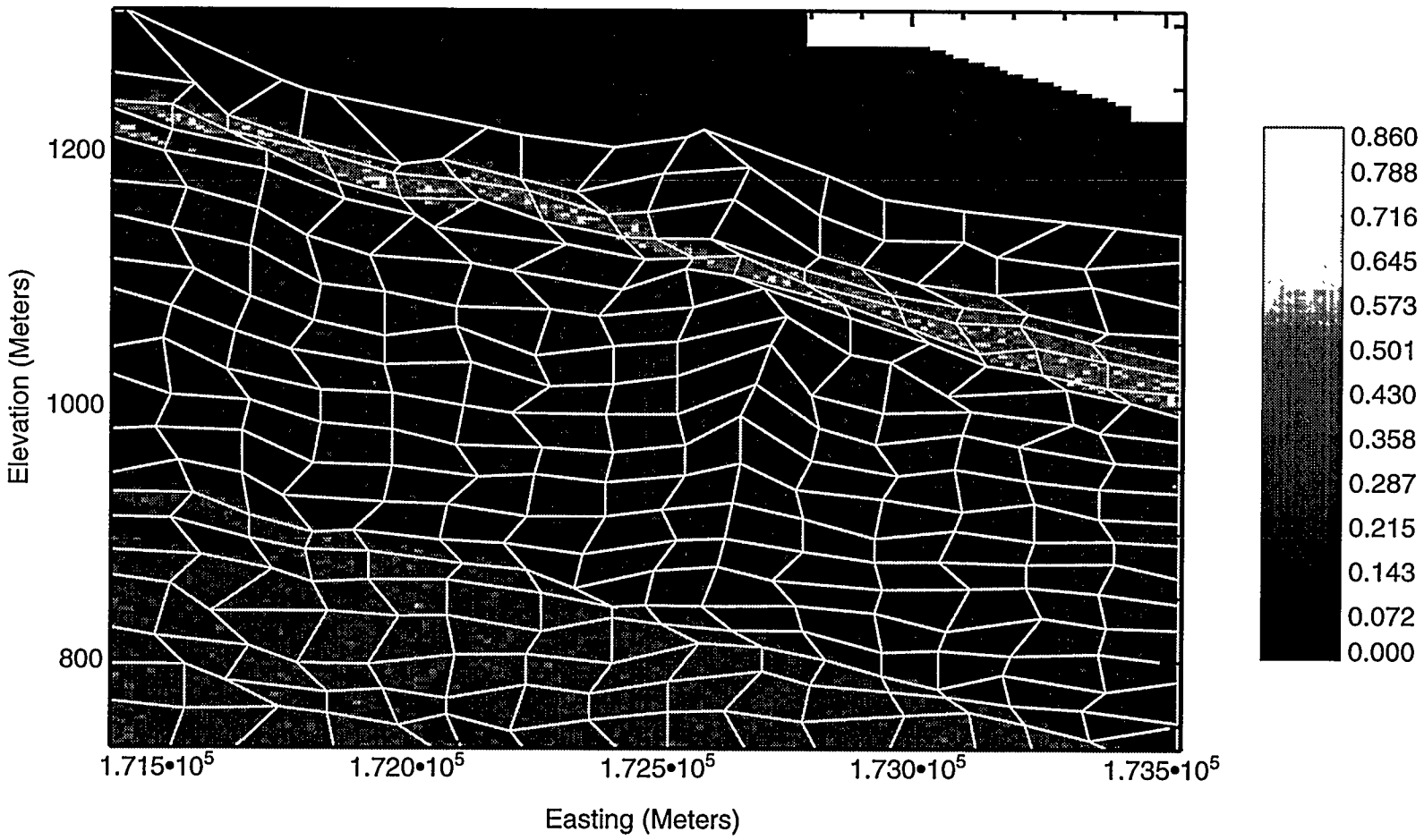


Figure 10. Detailed Porosities and Adapted Grid for the INTRAVAL Problem, Simulation #2

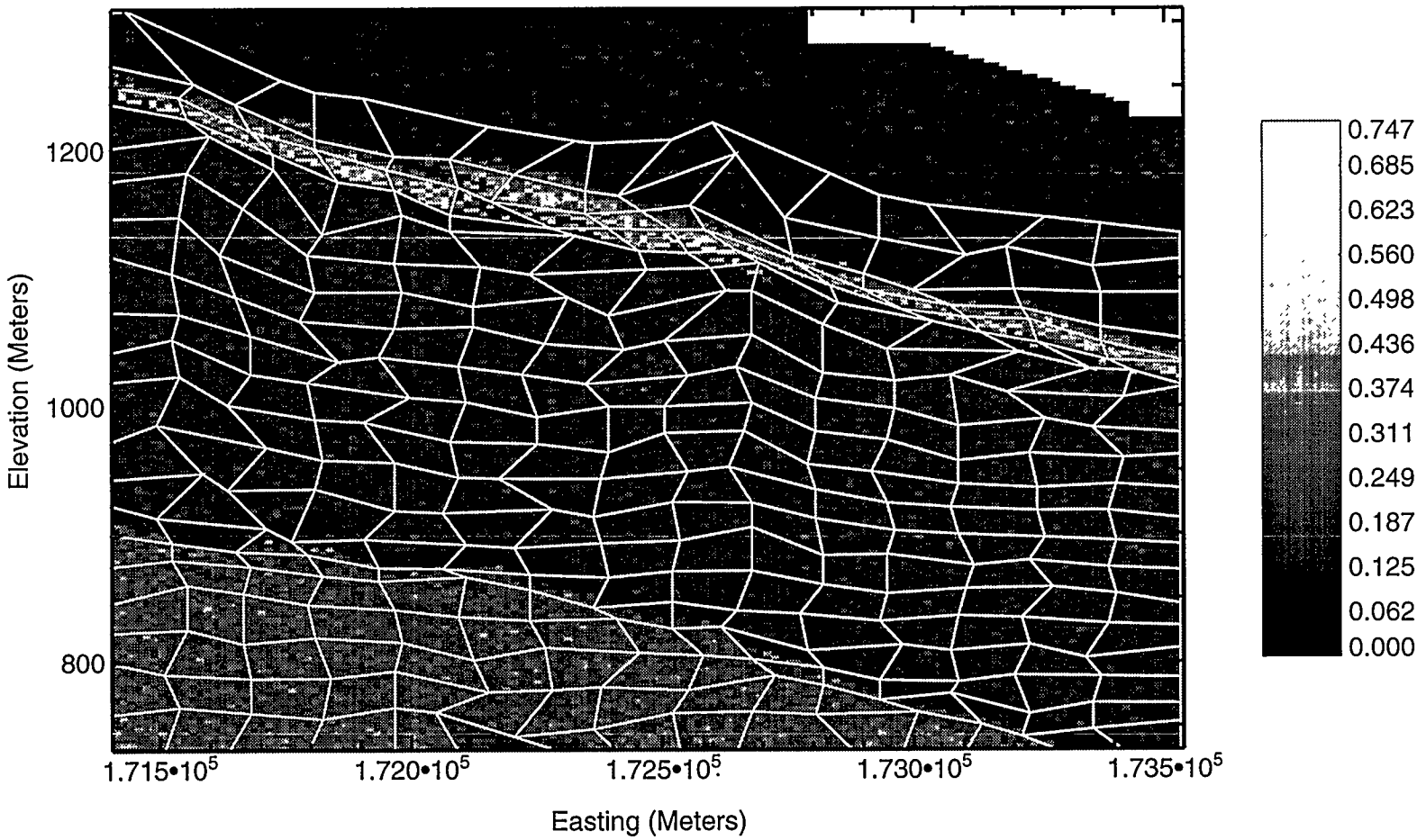


Figure 11. Detailed Porosities and Adapted Grid for the INTRAVAL Problem, Simulation #3

Table 2: Porosity Data Sources

| Unit | Subunit | Data Sources |
|---|---|---|
| welded Tiva Canyon | | USW UZN-53 (Voss, 1992b and Voss, 1993a)<br>USW UZN-54 and USW UZN-55 (Voss, 1992a)<br>transect (Voss, 1992a and Voss, 1993a)<br>USW UZ-16 (Voss, 1993b) |
| nonwelded Paintbrush | shardy base | USW UZN-53 (Voss, 1992b and Voss, 1993a)<br>USW UZN-54 and USW UZN-55 (Voss, 1992a)<br>USW UZ-16 (Voss, 1993b) |
| nonwelded Paintbrush | bedded | USW UZN-53 (Voss, 1992b and Voss, 1993a)<br>USW UZN-54 and USW UZN-55 (Voss, 1992a)<br>transect (Voss, 1992a and Voss, 1993a)<br>USW UZ-16 (Voss, 1993b) |
| Topopah Spring | vitric caprock | USW UZN-53 (Voss, 1992b and Voss, 1993a)<br>USW UZN-54 and USW UZN-55 (Voss, 1992a)<br>USW GU-3 (Voss, 1992a)<br>transect (Voss, 1992b and Voss, 1993a)<br>USW UZ-16 (Voss, 1993b) |
| Topopah Spring | welded main | USW UZN-54 (Voss, 1992a)<br>transect (Voss, 1992a and Voss, 1993a)<br>USW UZ-16 (Voss, 1993b) |
| Topopah Spring | basal vitrophyre | transect (voss, 1992a and Voss, 1993a)<br>USW GU-3 (Voss, 1992a)<br>USW UZ-16 (Voss, 1993b) |
| Topopah Spring | nonwelded shardy base | USW UZ-16 (Voss, 1993a) |
| vitric nonwelded Calico Hills | | USW GU-3 (Voss, 1992a) |
| zeolitic nonwelded | | transect (Voss, 1992a and Voss, 1993a)<br>USW UZ-16 (Voss, 1993b) |

Table 2 continued

| Unit | Subunit | Data Sources |
|---|---|---|
| welded Prow Pass | | USW UZ-16 (Voss, 1993b) |

## Adaptive Grid

An adaptive grid allows the elements used in the flow simulator to match the geometrical features in the geostatistical simulation. Boundaries between geologic units do not follow straight lines but adopt a more natural undulation or irregular contact surface.

The adaptive grid algorithm uses four fixed corner nodes and problem-defined boundaries for the four sides. The grid adaption process begins by defining an initial mesh. This initial grid is obtained by first equally spacing the nodes on a straight line along the left and right sides and then adjusting them to fit the problem-defined boundaries. Then the $x$-coordinates are equally spaced row by row between the respective nodes on either side. The top and bottom row of nodes are adjusted to fit the problem-defined boundaries. The final step equally spaces the $y$-coordinates between the respective top and bottom nodes.

A major goal of the adaptive grid is to reduce heterogeneity within elements in order to reduce uncertainty in upscaling material properties. First, a measure of heterogeneity must be introduced to allow grids to be compared. Minimization of the 2-norm

$$\|\sigma a\|_2 = \left[\sum_{i=1}^{n} (\sigma_i a_i)^2\right]^{1/2}, \tag{2}$$

when used to adapt a mesh attempts to make the standard deviation, $\sigma_i$, of porosity proportional to the area, $a_i$, of the element (Steinberg and Roache, 1985). This norm can be minimized by either (1) reducing heterogeneity within elements by aligning the grid with the geometric features, or (2) reducing the size of elements in areas of underlying heterogeneity. Small, heterogeneous elements may be subject to upscaling errors but presumably the smaller size reduces their importance to the flow calculations.

The key to the grid adaption process is that moving any flow grid node influences the contribution to the overall norm by at most four elements. A local norm is defined and calculated for each internal node by applying Equation (2) to the four neighboring elements. Then, after sorting the flow grid nodes by their local norms, the grid is adjusted node by node starting with the flow grid node with the highest local norm. The smallest adjustment that

virtually guarantees a change in elements for some of the underlying geostatistical nodes is the spacing of the geostatistical nodes. Also, the spacing of the underlying geostatistical nodes gives a bound for the possible resolution in the flow grid. Thus each flow grid node is adjusted in the $x$ and $y$ directions by positive and negative increments equal to the spacing of the geostatistical nodes. The local norm is recomputed after each adjustment and the adjustment accepted if the local norm decreases. A similar process is carried out for boundary nodes using a local norm based on the two adjacent elements and always adjusting the nodes to lie on the problem-defined boundary.

The grid adjustment can be carried out until a sweep of the nodes produces no changes. At some point, however, the improvements are small relative to the computing time required. Thus, grid adjustment is stopped when a reduction in the 2-norm of less than 0.5% is realized after a sweep of the nodes.

Finite element methods map the elements from physical space to a master element with local coordinates $\{\xi_i\} = \{\xi,\eta\}$. The master element is centered at the origin with $-1 \le \xi,\eta \le 1$ as shown in Figure 12. The Jacobian of the transformation, $|\mathbf{J}|$, from physical space to the master element must be greater than 0 to ensure the mapping is one-to-one, i.e., not degenerate. For quadrilateral elements with bilinear basis functions (see Appendix A for more details) the Jacobian is

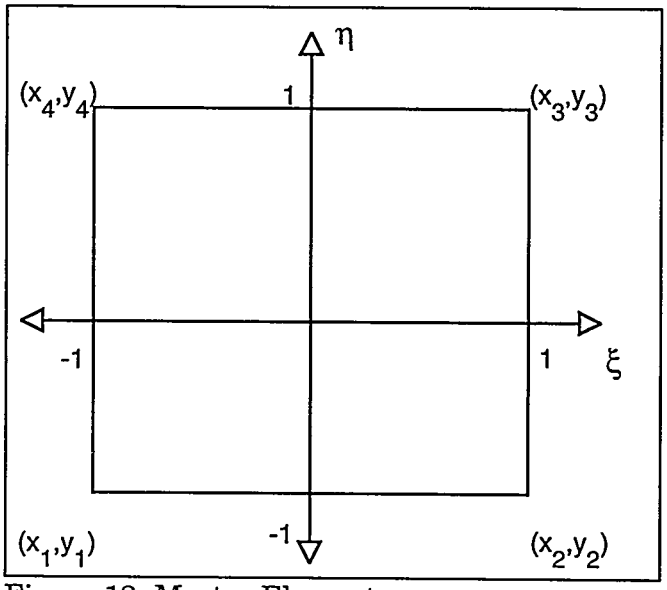

Figure 12. Master Element

$$|\mathbf{J}| = j_0 + j_1\xi + j_2\eta, \tag{3}$$

where

$$\begin{aligned} j_0 &\equiv [(x_1 - x_3)(y_2 - y_4) - (x_2 - x_4)(y_1 - y_3)]/8, \\ j_1 &\equiv [(x_3 - x_4)(y_1 - y_2) - (x_1 - x_2)(y_3 - y_4)]/8, \\ j_2 &\equiv [(x_2 - x_3)(y_1 - y_4) - (x_1 - x_4)(y_2 - y_3)]/8. \end{aligned} \tag{4}$$

Thus the condition for avoiding numerical problems due to the grid in the flow simulation is

$$j_0 - |j_1| - |j_2| > 0. \tag{5}$$

A physical interpretation of Equation (5) is that the quadrilateral element with bilinear basis functions must be convex; i.e., no angles of greater than 180°. Another situtation where Equation (5) is violated is where one of the sides of the quadrilateral has zero length. The grid adjustment checks Equation (5) to ensure that elements are not distorted too much. The distorted elements that result could still cause numerical problems due to high condition numbers if not handled properly by the flow code.

The results of applying the Geostatistical Adaptive Grid (GAG) code to the seven simulations of the calibration cross section are shown in Table 3. The average improvement in the 2-norm is 48%. For the maximum $\sigma_i a_i$ of any element the average improvement is 64%. The final grids are shown in Figures 13 through 19.

Table 3: Adaptive Grid Results for the Calibration Problem

| Seed | Initial 2-norm | Final 2-norm | Initial max $\sigma_i a_i$ | Final max $\sigma_i a_i$ |
|---|---|---|---|---|
| 1711 | 222.49 | 99.420 | 60.944 | 21.316 |
| 1713 | 195.42 | 110.39 | 58.491 | 22.550 |
| 1715 | 242.79 | 112.21 | 61.141 | 20.044 |
| 1717 | 225.15 | 104.74 | 55.706 | 19.294 |
| 1719 | 220.43 | 127.04 | 58.035 | 23.132 |
| 1721 | 202.38 | 102.59 | 60.160 | 21.853 |
| 1723 | 213.69 | 125.64 | 59.128 | 19.759 |

The INTRAVAL problem (east-west cross section) has less geologic structure and a larger scale that makes resolution of the features more difficult. The average reduction in the 2-norm is 27% for the three grids. For the same grids, the maximum $\sigma_i a_i$ of any element is reduced an average 41%. The norms for the three grids are given in Table 4. The grids are shown in Figures 9 through 11.

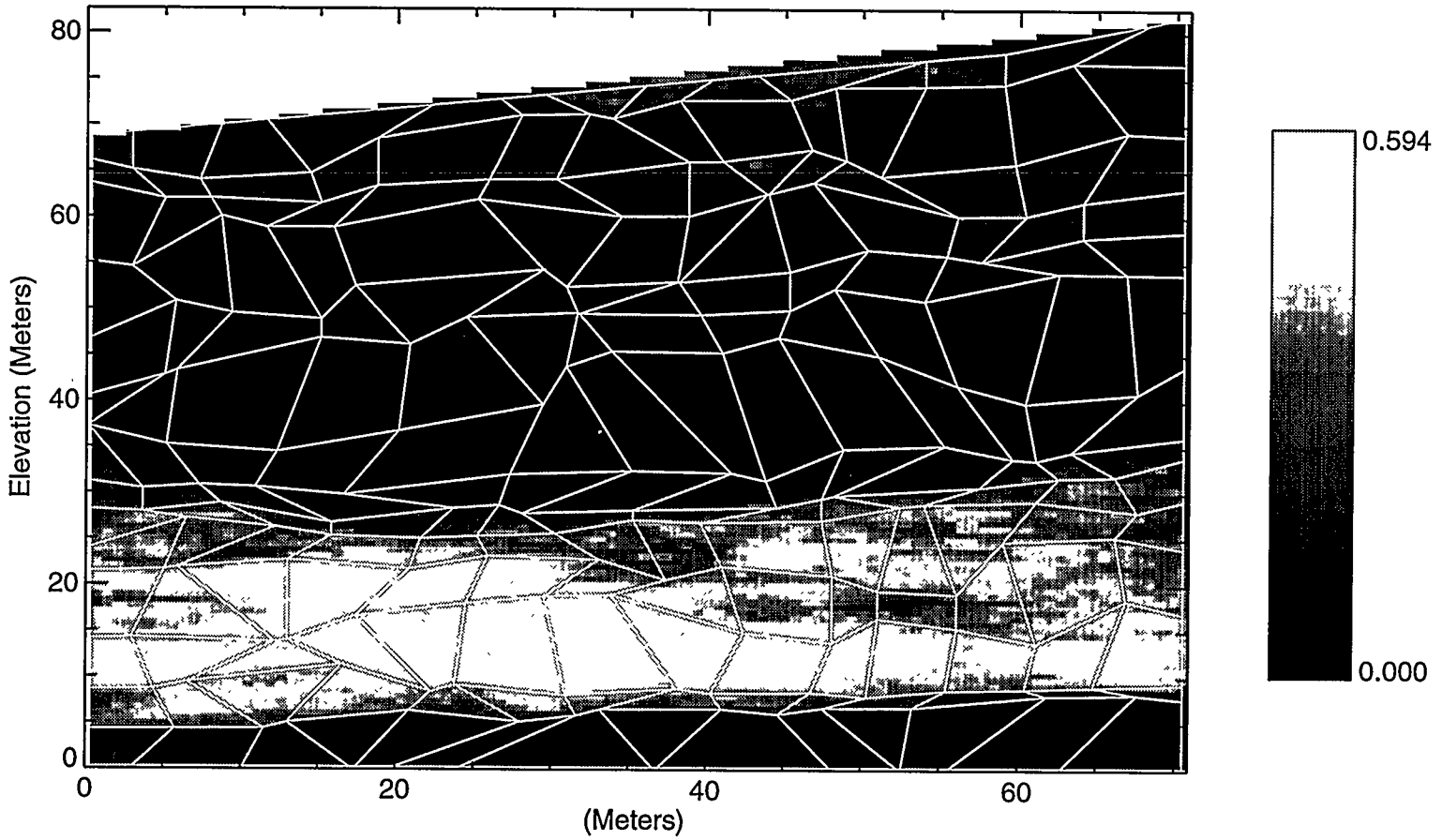


Figure 13. Adapted Grid for the Calibration Problem, Simulation #1

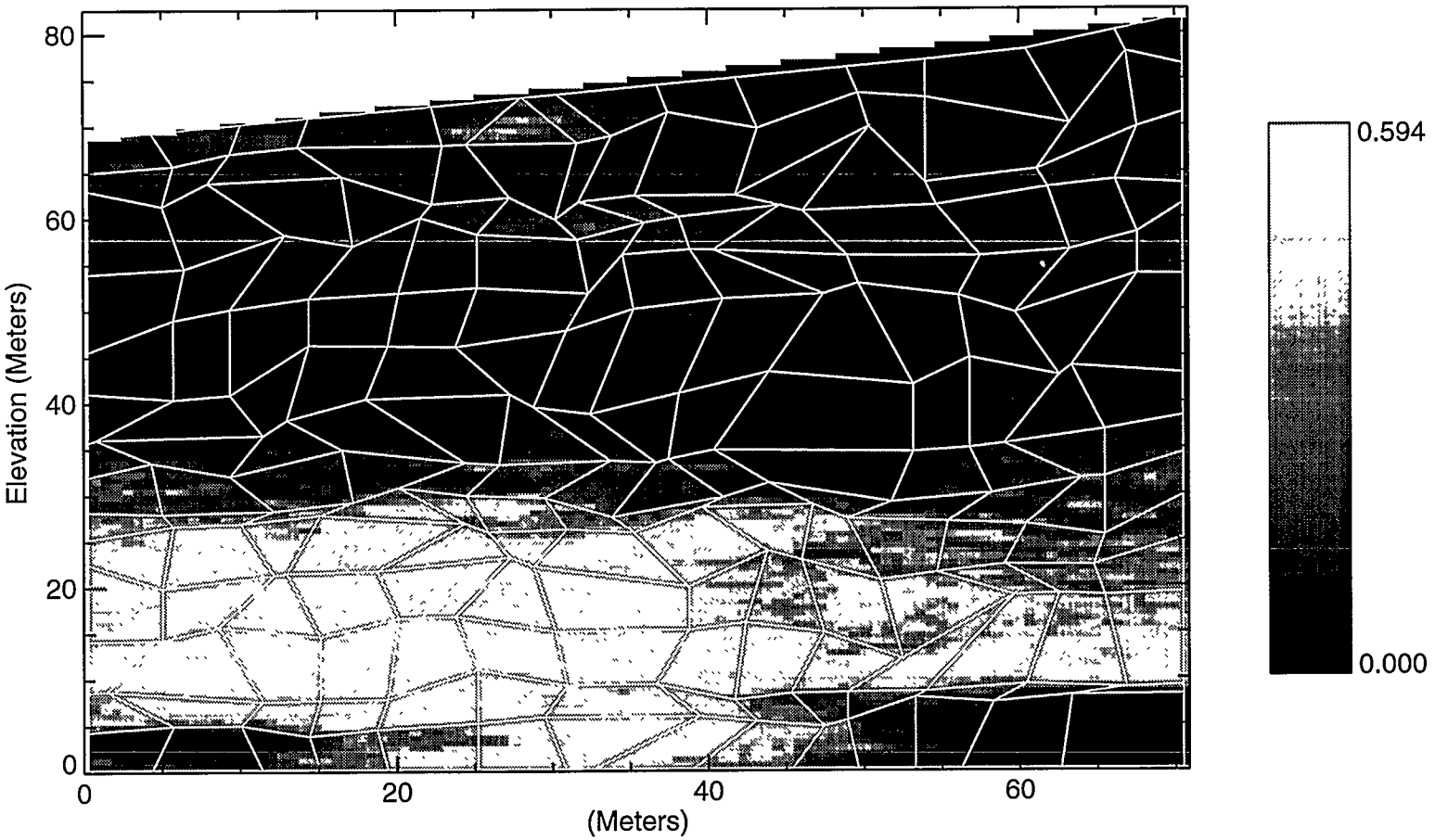


Figure 14. Adapted Grid for the Calibration Problem, Simulation #2

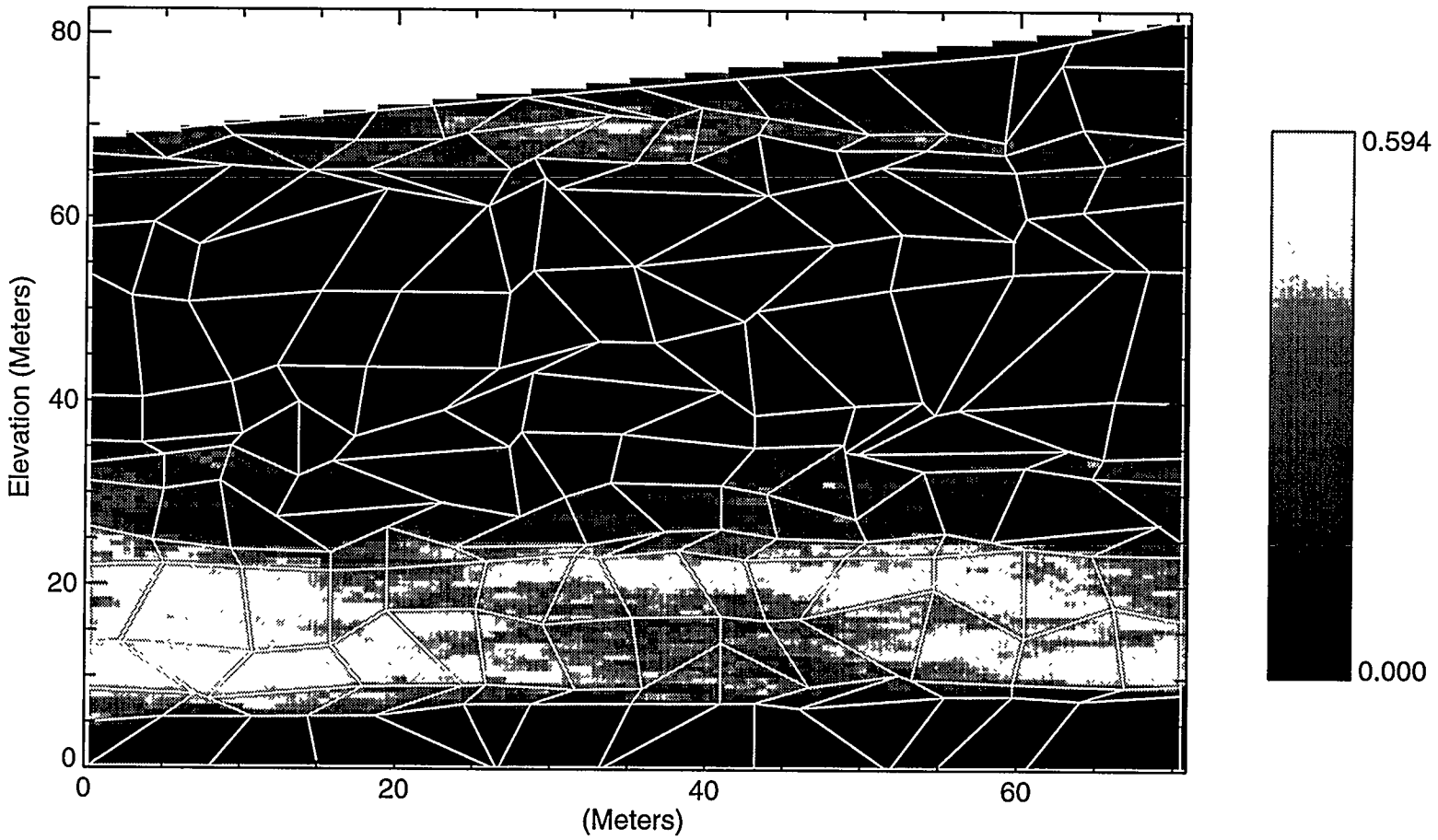


Figure 15. Adapted Grid for the Calibration Problem, Simulation #3

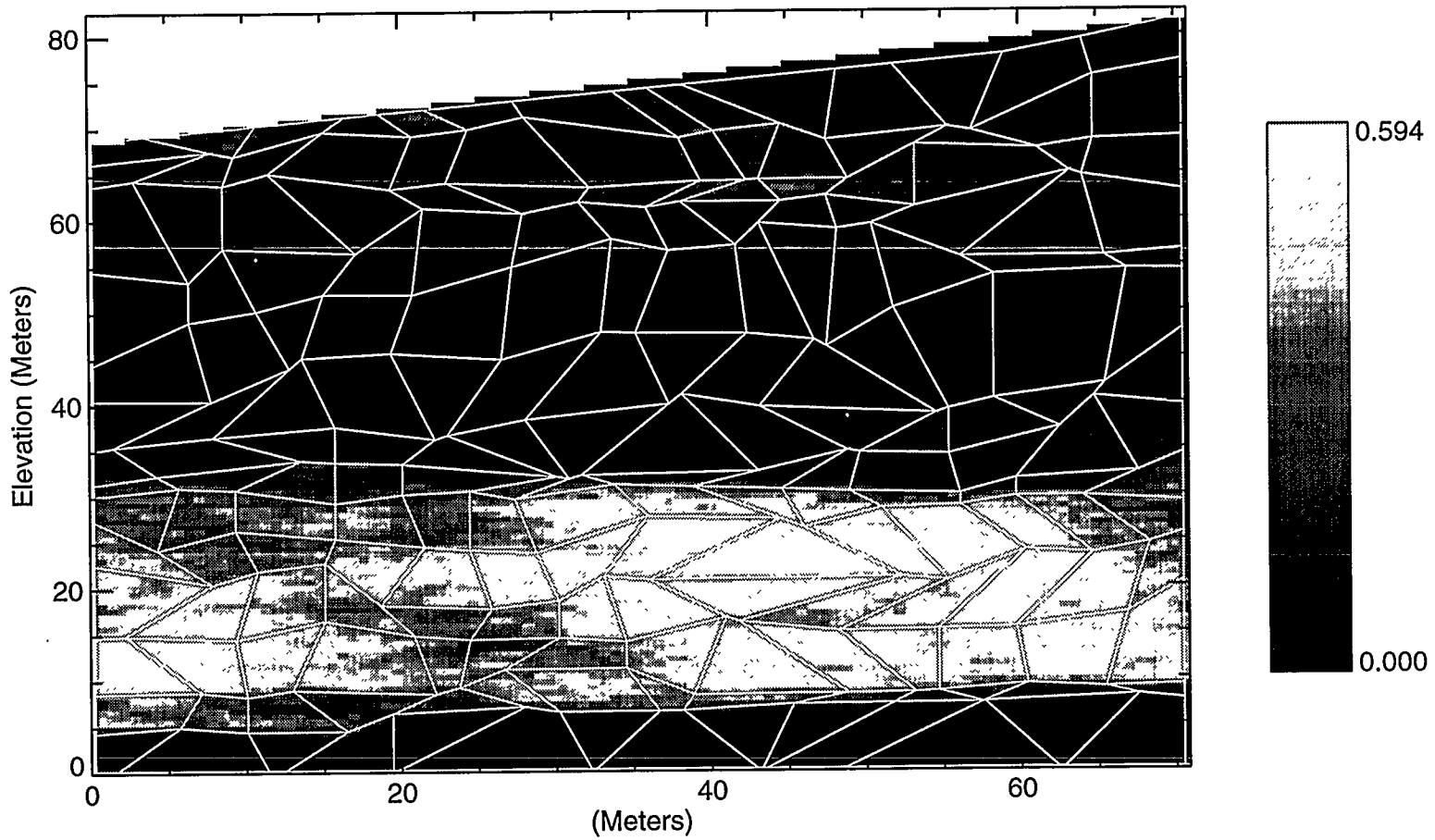


Figure 16. Adapted Grid for the Calibration Problem, Simulation #4

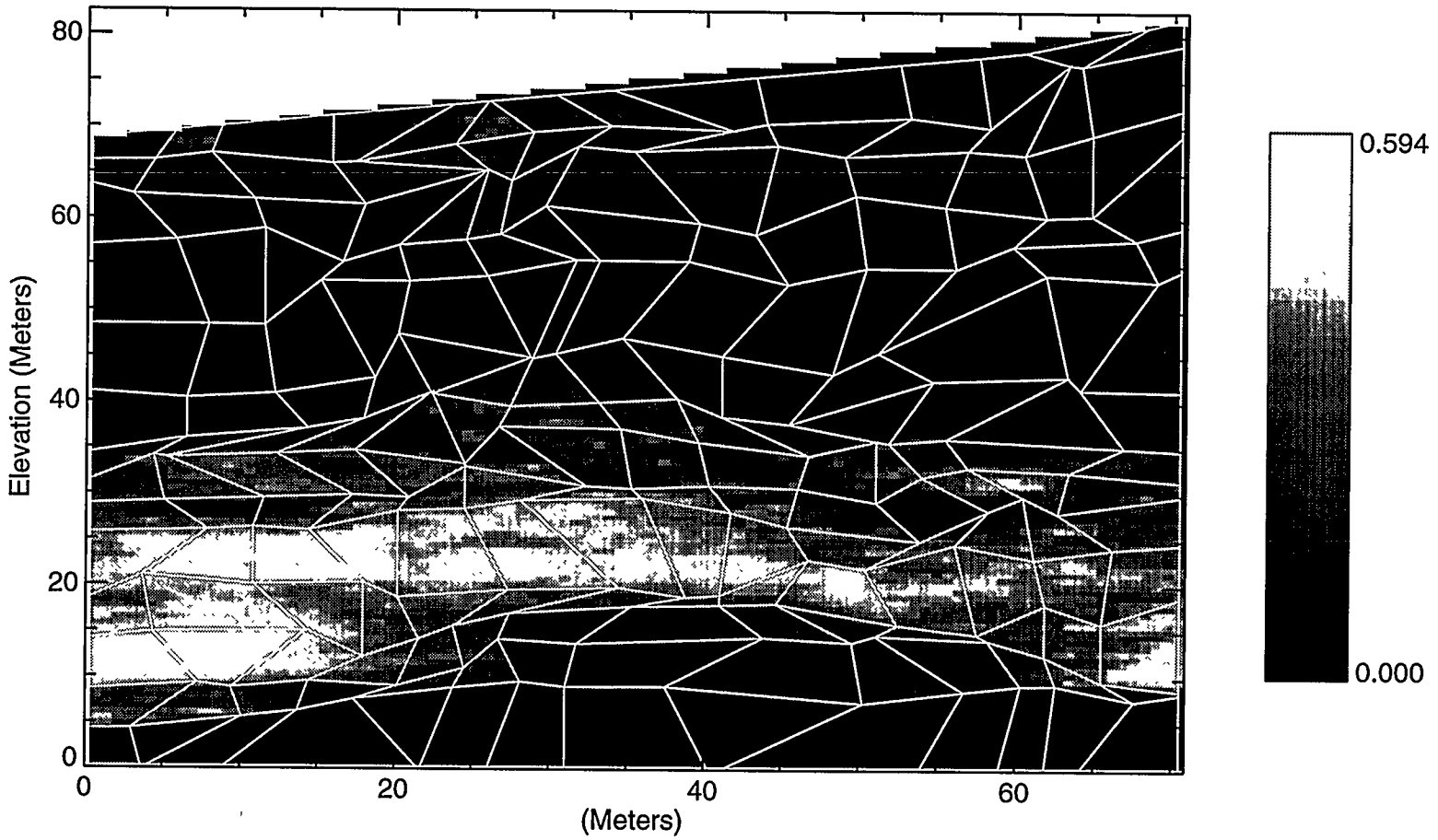


Figure 17. Adapted Grid for the Calibration Problem, Simulation #5

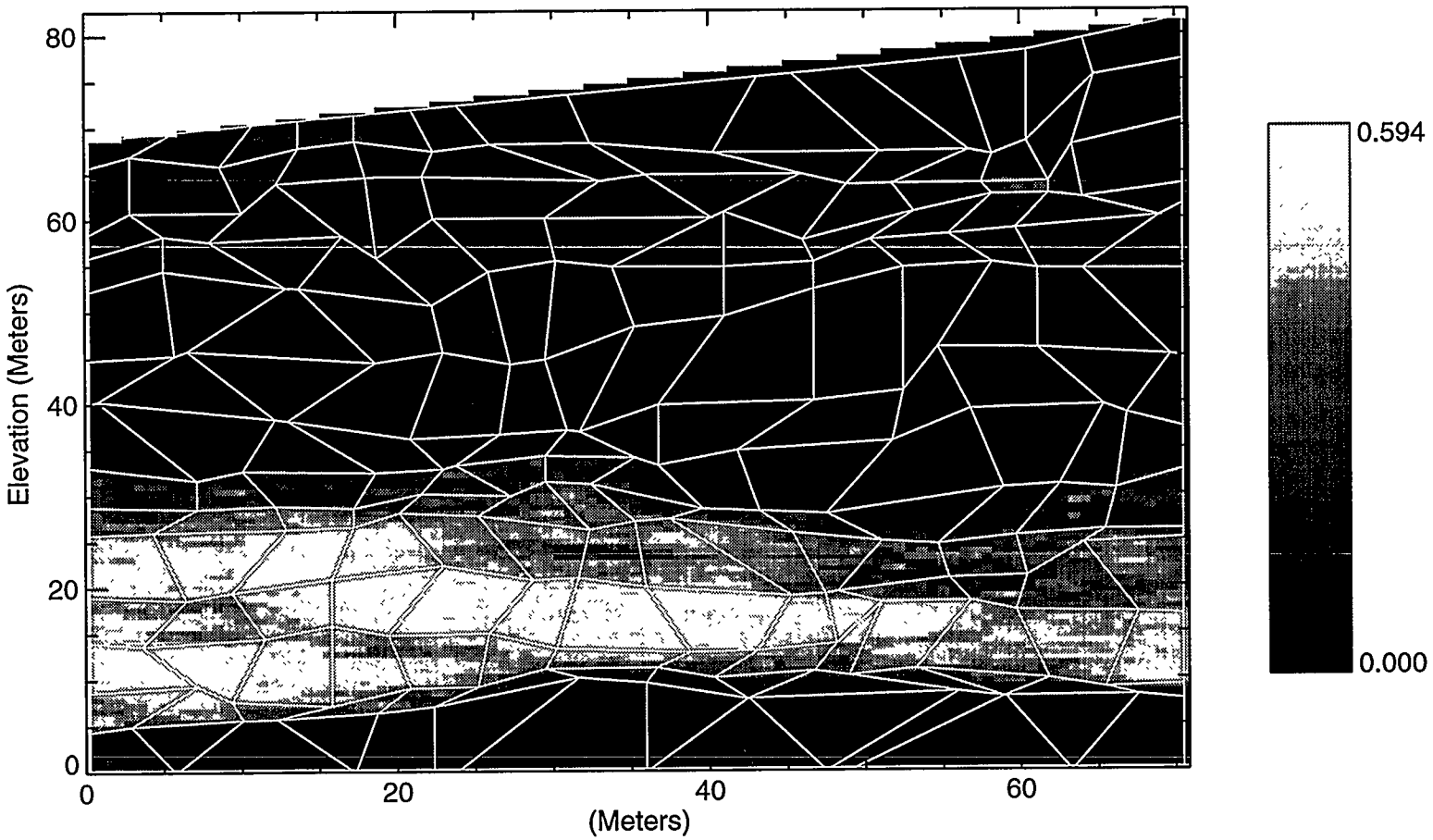


Figure 18. Adapted Grid for the Calibration Problem, Simulation #6

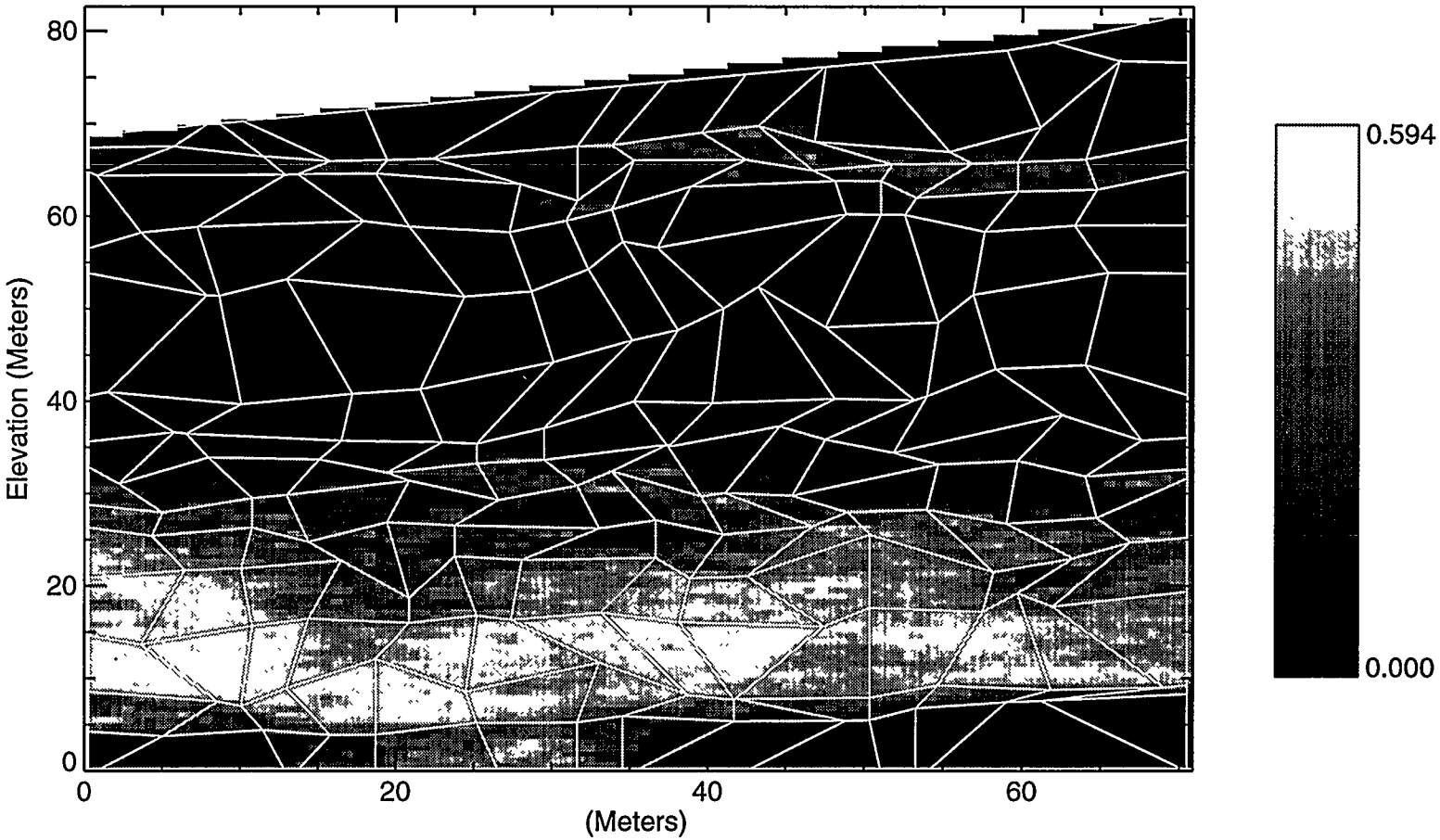


Figure 19. Adapted Grid for the Calibration Problem, Simulation #7

Table 4: Adaptive Grid Results for the INTRAVAL Problem

| Seed | Initial 2-norm | Final 2-norm | Initial max $\sigma_i a_i$ | Final max $\sigma_i a_i$ |
|---|---|---|---|---|
| 69067 | 49005 | 35858 | 7801.5 | 5097.9 |
| 69069 | 44116 | 32019 | 8003.7 | 4609.0 |
| 69071 | 42623 | 30813 | 7805.3 | 4227.4 |

# Material Properties

Material properties are generated based on the unit and porosity data generated earlier. In order to mimic Yucca Mountain as much as possible, the observed correlations in core data are used. Thus the proper scale to generate matrix material properties is on the fine-scaled geostatistics grid. The geostatistics grid is still a coarser scale than core scale but the difference is much less than between the scale of the flow grid and core scale. Once the matrix material properties are generated for the geostatistics grid, then the matrix element properties are generated for the flow grid using various scaling rules depending on the particular material property as discussed later in the section on upscaled properties. Although the scaling rules are subject to considerable uncertainty, the potential for error is greatly reduced by minimizing heterogeneity through use of the adaptive grid described earlier.

## Moisture Retention Curve

Two common models for the moisture retention curve are the Brooks and Corey (1966) model and the van Genuchten (1978) model. The Brooks and Corey model is given by

$$s=\begin{cases}(1-s_r)\left|\dfrac{\psi}{\psi_a}\right|^{\lambda}+s_r, & \left|\dfrac{\psi}{\psi_a}\right|\geq 1\\ 1, & \left|\dfrac{\psi}{\psi_a}\right|<1\end{cases}, \tag{6}$$

where $s$ is saturation, $\psi\leq 0$ is pressure, and $s_r$, $\psi_a$ and $\lambda$ are material parameters. Although the sharp beginning of desaturation at $\psi_a$, called the air entry pressure, is theoretically appealing, the Brooks and Corey model suffers numerical problems since there is not a unique pressure associated with a saturation of 1.0. The van Genuchten model is

$$s=(1-s_r)\left(\frac{1}{1+|\alpha\psi|^{\beta}}\right)^{\left(1-\frac{1}{\beta}\right)}+s_r, \tag{7}$$

where $s_r$, $\alpha$ and $\beta$ are parameters for the material. The van Genuchten model, like the Brooks and Corey model, originally was developed for soils. Fitting the van Genuchten model to sparse data typical of rock matrix results in an poorly posed problem due to the nature of

the van Genuchten parameters. Both $\alpha$, the air entry parameter, and $s_r$, the residual saturation, are related to the tails of the distribution of pore pressures at which desaturation occurs. The desaturation parameter, $\beta$, is related to the slope of the moisture retention curve or the standard deviation of the distribution of pore pressures at which desaturation occurs. For sparse data, the mean and standard deviation are the best fitting parameters while the parameters related to the tails of the distribution are difficult to determine.

An alternative to the Brooks and Corey model and the van Genuchten model is based on the gamma function. The gamma distribution is given by (Benjamin and Cornell, 1970)

$$f(x)=\frac{\lambda(\lambda x)^{a-1}e^{-\lambda x}}{\Gamma(a)},\ x\geq 0, \tag{8}$$

where $a$ and $\lambda$ are the two gamma parameters and

$$\Gamma(a)=\int_0^{\infty} e^{-u}u^{a-1}du. \tag{9}$$

The incomplete gamma function is

$$F(r)=\int_0^{r} f(x)dx=\frac{\Gamma(a,\lambda r)}{\Gamma(a)}=\frac{\int_0^{\lambda r} e^{-u}u^{a-1}du}{\Gamma(a)}, \tag{10}$$

where $r$ is the pore size diameter. Since all pores of diameter greater than $r$ are desaturated (assuming no trapping of moisture, see Klavetter and Peters (1987) for a more detailed discussion of the assumptions involved), then the incomplete gamma function is the moisture retention curve corresponding to a particular gamma function. One of the advantages of the gamma function is the ease with which it is possible to switch back and forth between the pore size distribution and moisture retention curve. Another advantage is that since the two gamma parameters are functions of the mean, $\bar{r}$, and the standard deviation, $\sigma(r)$, given by

$$a=\left[\frac{\bar{r}}{\sigma(r)}\right]^2, \tag{11}$$

$$\lambda=\frac{\bar{r}}{\sigma(r)^2}, \tag{12}$$

fitting the incomplete gamma function to sparse data is much better posed than fitting the van Genuchten function.

The incomplete gamma function can also be expressed in terms of pressure, $\psi$, using

$$\psi=\frac{c}{r}. \tag{13}$$

The constant $c$ is given by

$$c=\frac{2\gamma\cos\theta}{\rho g}=1.4185x10^{-5}\ \mathrm{m}^2=1.3896x10^{-6}\ \mathrm{mbar} \tag{14}$$

where $\gamma = 0.072$ N/m is the surface tension, $\theta = 15^{\circ}$ is the contact angle (Klavetter and Peters, 1986), $\rho = 1000$ kg/m$^3$ is the density of water, and $g = 9.806$ N/kg is the gravitational constant. Substituting Equation (13) into the incomplete gamma function

$$F(c/\psi)=\int_0^{c/\psi} f(x)dx=\frac{\Gamma(a,\lambda c/\psi)}{\Gamma(a)}=\frac{\int_0^{\lambda c/\psi} e^{-u}u^{a-1}du}{\Gamma(a)}. \tag{15}$$

Due to the inverse relationship between $\psi$ and $r$, the incomplete gamma function is equal to 1 at a suction pressure of 0 and approaches 0 as the magnitude of the suction pressure increases. In Figure 20 the moisture retention curve is plotted for fractures (discussed later in the section on fracture properties) using an incomplete gamma function. A van Genuchten curve has been fitted to the incomplete gamma function evaluated at 640 points and is also shown. The incomplete gamma function does not round off the corner where desaturation begins as much as the van Genuchten function. Thus, the incomplete gamma function is closer to the Brooks and Corey (1966) moisture retention curve yet the inverse function still exists.

Subroutines for the computation of the gamma function and the incomplete gamma function are commonly available and quick to evaluate (Press, *et al.*, 1988). The gamma function takes a few logarithm calls and about 25 floating point operations (flops) which is not much more than the standard trigonometric built-in functions. The incomplete gamma function is easily computed from a rapidly converging continued fraction.

## Core-Scale Properties

Developing correlations depends on the material property considered, its relationship to other properties and the amount of available data upon which to base the correlation. Lumping categories allows the correlations to be based on larger amounts of data and reduces the influence of a few data that may not be representative of the actual material properties.

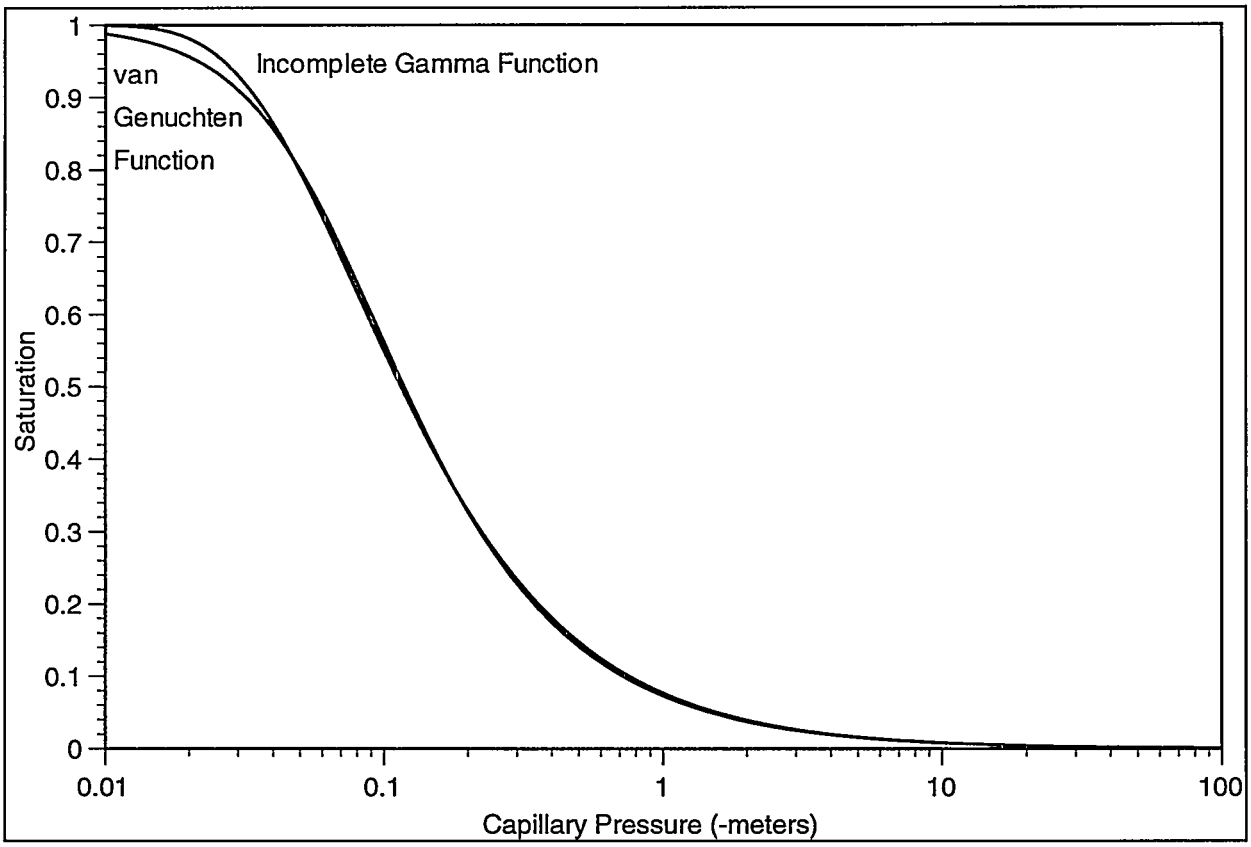

Figure 20. Moisture Retention Curve Comparison for Fractures

However, splitting the data into a greater number of categories allows more tailoring of the properties to a category that can otherwise be blurred by lumping. The approach taken in this study is to use the fewest possible number of categories since the emphasis is on testing the numerical approach.

Previous studies have shown that saturated hydraulic conductivity and porosity are correlated for nonzeolitic materials at Yucca Mountain (Peters, *et al.*, 1984). Figure 21 shows saturated hydraulic conductivity versus porosity data for nonzeolitic materials. The formula for generating saturated hydraulic conductivity shown by the regression line is

$$\ln k_s = -27.042 + 26.526\phi + 2.6343 g(), \tag{16}$$

where $g()$ is the unit gaussian deviate. There appears to be quite a bit of scatter for low porosity samples due to measurement errors for low conductivities and microfractures for some of the densely welded samples. A total of 180 data points from seven sources are used with no obvious bias in any of the studies. The linear correlation coefficient is 0.85.

Saturated conductivity and porosity data for zeolitic materials are shown in Figure 22. For zeolitic materials, saturated conductivity does not appear to be dependent on porosity but is more likely dependent on the degree of zeolitization. The formula for zeolitic materials is

$$\ln k_s = -24.021 + 1.8973 g(). \quad (17)$$

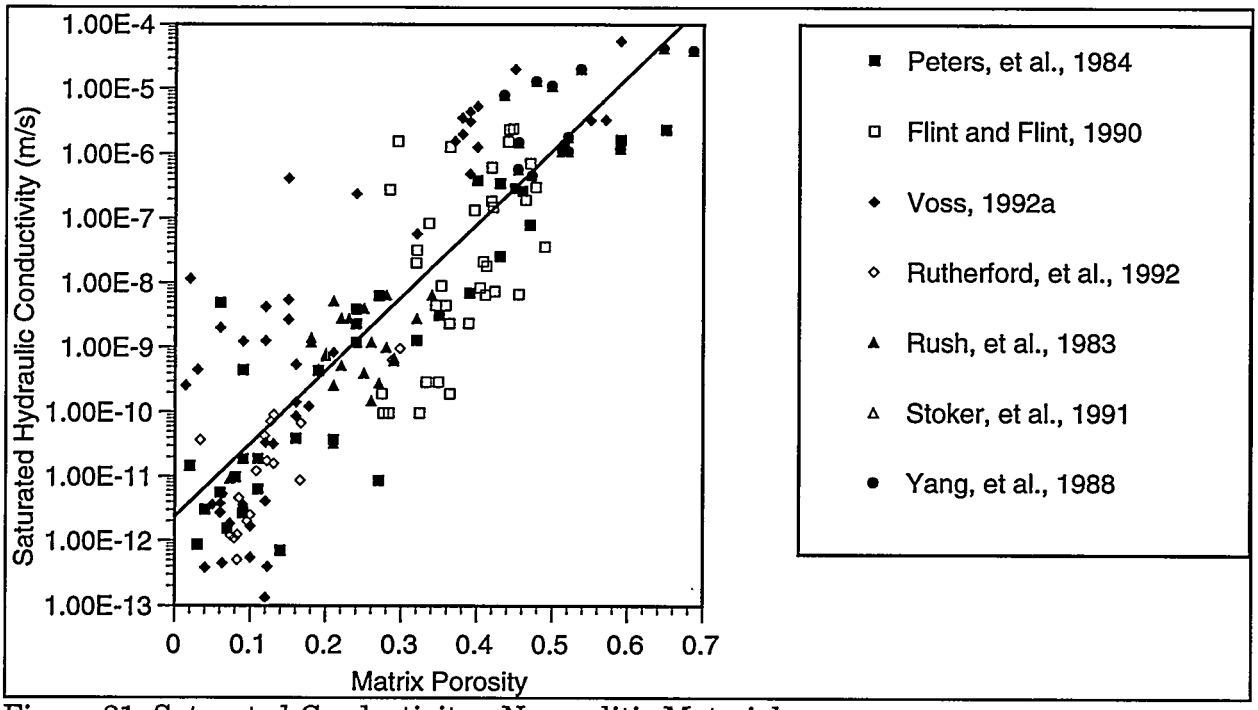


Figure 21. Saturated Conductivity: Nonzeolitic Materials

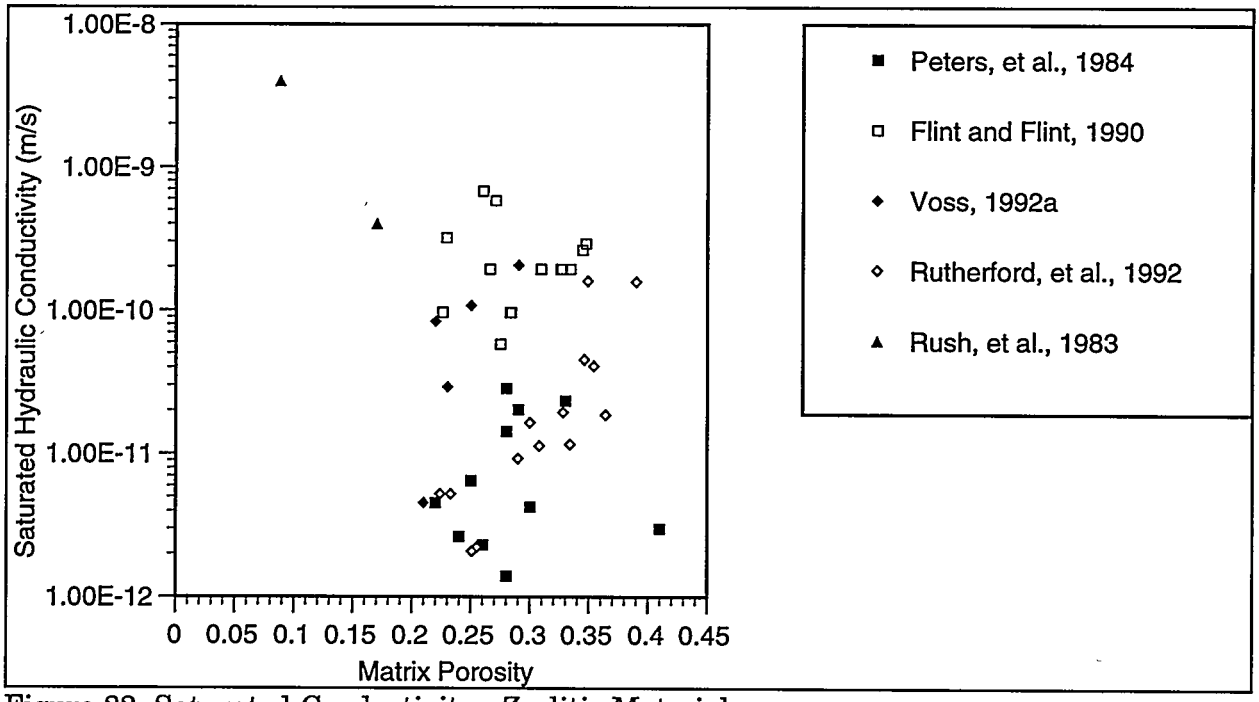


Figure 22. Saturated Conductivity: Zeolitic Materials

The data from Peters, *et al.* (1984) and Rutherford, *et al.* (1992) show a bias towards lower conductivities although it is possible the bias is due to how the samples were selected for testing. The two data points from Rush, *et al.* (1983) may not be properly classifed as zeolitic.

There are 46 data points, and considering the differences in the results of the 5 studies, there still remains some uncertainty about zeolitic materials.

The data for average pore size are split up into the three categories used for the indicator geostatistics. The welded and nonwelded materials are not lumped because then it is difficult to accurately represent the entire range of porosity. Also, the regression then appears very sensitive to outliers. In general, outliers are a problem as there are a few samples in each category that have relatively high average pore sizes. For the welded category, the outliers are probably samples with a significant volume of microfractures, whereas the zeolitic outliers may not be "fully" zeolitic. The average pore size versus porosity for the three materials is shown in Figures 23 through 25. The regression lines are given for the welded, nonwelded, and zeolitic materials, respectively, by

$$\bar{r}=0.033238+0.86068\phi, \tag{18}$$

$$\bar{r}=-1.6086+8.6702\phi, \tag{19}$$

$$\bar{r}=-0.094062+0.46144\phi. \tag{20}$$

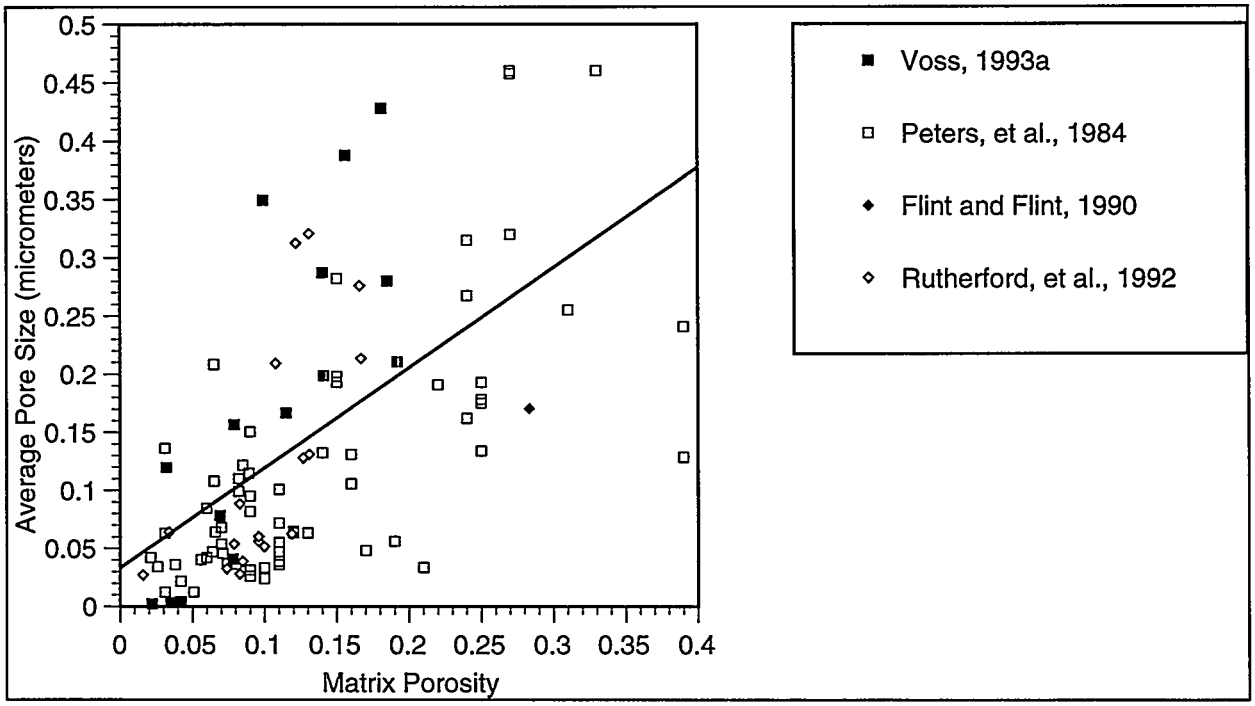

Figure 23. Average Pore Size: Welded Materials

The breakpoint between welded and nonwelded units for the calibration problem is taken to be a porosity of 21%. The average pore size is a derived property obtained by fitting an incomplete gamma function to moisture retention data. The scatter and outliers may be due to errors or bias introduced in the fitting process.

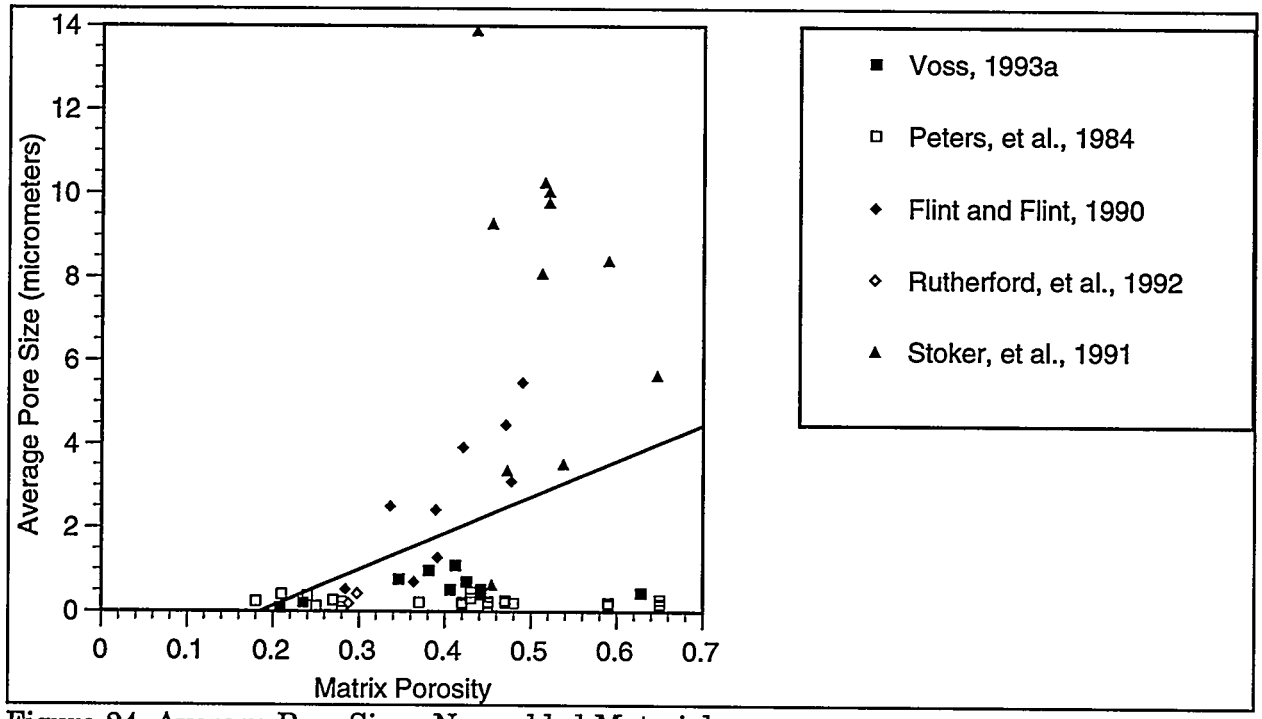

Figure 24. Average Pore Size: Nonwelded Materials

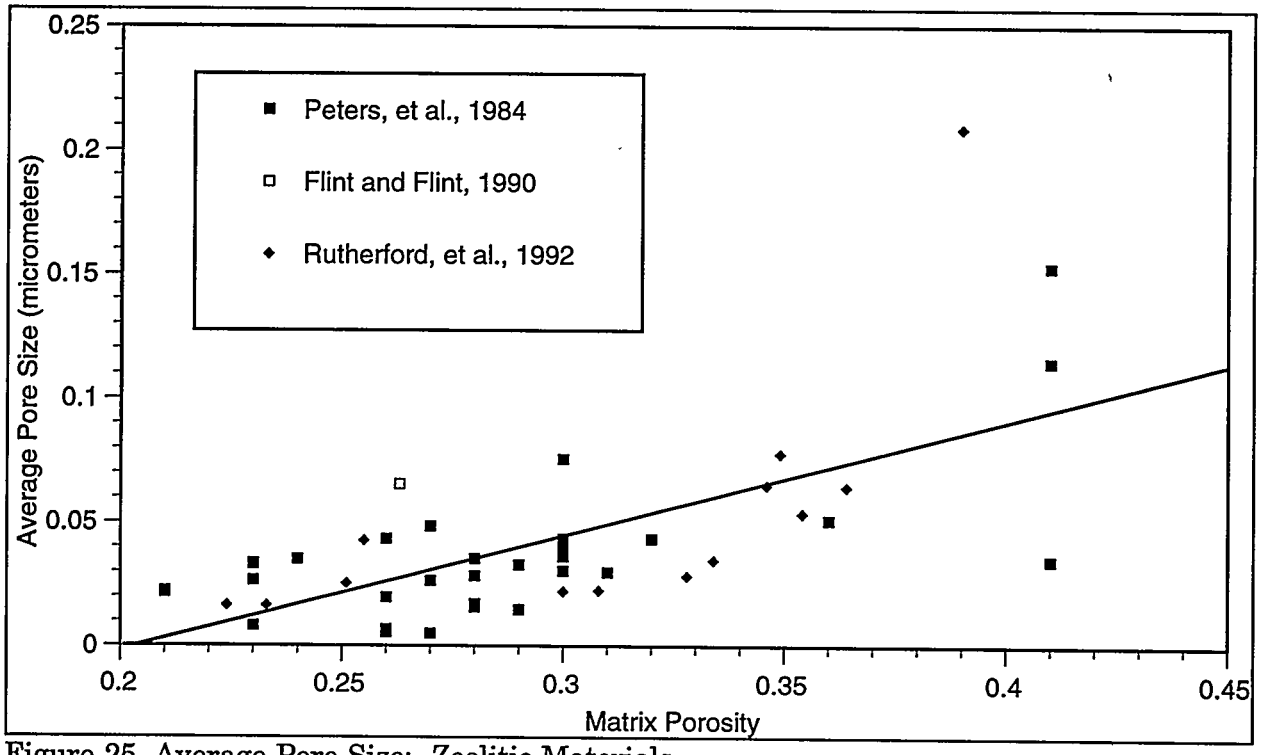

Figure 25. Average Pore Size: Zeolitic Materials

The standard deviation of the pore size distribution versus average pore size is shown in Figure 26. There appears to be a strong relationship, although both parameters are derived from moisture retention data and the relationship could be an artifact of the numerical fit. The relationship is given by

$$\ln \sigma(r)=0.27909+1.0537\ln \bar{r}+0.42042g(). \quad (21)$$

For zeolitic materials the data are shown in Figure 27 and the regression is given by

$$\ln \sigma(r)=1.0196+1.1896\ln \bar{r}+0.13780g(). \quad (22)$$

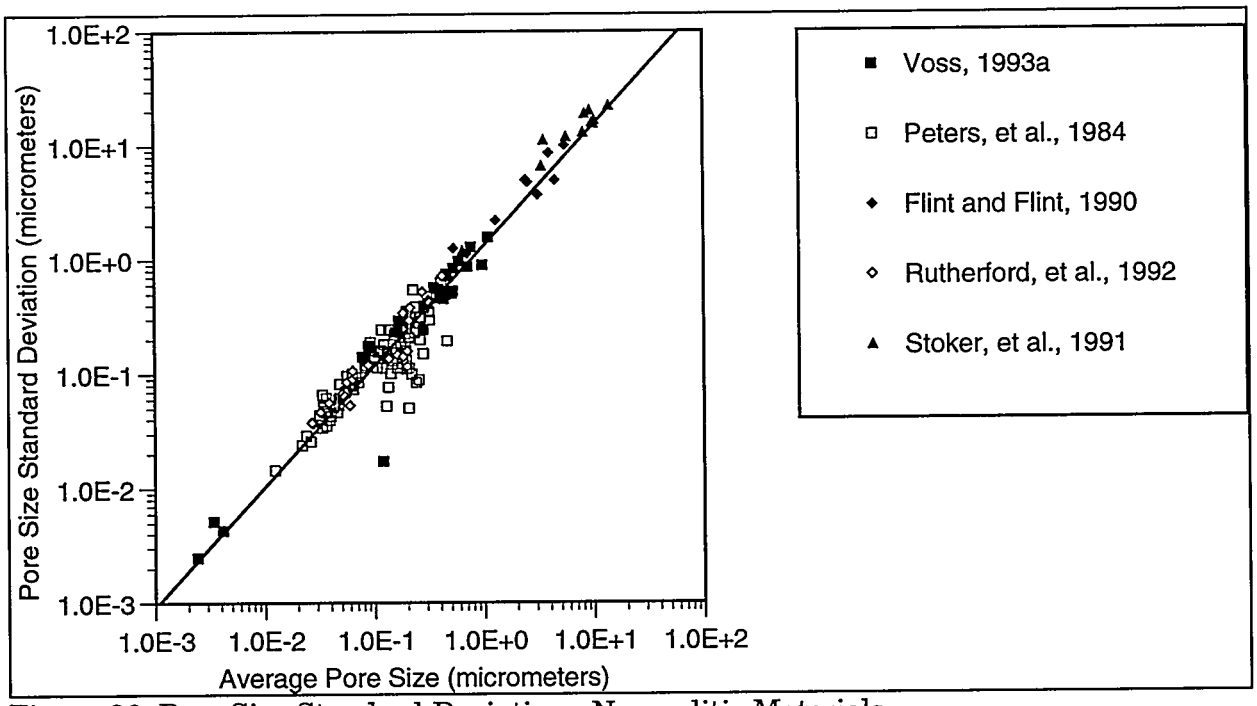


Figure 26. Pore Size Standard Deviation: Nonzeolitic Materials

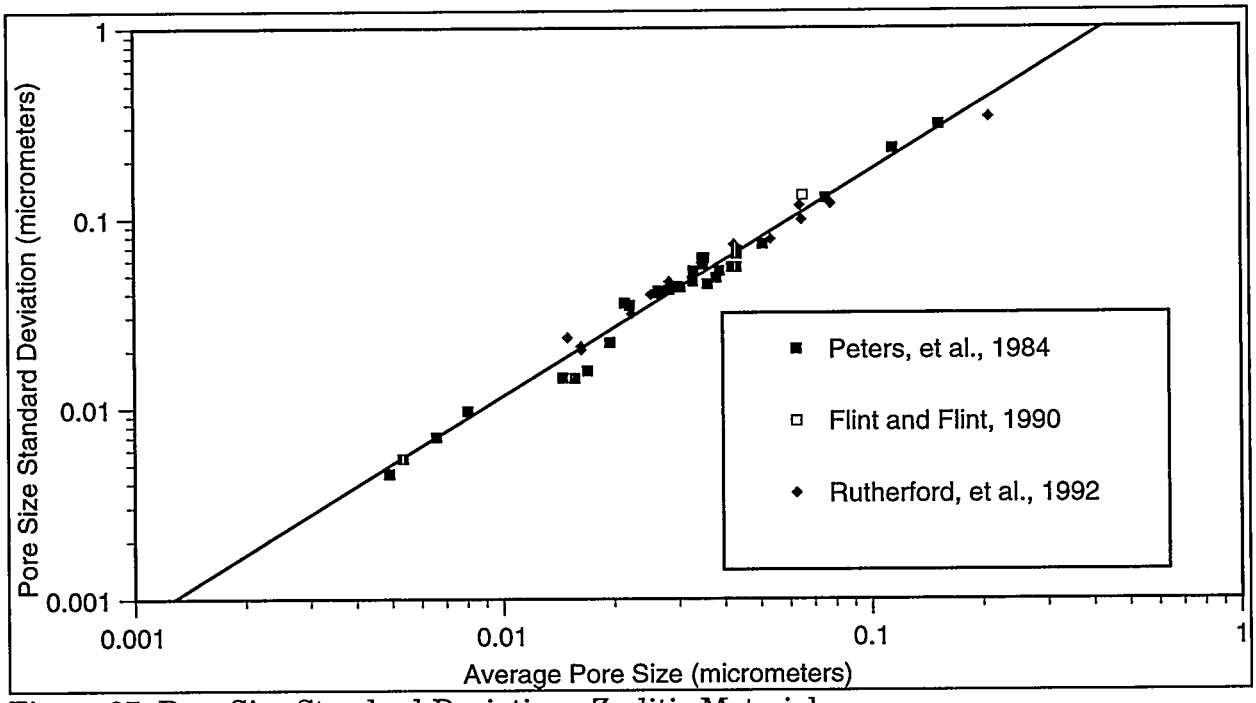


Figure 27. Pore Size Standard Deviation: Zeolitic Materials

Using the expected values for the average pore size and standard deviation of the pore size, representative core-scale moisture retention curves are constructed and shown in Figure 28. Three curves for matrix materials are shown with each category represented. The nonwelded Paintbrush bedded subunit desaturates first among the matrix materials while the zeolitic unit desaturates at the highest suction pressures. The Topopah Spring main subunit shows a steeper curve than the other two matrix materials. The corresponding volume-weighted pore size distributions are shown in Figure 29. Although all three approach infinity as the pore diameter decreases, the zeolitic unit has the smallest pores while the nonwelded Paintbrush bedded subunit pore size distribution is weighted more toward large pores.

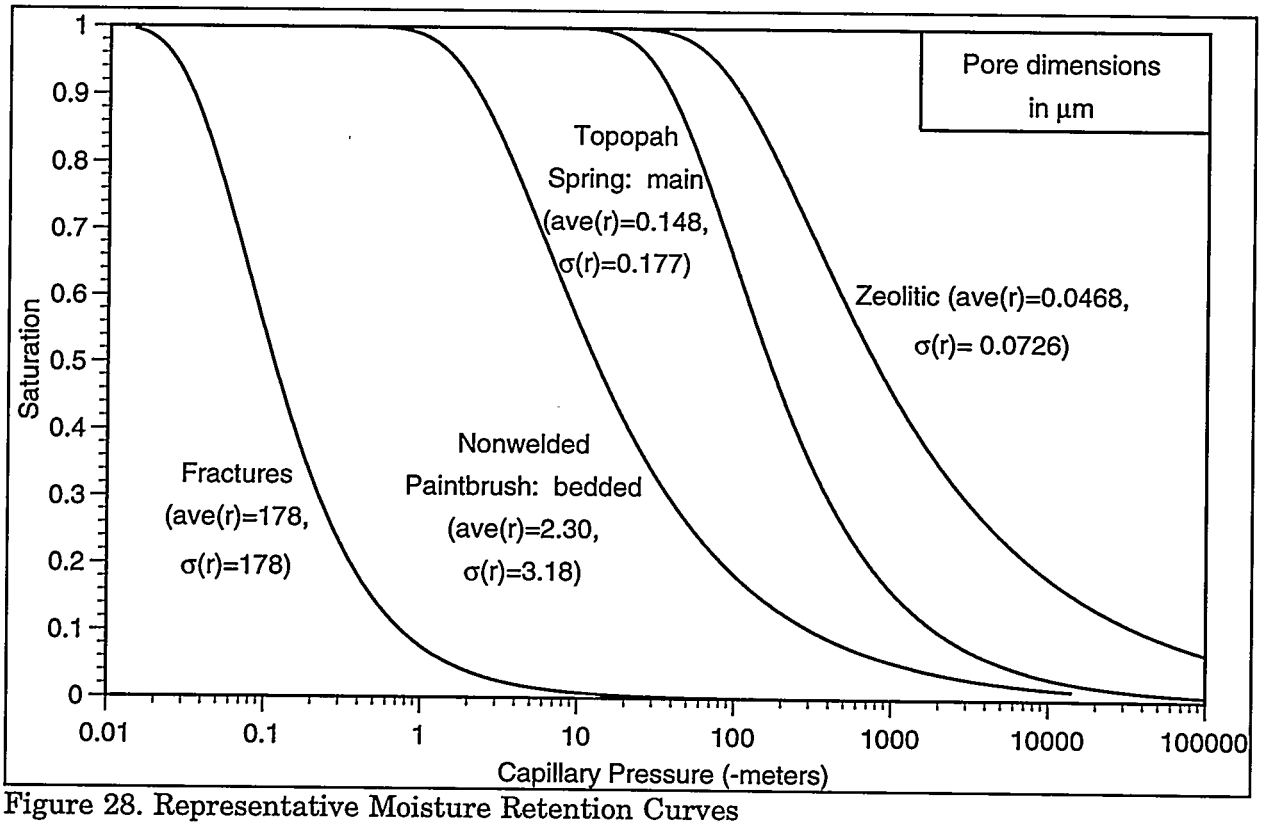

Figure 28. Representative Moisture Retention Curves

The unsaturated conductivity requires computation of $k_r \equiv k/k_s$, where $k$ is the unsaturated hydraulic conductivity. The most common methods are due to Mualem (1976) and Brooks and Corey (1966). The method due to Mualem requires integration of $s = F(\psi)$ which is computed analytically for the above form of the van Genuchten function but would require numerical integration for the incomplete gamma function. The Brooks and Corey method requires the Brooks-Corey constant $\varepsilon_m$

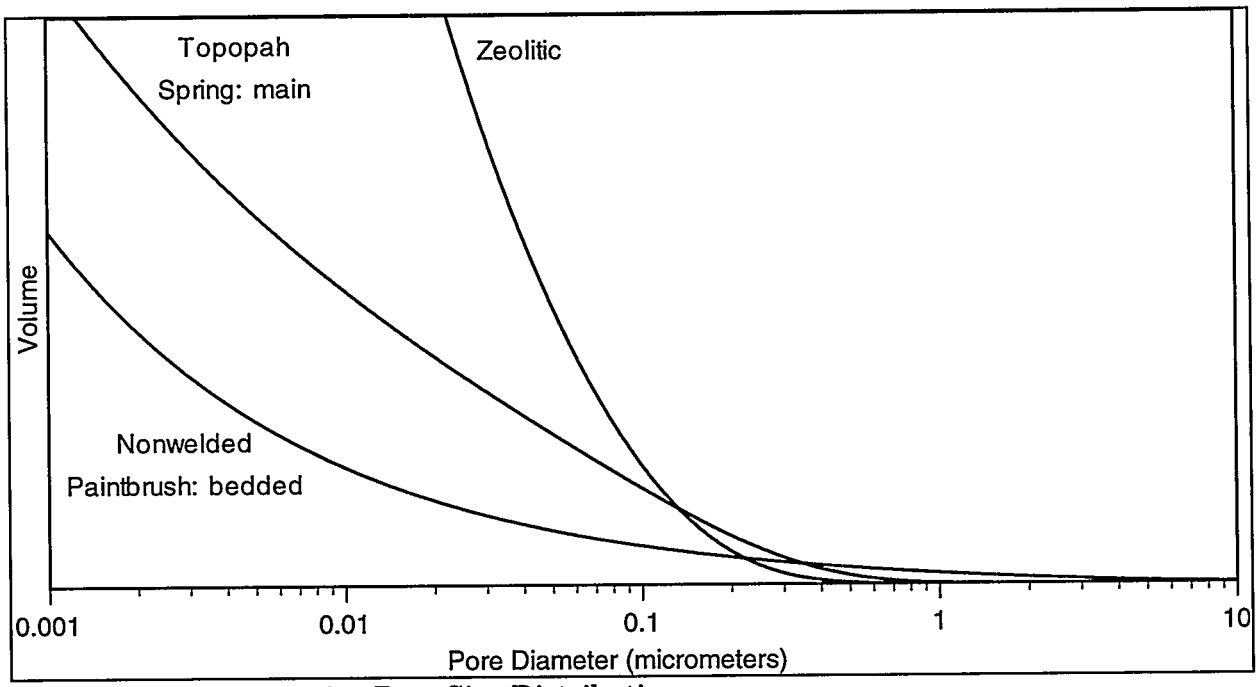

Figure 29. Representative Pore Size Distributions

$$k_r = \left( \frac{s - s_r}{1 - s_r} \right)^{\varepsilon_m}. \tag{23}$$

Klavetter and Peters (1986) estimated the Brooks-Corey constant for five nonzeolitic samples from USW G-4 from the van Genuchten function. The sample from Prow Pass is included in this group because it is partially welded, not noted as zeolitic, and fits with the other data as can be seen in Figure 30. The regression for $\varepsilon_m$ is

$$\varepsilon_m = 6.4835 - 5.3143\phi + 0.75144g(). \tag{24}$$

Klavetter and Peters also examined one zeolitic sample and determined a Brooks-Corey constant of $\varepsilon_m$ = 6.4. Representative unsaturated conductivity curves are shown in Figure 31 calculated using Equation (23) and the incomplete gamma function.

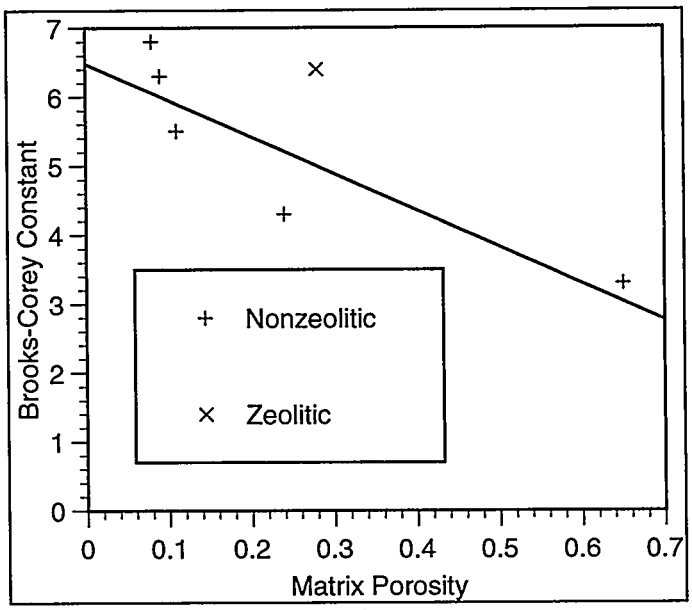

Figure 30. Brooks-Corey Constant

## Upscaled Properties

The numerical flow code requires material properties for large-scale blocks

in order to make the problem computationally tractable. The available data for rock matrix properties are on small core samples in order to allow data to be collected in a reasonable time. For heterogeneous materials the properties are scale dependent and thus the issue of upscaling properties from that of data collection to that used in flow simulation must be addressed.

Upscaling material properties usually involves some type of averaging process. The proper scaling (averaging) formula is dependent on the material property and for most material properties there is uncertainty about an appropriate scaling formula. However, if the range of values (the heterogeneity) can be reduced then there is less opportunity for error in the averaging process and more confidence in upscaling. The adaptive grid algorithm discussed earlier minimizes heterogeneity within elements and reduces the size of elements in highly heterogeneous areas. Reducing the size of elements also increases confidence by limiting the area over which scaling errors may apply.

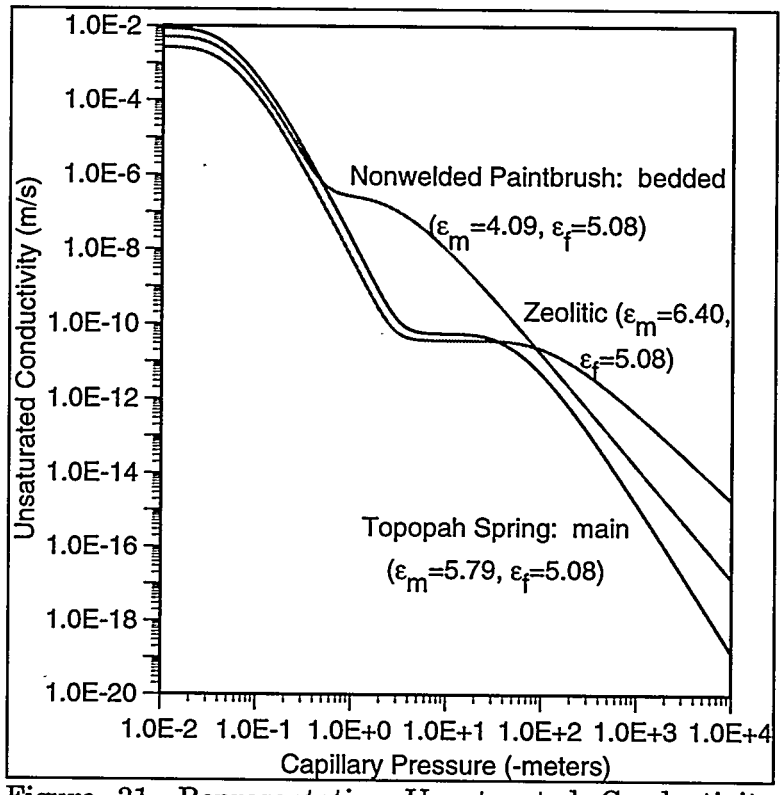

Figure 31. Representative Unsaturated Conductivity Curves

The upscaling procedure for porosity is to compute the linear average of all the porosities within an element to get an element porosity. Results of the upscaling for the seven realizations of the calibration problem (north-south cross section) are shown in Figure 32 and for the east-west cross section are shown in Figures 33 through 35. For saturated conductivity, geometric averaging is used (Warren and Price, 1961)

$$k_s^{\,e}=\exp\left[\frac{1}{n}\sum_{i=1}^{n}\ln\left(k_s\right)_i\right]. \qquad (25)$$

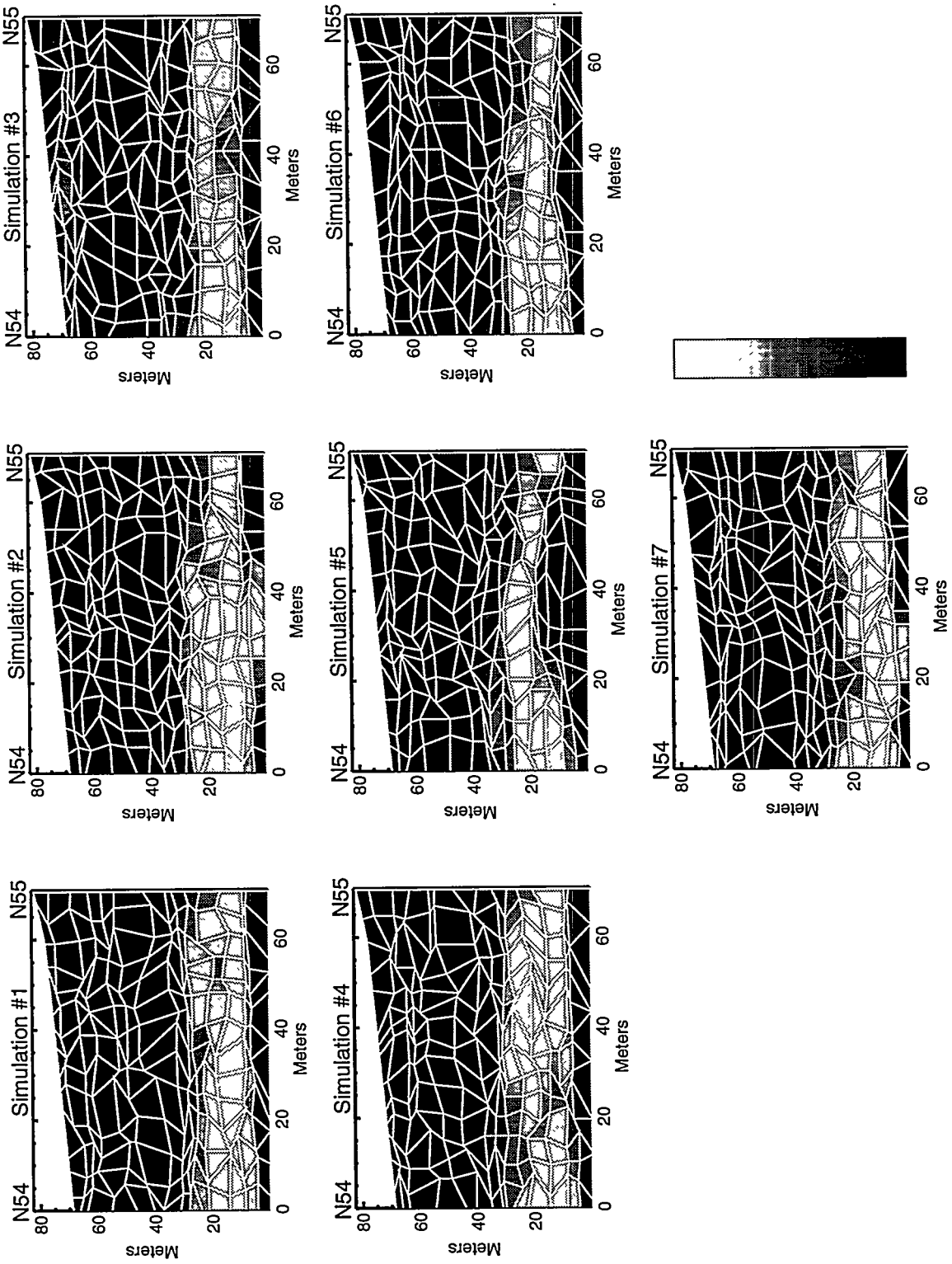


Figure 32. Element Porosities for the Calibration Problem

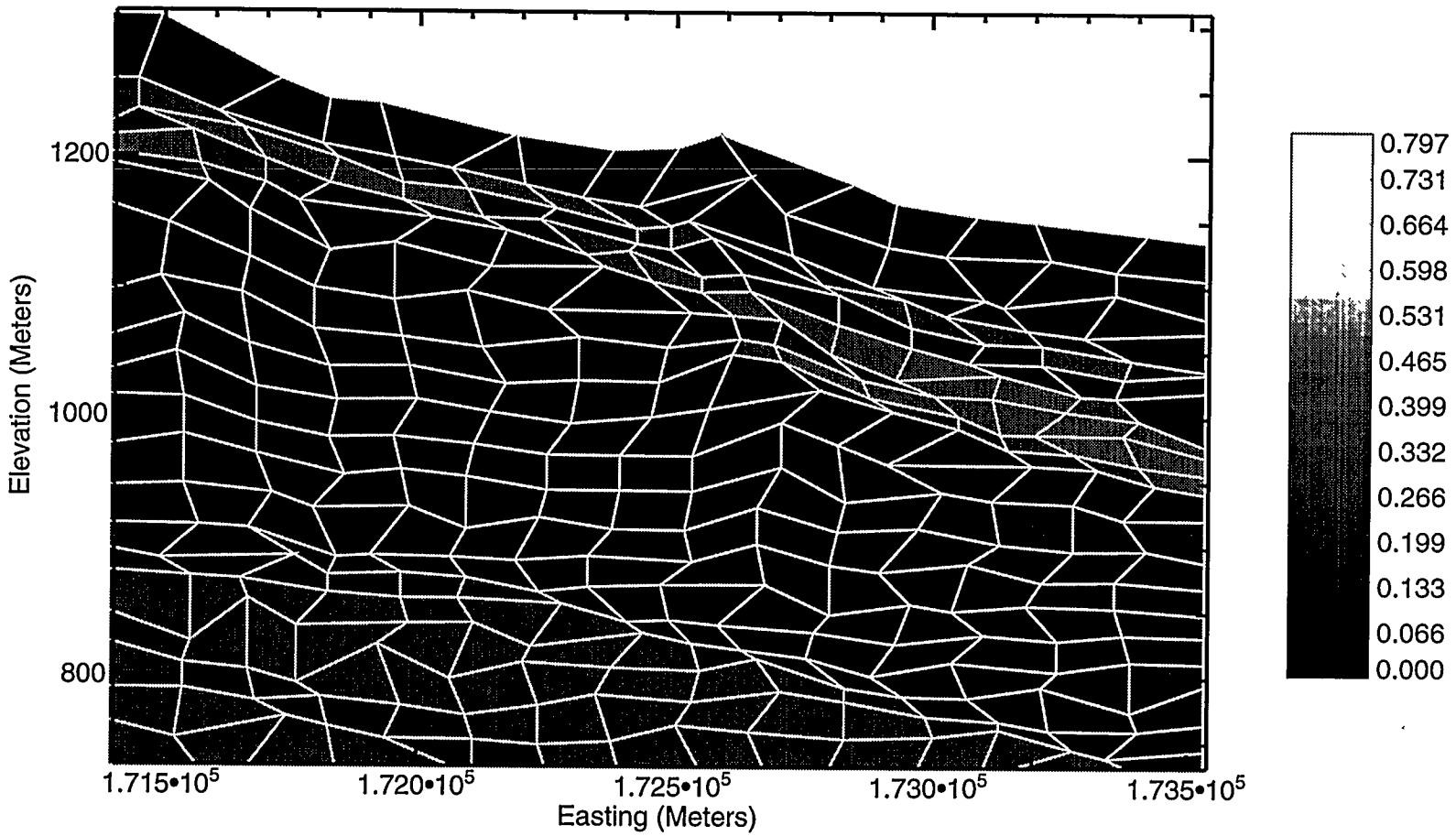


Figure 33. Element Porosities for the INTRAVAL Problem, Simulation #1

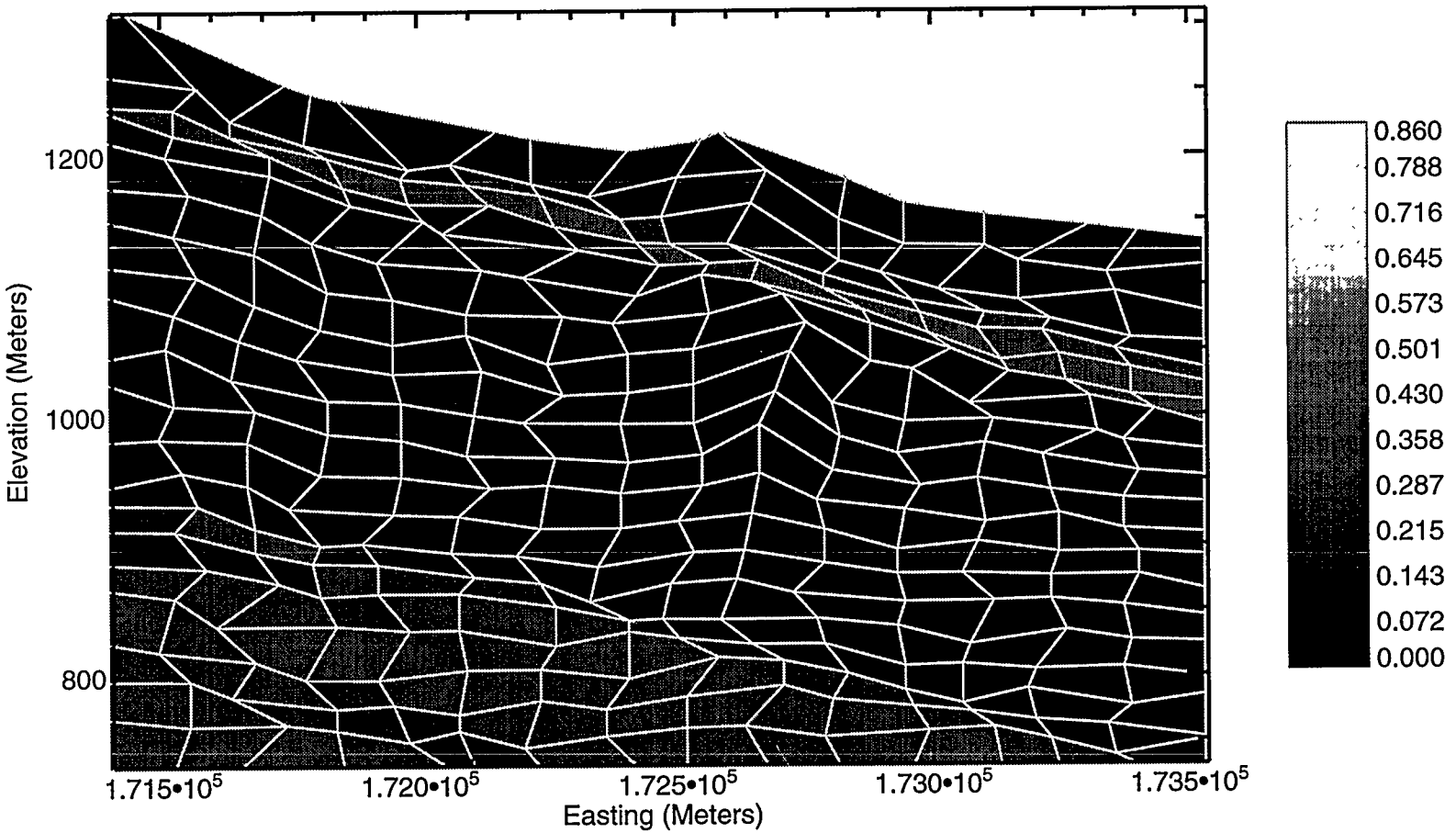


Figure 34. Element Porosities for the INTRAVAL Problem, Simulation #2

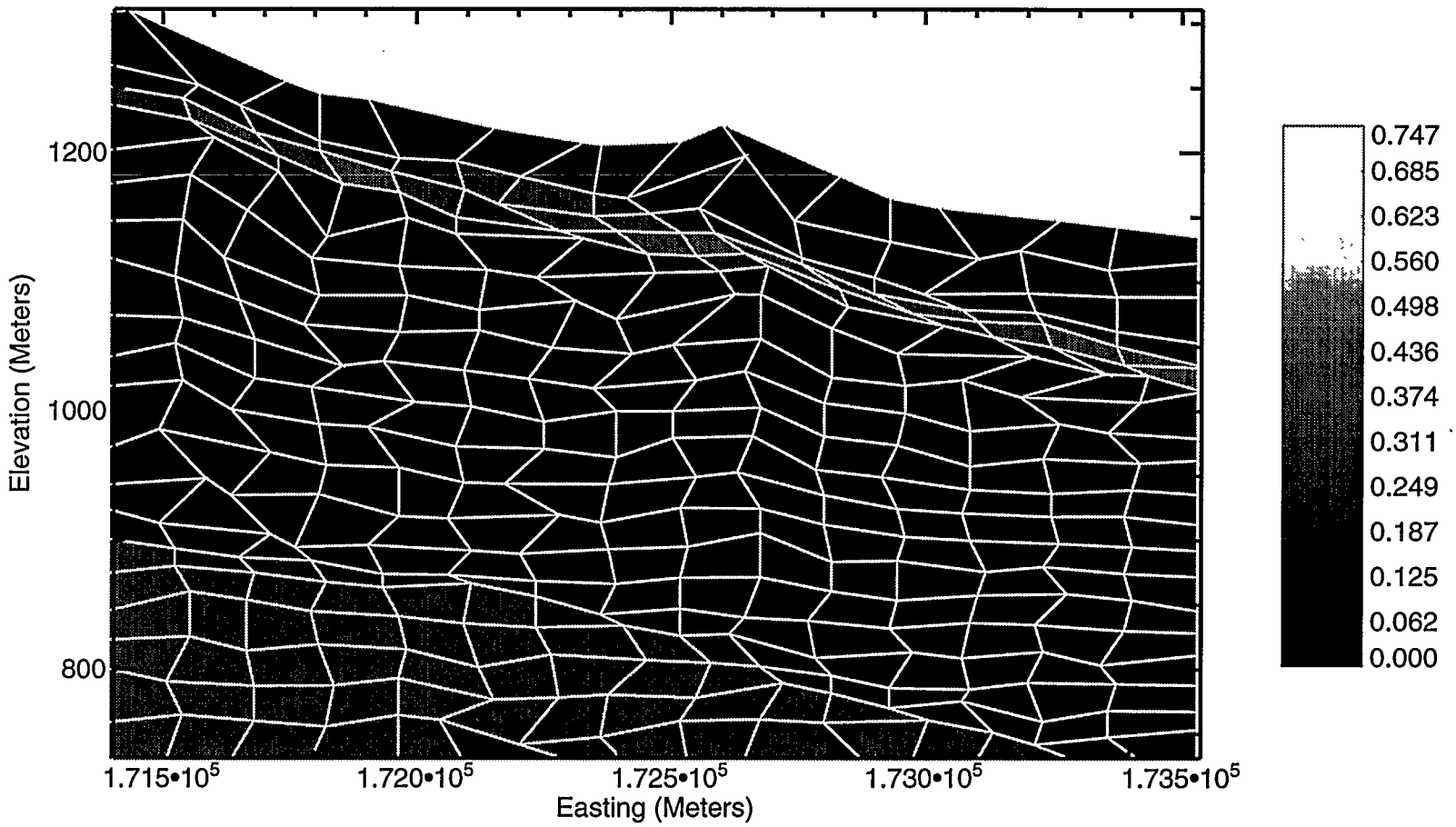


Figure 35. Element Porosities for the INTRAVAL Problem, Simulation #3

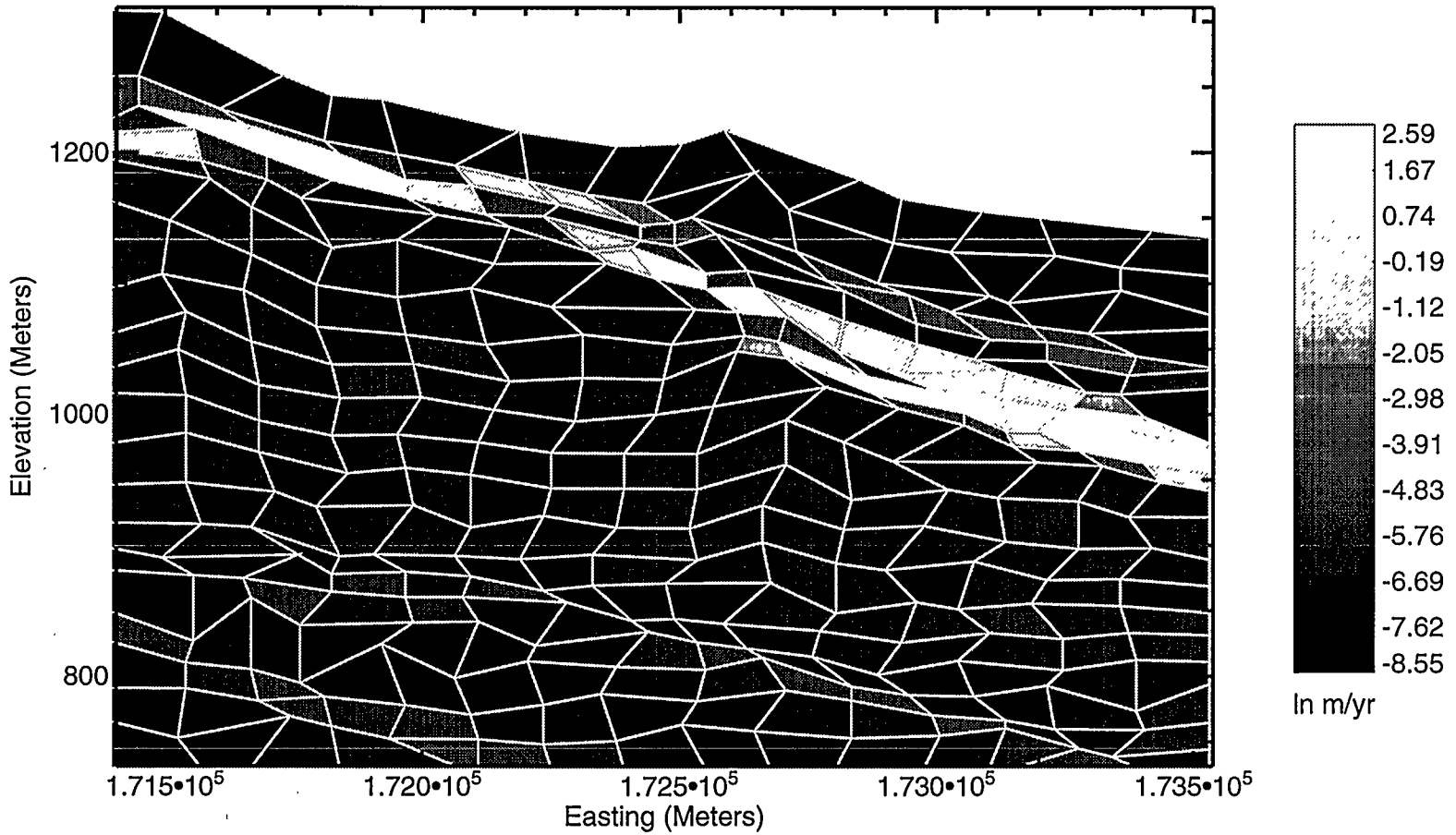


Figure 36. Element Saturated Conductivities for the INTRAVAL Problem, Simulation #1

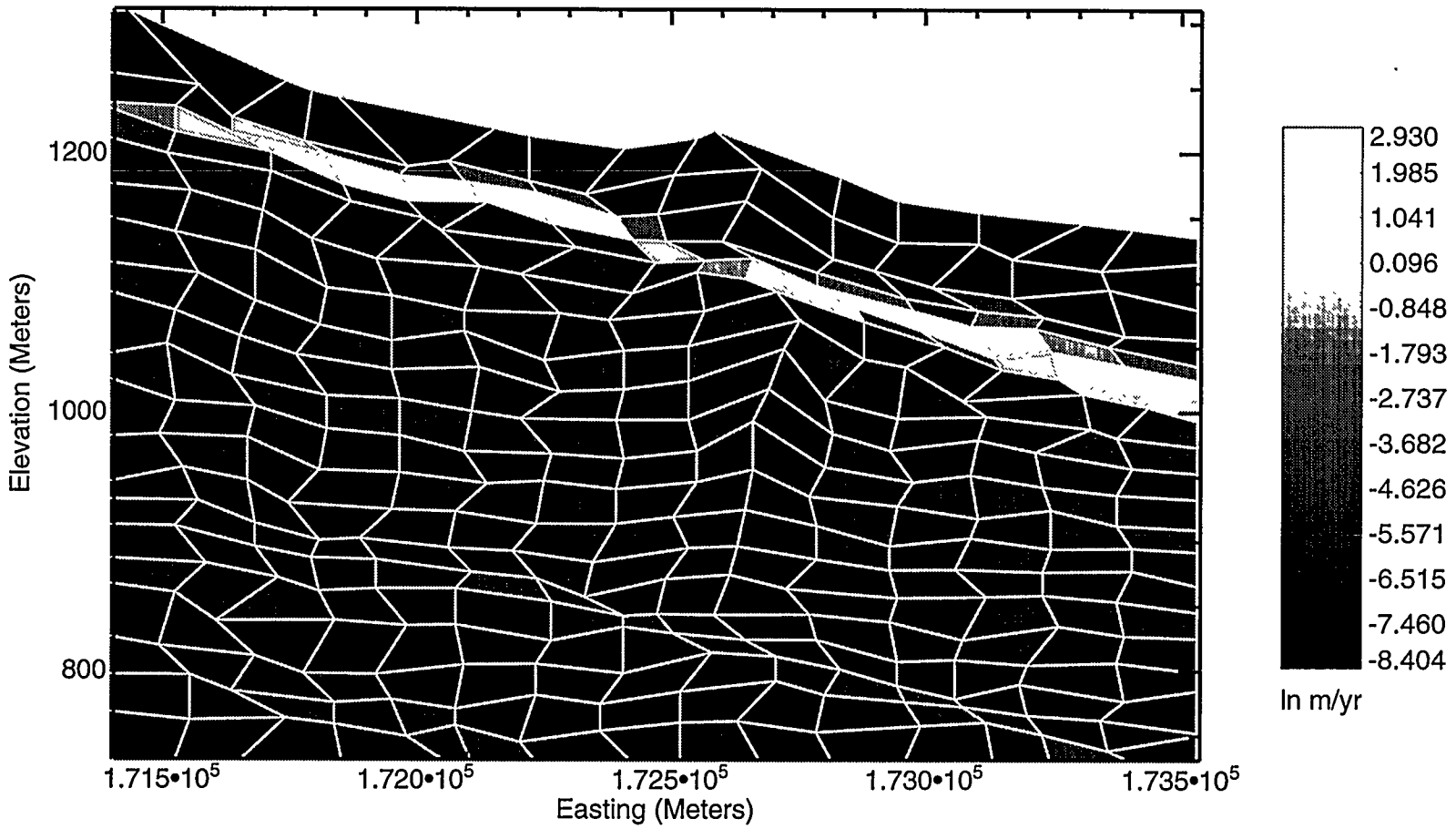


Figure 37. Element Saturated Conductivities for the INTRAVAL Problem, Simulation #2

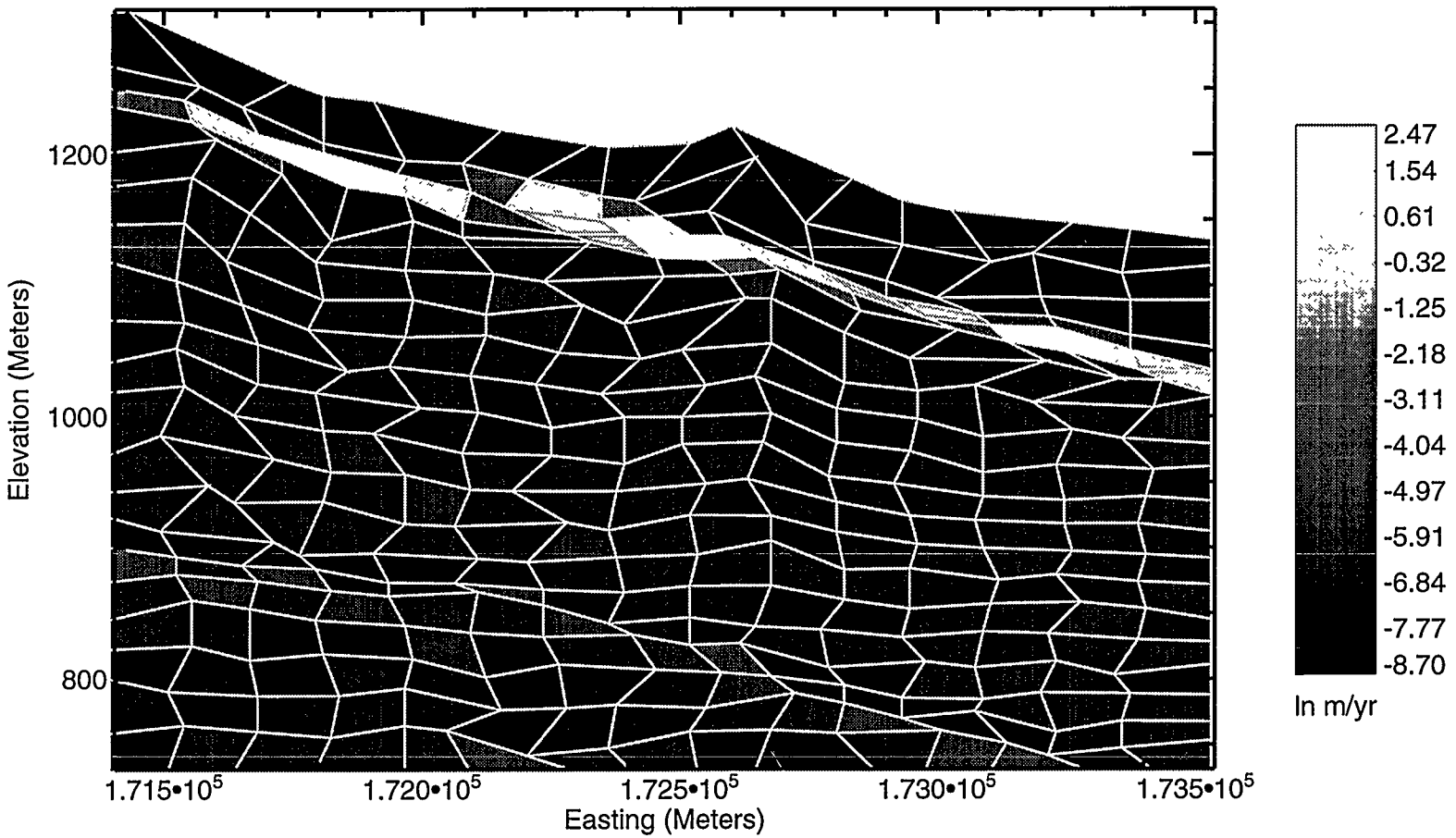


Figure 38. Element Saturated Conductivities for the INTRAVAL Problem, Simulation #3

The upscaled saturated conductivities for the east-west cross section are shown in Figures 36 through 38. The average pore size upscaling uses a volume (porosity) weighted linear averaging

$$\bar{r}^e = \frac{1}{\phi^e n} \sum_{i=1}^{n} \phi_i \bar{r}_i. \tag{26}$$

Using the similiarity of the computation of standard deviation with moment of inertia, then the standard deviation of the pore size distribution can be scaled using the porosity-weighted parallel axis theorem (Popov, 1976)

$$\sigma(r^e) = \left\{ \frac{1}{\phi^e n} \sum_{i=1}^{n} \phi_i \left[ \sigma(r_i) + \left( \bar{r}^e - \bar{r}_i \right)^2 \right] \right\}^{1/2}. \tag{27}$$

The random error term in the average pore size is best omitted in applications when computing Equation (27) since the upscaling is very sensitive to the difference in the parentheses. An implicit assumption made by the upscaling process is that the element pore size distribution can be represented by a gamma function; e.g., the distribution is not bimodal. The Brooks-Corey coefficient is volume averaged over the element. In addition, scaling of the moisture retention curve results in an implicit scaling of the unsaturated conductivity curve.

## Fracture Properties

A composite-porosity model is employed in the flow simulator. The INTRAVAL data set did not include data for fracture properties and there is considerable uncertainty due to difficulties in measuring fracture properties in-situ. A linear regression of expected matrix and fracture porosities from the first seven units of TSPA 1993 (Schenker, *et al.*, 1994) yields

$$\phi_f = 0.0026192 - 0.0058455\phi_m, \ \phi_f \geq 0. \tag{28}$$

The regression is shown in Figure 39.

The fracture conductivities are obtained from bulk conductivities for TSPA 1993 (Schenker, *et al.*, 1994). The log base 10 expected values are averaged over the element to account for elements with multiple units. For the calibration problem the geometric average for the first three units (382 meters/year) is used. The expected values for apertures in TSPA 1993 do not vary much for the first seven units, so their average value of $\bar{r}$ = 178 micrometers is used. Examining the coefficients of variation shows they are all grouped near

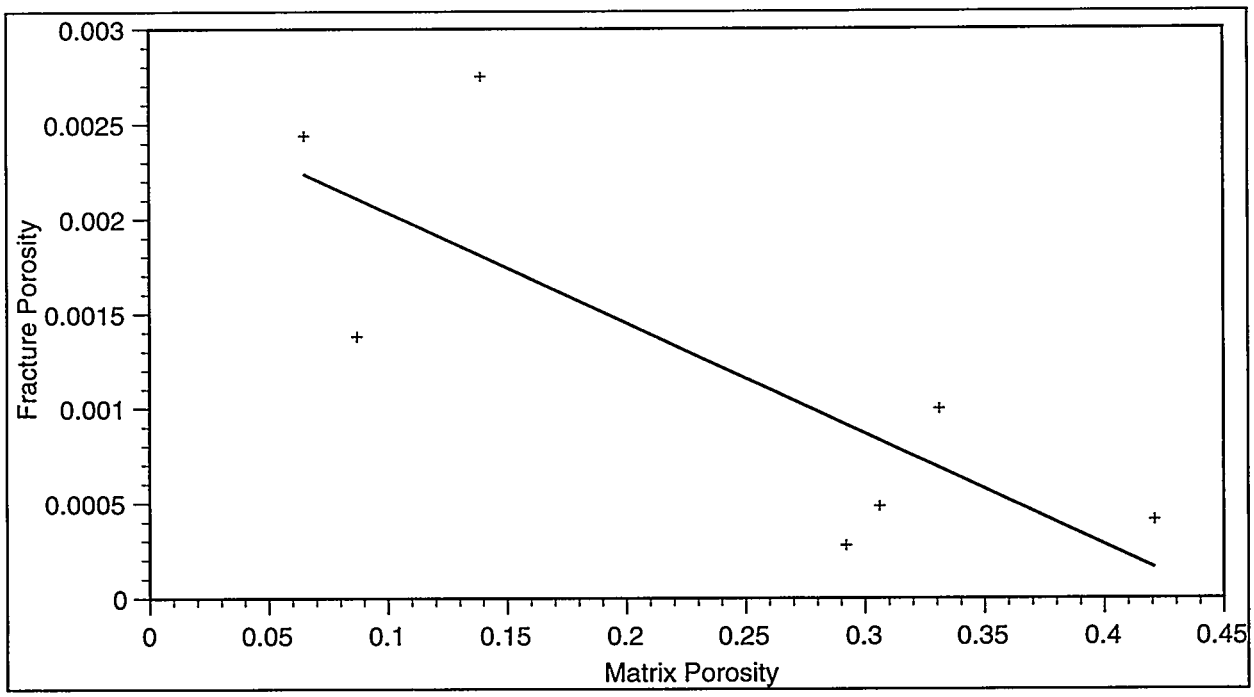

Figure 39. Fracture Porosity

1.0 which implies an exponential distribution. Then the gamma function parameters are $\alpha$ = 1.0 and $\lambda$ = 0.00562 and the moisture retention curve is shown in Figure 28. Fitting a van Genuchten curve to the incomplete gamma function (see Figure 20) results in $\alpha$ = 15.097, $\beta$ = 1.9638, and $s_r = 0$. Following Klavetter and Peters (1986), then the Brooks-Corey constant is calculated as $\varepsilon_f = 5.08$.

# Flow Simulation

Solution of the partial differential equations governing flow through porous media requires their approximation (discretization) on a finite dimensional space in order to allow computation. Most approximations (finite elements and finite differences) involve the use of a mesh in the discretization. As long as the consistency condition is satisfied, any of the methods for discretization will converge to the solution of the partial differential equation as the mesh becomes finer in an appropriate fashion. Thus, in this sense, all methods for discretization are equivalent; however, in a finite-dimensional space each method for discretization can preserve only some of the properties of the partial differential equation. Understanding the goals of the modeling can allow the choice of a method of discretization that preserves the important properties of the partial differential equation. A description of the properties of the method of discretization are contained in the section on theory. A derivation of the discretization method is contained in Appendix A.

The partial differential equations to be solved are nonlinear due to the dependence of the unsaturated conductivity on pressure head. The nonlinear nature is often quite severe and a source of problems for many flow codes. A discussion of the quasi-Newton method that allows robustness and the nonlinear solvers is in the section on nonlinear solvers. The nonlinear solvers each require linear solvers which are discussed in the linear solver section.

Calibration of the modeling technique requires comparison of the model solutions with measured data such as the in-situ saturations. The modeling technique employed eschews the typical inverse approach of matching saturations, but attempts to use the saturation measurements as data in a forward modeling approach.

Finally, the section on the east-west INTRAVAL problem discusses the solution approach on a much larger domain. The initial results predicted saturations at USW UZ-16 before saturation data were made available. The results in this report have been further debugged and cleaned up after the data were released, but no substantial changes in the approach were made.

## Theory

Consider a domain, $\Omega$, with a piecewise continuous boundary $\Gamma$. The steady state flow problem is given by mass conservation and Darcy's Law for a spatial dimension of $n$ by

$$\nabla\cdot\left[\rho(\psi)k(\psi)\nabla(\psi+x_n)\right]=0,\ \mathbf{x}\in\Omega, \tag{29}$$

where $\rho$ is the density, $k$ is the unsaturated conductivity, $\psi$ is the capillary pressure head and $x_n$ is the elevation. The unsaturated conductivity is a function of pressure and the major source of the nonlinearity. The second order partial differential equation can be split into two coupled first order differential equations

$$\begin{aligned} \mathbf{q} &= -k(\psi)\nabla(\psi + x_n), \\ \nabla\cdot(\rho\mathbf{q}) &= 0, \end{aligned} \tag{30}$$

where the first equation is Darcy's Law and the second is conservation of mass. The boundary conditions considered are a mix of Dirichlet and Neumann where $\Gamma = \Gamma_d + \Gamma_n$ and

$$\begin{aligned} \psi &= \psi_0(\mathbf{x}), \ \mathbf{x} \in \Gamma_d, \\ \mathbf{q}\cdot\mathbf{n} &= q_0(\mathbf{x}), \ \mathbf{x} \in \Gamma_n, \end{aligned} \tag{31}$$

where $\mathbf{q}$ is the Darcy flux and $\mathbf{n}$ is the normal to the boundary.

Only the liquid phase is considered in the present approach. Gas and water vapor flow are assumed to be primarily in the fractures. Where the liquid is located solely in the matrix, entrapment of gas is unlikely. However, as the matrix becomes saturated and fracture flow is initiated, gas entrapment may occur. If the zone of saturation is relatively small, it is likely that other fracture pathways exist which bypass the locally saturated zone and gas entrapment can be avoided. Vapor phase transport of water may be significant but should not be sensitive to zones of local saturation as long as the zones are relatively small.

The first step in the numerical solution of porous media flow is discretization of the differential equation. Finite element methods approximate the solution on elements in terms of basis functions. In order to assemble the global matrices, the approximations must be linked in terms of continuity of the solution between elements. Classical approaches enforce continuity of $\mathbf{p}$, the approximation of $\psi + x_n$, which are called primal methods. Dual methods enforce continuity of normal flux where $\mathbf{q} = \{q^1, q^2\}$ as shown in Figure 40. In the case of local saturation of an element, saturations and pressures differ markedly between adjacent elements. Enforcing continuity of pressure suppresses local saturation since the pressures at the common nodes must represent both elements. Enforcing continuity of normal flux allows discontinuous pressure across element boundaries which permits local saturation to occur. Primal methods require nodes to be clustered near material interfaces and near channeling (Dudley, *et al.*, 1988). Furthermore, the nonlinearity in unsaturated conductivity can cause two elements with very similar hydrologic properties to have widely different

conductivities and act like a material interface. A numerical method based on the dual approach is the dual mixed finite element method (Robey, 1990 and Roberts and Thomas, 1990). A special finite difference method that avoids differencing across material interfaces (Morel, *et al.*, 1990) may also be suited to this type of problem.

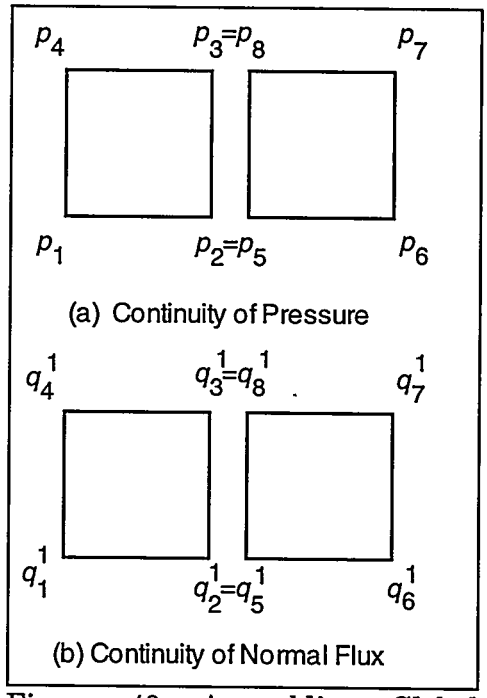

Figure 40. Assembling Global Matrices

For primal methods, the fluxes are approximated in a lower dimensional space than pressures. In the dual approach, pressures are approximated in a lower dimensional space than fluxes (see Appendix A). The potential for higher accuracy in fluxes led to use of the dual mixed finite element method in petroleum reservoir problems (Ewing, *et al.*, 1983). The dual mixed finite element method has also been shown to produce superior streamlines over pressure-based approaches (Kaasschieter and Huijben, 1992). A flow code, DUAL, based on the dual mixed finite element method has been assembled from an existing linear code for use in ground water travel time studies.

The highly nonlinear nature suggests the use of a nonlinear Newton solver. Flow codes based on a nonlinear Newton solver often spend a major amount of time computing the Jacobian matrix. Therefore, one area where significant effort was used to write new code was in computing the Jacobian efficiently, which is detailed in the section on nonlinear solvers. Another area of considerable computing expense for finite element codes is in setting up the element matrices using Gaussian quadrature. For the mixed finite element method it is possible to use analytical integration, which results in very simple expressions for the entries of the element matrices (see Appendix A for details).

While the conductivity varies over the element, an assumption in the derivation of simple expressions for the entries in the element matrices $\mathbf{B}^e$ is that there is an effective conductivity for the element. Computing an effective conductivity for use in the DUAL flow code is an averaging process over the element. Since the conductivity may vary by orders of magnitude across an element, geometric averaging is used

$$(\rho k_{eff})^{-1}=\exp\left[\frac{1}{\rho a_e}\int_e \ln\, k^{-1}(\mathbf{p})\, de\right], \tag{32}$$

where $a_e$ is the area of element $e$. The standard approach in finite elements is to use Gaussian quadrature to approximate the integral (Atkinson, 1978). Then

$$(\rho k_{eff})^{-1}=\exp\left[\frac{1}{4\rho}\sum_{i=1}^{2}\sum_{j=1}^{2}\ln\ k^{-1}\left(\psi(\xi_i,\eta_j)\right)\right], \tag{33}$$

where $\xi = \eta = \{-0.5773502692,0.5773502692\}$ are the vectors of Gauss points used for Gaussian quadrature on the master element shown in Figure 12. Note that the averaging process becomes more suspect as the range of conductivities in an element increases. Also, applying nonlinear optimization can result in the pressures at the four Gauss points being driven such that an appropriate conductivity is achieved for the element. In particular, the nonlinear optimization may drive part of the element into fracture flow to obtain conductivities consistent with the rest of the model; the pressures within the element then no longer have physical interpretations but represent a continuum between matrix flow and fracture flow. Finer resolution of the flow grid is usually appropriate in such elements to determine the occurrence of a locally saturated region (element).

## Nonlinear Solver

The degree of nonlinearity in the unsaturated flow at Yucca Mountain is highly dependent on the material parameters for the matrix and the fractures as well as the flow regime encountered; i. e., the region of the unsaturated conductivity curve where the solution lies. For example, often the point at which fracture flow is initiated possesses a large degree of nonlinearity. Thus the success of a nonlinear solver is very problem dependent and the nonlinear solver must be developed in conjunction with the models. The present goal is a robust and efficient nonlinear solver that can be expected to perform well for most problems.

The nonlinear solver employed by DUAL is based on that used for the DYNAMICS module in TOSPAC, a one-dimensional code (Dudley, *et al.*, 1988) which has seen considerable use on Yucca Mountain problems. Ground water travel time for pre-emplacement calculations is typically considered a steady state problem since treating it as a dynamic problem would introduce the unanswerable question of the proper initial condition. For post-emplacement calculations, a dynamic problem is encountered; however, first a steady state problem typically is solved for the initial condition. Moreover, it is not difficult to add a time-stepping algorithm to DUAL. Solving the steady state problem corresponds to large time steps for the dynamic problem and can be expected to be more demanding than the dynamic problems. A Newton solver is employed with an optional Picard solver used for the

initial guess. In addition, a line search method is used to adjust the Newton step to avoid nonlinear instability.

The Picard solver is a simple fixed point method where the conductivity is determined using the pressure at the previous iteration. From use with the one-dimensional TOSPAC, the Picard solver often does not converge but is useful in providing an initial guess. Presently DUAL uses the initial guess from the Picard solver until the initial residual of the linear equations for the Newton step becomes large whereupon it is used on every other Newton iteration. The nonlinear equations are linearized using the current unknowns at step $n$ and then the unknowns at step $n+1$ are determined using the equation (see derivation in Appendix A)

$$\begin{bmatrix} \mathbf{K}(\mathbf{p}^n)\mathbf{B} & \mathbf{D}^T & \mathbf{C}^T \\ \mathbf{D} & \mathbf{0} & \mathbf{0} \\ \mathbf{C} & \mathbf{0} & \mathbf{0} \end{bmatrix} \begin{bmatrix} \mathbf{q}^{n+1} \\ \mathbf{p}^{n+1} \\ \lambda^{n+1} \end{bmatrix} = \begin{bmatrix} \mathbf{g} \\ \mathbf{0} \\ \mathbf{f} \end{bmatrix}. \tag{34}$$

The Newton method solves the equation

$$\mathbf{Js}=-\mathbf{F}, \tag{35}$$

where $\mathbf{J}$ is the Jacobian matrix, $\mathbf{F}$ is the current residual vector, and $\mathbf{s}$ is the Newton step. The Newton solver uses a combination of analytical differentiation and central differencing to calculate the Jacobian in a very efficient manner. Consider partial derivatives with respect to the components of $\mathbf{q}$

$$\frac{\partial}{\partial q_j}\left\{ \begin{bmatrix} \mathbf{K}(\mathbf{p})\mathbf{B} & \mathbf{D}^T & \mathbf{C}^T \\ \mathbf{D} & \mathbf{0} & \mathbf{0} \\ \mathbf{C} & \mathbf{0} & \mathbf{0} \end{bmatrix} \begin{bmatrix} \mathbf{q} \\ \mathbf{p} \\ \lambda \end{bmatrix} - \begin{bmatrix} \mathbf{g} \\ \mathbf{0} \\ \mathbf{f} \end{bmatrix} \right\} = \begin{bmatrix} \mathbf{K}_{jj}(\mathbf{p})\mathbf{B}_j \\ \mathbf{D}_j \\ \mathbf{C}_j \end{bmatrix}, \tag{36}$$

where the single $j$ subscript on a matrix indicates the $j$th column. Thus the first column of submatrices for the Jacobian matrix is identical to that of the Picard matrix. Similiar results are obtained for $\lambda$ and the last column of submatrices. The nonlinearity is in terms of $\mathbf{p}$ so

$$\frac{\partial}{\partial p_j}\left\{ \begin{bmatrix} \mathbf{K}(\mathbf{p})\mathbf{B} & \mathbf{D}^T & \mathbf{C}^T \\ \mathbf{D} & \mathbf{0} & \mathbf{0} \\ \mathbf{C} & \mathbf{0} & \mathbf{0} \end{bmatrix} \begin{bmatrix} \mathbf{q} \\ \mathbf{p} \\ \lambda \end{bmatrix} - \begin{bmatrix} \mathbf{g} \\ \mathbf{0} \\ \mathbf{f} \end{bmatrix} \right\} = \begin{bmatrix} \mathbf{B}\mathbf{q}\dfrac{\partial \mathbf{K}(\mathbf{p})}{\partial p_j} + (\mathbf{D}^T)_j \\ \mathbf{0} \\ \mathbf{0} \end{bmatrix}. \tag{37}$$

Thus the Jacobian matrix is obtained

$$\mathbf{J}=\begin{bmatrix} \mathbf{K(p)B} & \hat{\mathbf{D}}^T & \mathbf{C}^T \\ \mathbf{D} & \mathbf{0} & \mathbf{0} \\ \mathbf{C} & \mathbf{0} & \mathbf{0} \end{bmatrix}, \tag{38}$$

where

$$\left(\hat{\mathbf{D}}^T\right)_j=\mathbf{Bq}\frac{\partial \mathbf{K(p)}}{\partial p_j}+\mathbf{D}^T. \tag{39}$$

$\hat{\mathbf{D}}^T$ is calculated using finite differences. Since $\mathbf{D}^T$ consists of 8x3 blocks, it only takes three sweeps to compute all the differences.

The Newton method achieves very quick convergence near the solution. It is possible to improve the global convergence of the Newton method using a quasi-Newton framework (Dennis and Schnabel, 1983). Once the Newton step is computed, then the residual at the new unknowns is computed and it is decided using global convergence criteria whether to accept the new iteration. If not, then a search is conducted in the direction of the Newton step. A one-dimensional minimization problem results. Currently, a cubic line search is used to conduct the minimization until a solution is obtained that meets the global convergence criteria. Convergence is theoretically guaranteed using a quasi-Newton approach. In practice, very nonlinear problems may never achieve the quick convergence of the Newton method and there also are other numerical difficulties that may occur.

## Linear Solvers

The Picard iteration and Newton iteration both require linear solvers. The matrices are often very poorly conditioned. In addition, often the region of interest is where the Darcy fluxes are relatively small. Iterative solvers are often employed but they resolve only the larger eigenvalues (large fluxes) with any accuracy. Thus experience dictates that it is desirable to use a direct solver for resolving the small fluxes. DUAL uses an efficient direct solver for the Picard iteration and an iterative solver for the Newton step.

Due to the high degree of nonlinearity often encountered, it is advantageous to only approximately obtain the Newton step. Numerical experiments show a residual with relative error of 0.1 to 0.5 often results in fewer nonlinear iterations than more accurate approximations of the Newton step.

The iterative solver used is a biconjugate gradient method for nonsymmetric matrices (Fletcher, 1976). More recent variants, conjugate gradients squared and stabilized biconjugate gradients (van der Vorst, 1992) have been tried without success. Several simple preconditioners have been tried without success since the matrix equations are not diagonally dominant or positive definite. An incomplete LU preconditioner is used in similar applications but is somewhat complicated to implement. Another possibility is to use the Picard solver as a preconditioner to accelerate the biconjugate gradient method instead of just for the initial guess. No preconditioner is used at present because the biconjugate gradient method does not require very many iterations for most problems. This is especially true during the early nonlinear iterations. Another type of iterative solver is a multigrid solver for diffusion problems with highly varying diffusion coefficients (Molenaar, 1992) which may be desirable for large problems.

The direct solver used by DUAL is a null space method (Heath, 1976 and Robey, 1992). This solver is discussed in detail in Appendix B.

## North-South Calibration Problem

The calibration problem involves a small cross section with detailed information located between USW UZN-54 and USW UZN-55. The cross section is suitable for testing numerical methods and studying infiltration into the Topopah Spring welded unit. Seven simulations were conducted for the calibration problem.

The boundary conditions for the lateral boundaries are derived from the in-situ saturation measurements obtained from the bounding drill holes USW UZN-54 and USW UZN-55. The average moisture retention curve for the element (at a local scale) is used to back out a pressure and the median of the pressures for the element is used for the boundary condition. The top boundary is split into 15.24 meters width of alluvium in the arroyo and the rest as sideslope. The alluvium is given the same pressure as the top element adjacent to USW UZN-54 while the pressure from the top element bordering USW UZN-55 is taken to represent the sideslope. The bottom boundary is a linear interpolation of the pressures from the bottom corner elements. Note that two of the cross sections do not have an intact Topopah Spring caprock for which the bottom boundary condition is improbable.

The matrix saturations for the north-south cross section are shown in Figure 41. The welded material is 60% to 100% saturated while the nonwelded material is 33% to 66% saturated. A capillary barrier is evident above the nonwelded interval in all five simulations where the Topopah Spring caprock is intact. Simulation 5 of Figure 41, which has a thinning

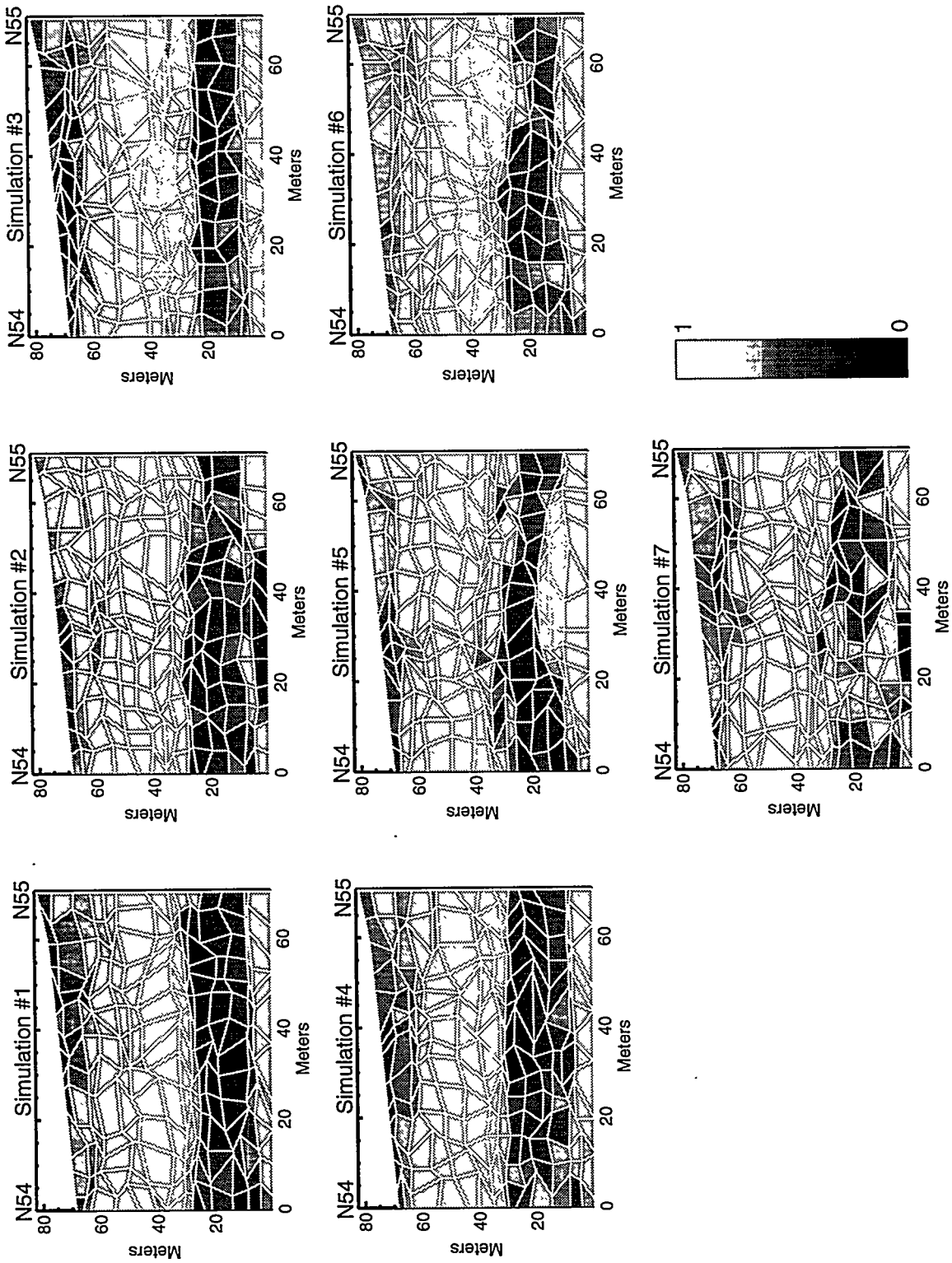


Figure 41. Matrix Saturations for the Calibration Problem

of the nonwelded interval, shows less of a capillary barrier but is approaching saturation just underneath the thinned out section.

The capillary pressures are shown in Figure 42. Simulations 3, 6 and 7 show elements as white where the pressure at the center of the element is above zero (saturated). Note that since the matrix saturation is averaged at the Gauss points the matrix saturation may not be 1.0. Locally saturated regions are where fracture flow may be initiated. If the highest pressure is above zero, it is shown in the legend. The value for simulation 3 appears rather high but the others look reasonable given the grid resolution. None of the simulations have a fracture saturation greater than about 75% (three of the four Gauss points saturated) and may or may not remain saturated as the grid is resolved.

The unsaturated conductivities are plotted in Figure 43. Darcy fluxes are shown in Figure 44. Simulations 2 and 7 where the Topopah Spring caprock is not intact show large velocities through the breaks due to the bottom boundary condition. The rest of the simulations show a few large fluxes near the lower left hand boundary probably reflecting the lateral boundary condition. Otherwise, the largest fluxes are in the nonwelded interval as expected. There does not appear to be any predominant flow direction which is not unexpected since the cross section is perpendicular to the dip. The Darcy fluxes in the Topopah Spring caprock, where it is intact, appear relatively uniform compared to the nonwelded interval.

## East-West INTRAVAL Problem

The INTRAVAL problem seeks to predict volumetric water content at USW UZ-16. The model used in this study is a two-dimensional east-west cross section. The western boundary is approximately at Ghost Dance Fault while the eastern boundary is near Bow Ridge Fault. The cross section intercepts the location of USW UZ-16. The top boundary is the topographical surface and the bottom is an elevation of 730.0 meters. In Nevada State Plane coordinates the cross section covers eastings 171,405.96 to 173,539.56 meters and a northing of 231,811.17 meters.

The lateral boundaries are faults and are handled as no-flow boundaries. The bottom boundary is taken as the water table with zero pressure. The topographical surface is split into three zones: alluvium, north and east facing slopes, and south and west facing slopes. The three zones are represented respectively by data from drill holes USW UZN-54, USW UZN-53, and USW UZN-55. Each of these drill holes have in-situ saturation and porosity data of which the uppermost measurements are used. Using the deterministic relationships

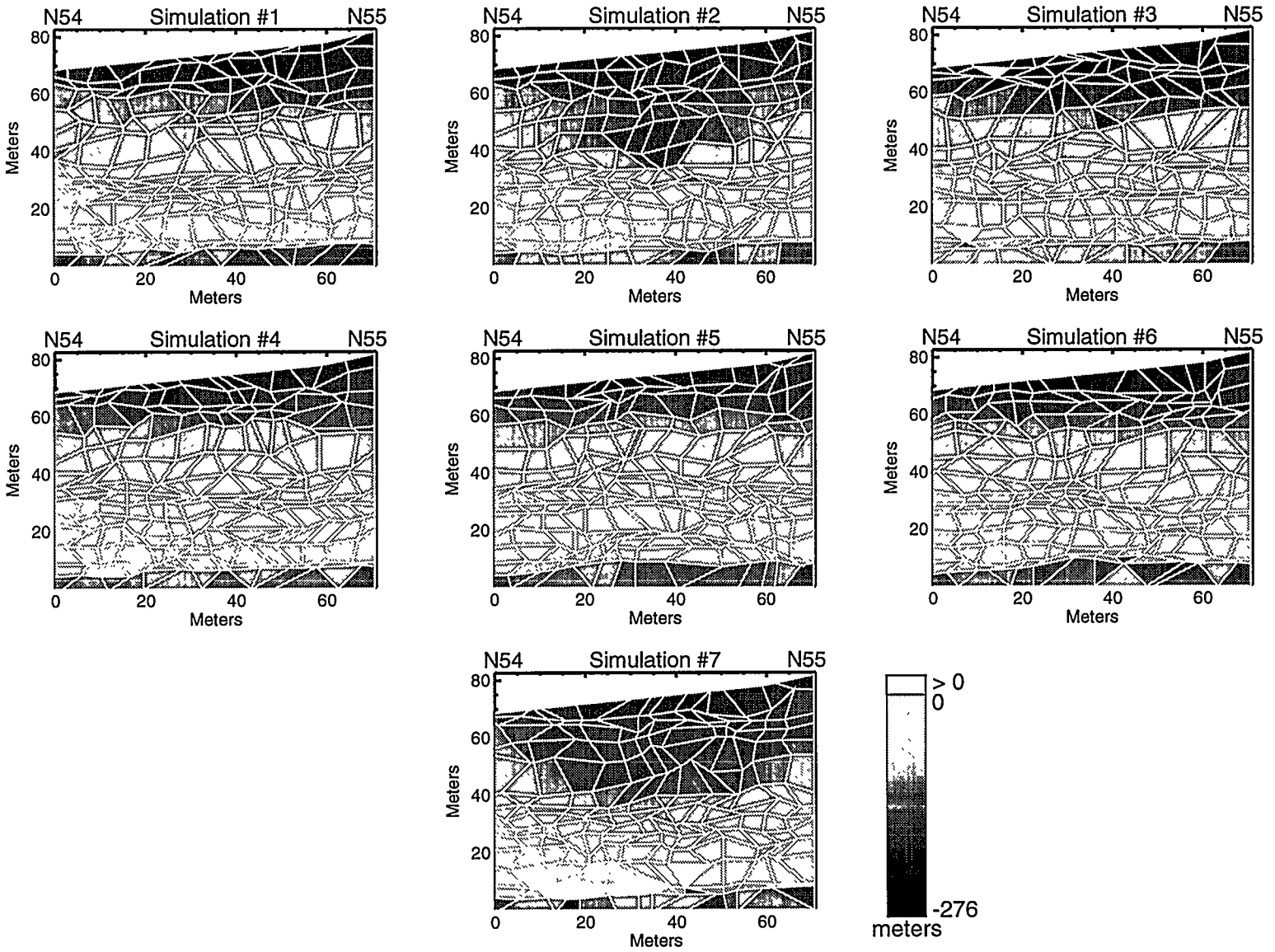


Figure 42. Capillary Pressures for the Calibration Problem

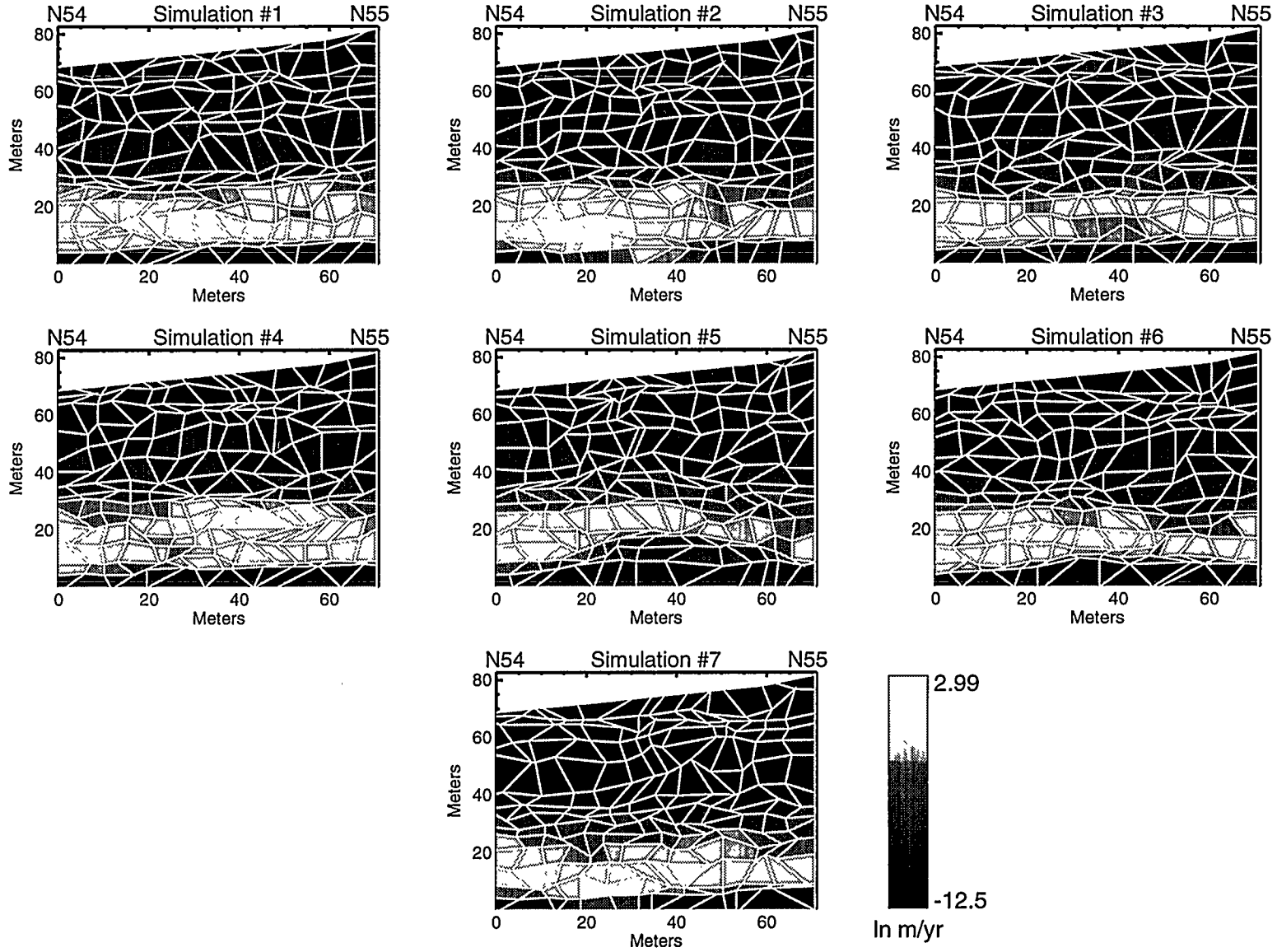


Figure 43. Conductivities for the Calibration Problem

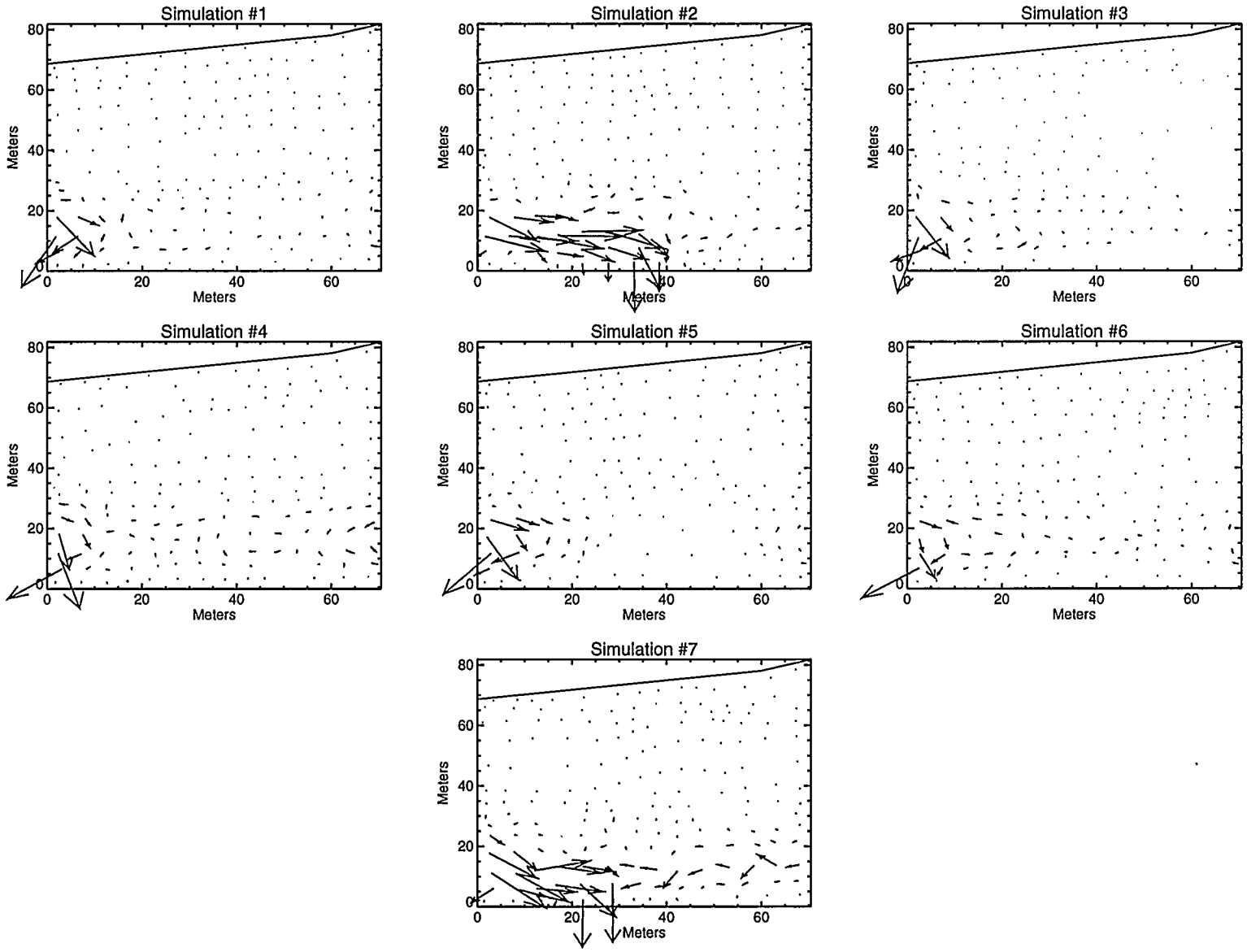


Figure 44. Darcy Fluxes for the Calibration Problem

for generating moisture retention curves, a pressure can be calculated for each of the three infiltration zones. From eastings 171,405.96 to 171,863.16 meters the top boundary is designated as shaded sideslope. Eastings 172,548.96 to 172,922.34 meters are taken to be sunny sideslope. The rest of the top boundary is classified as alluvium as shown in Figure 45. Pressure boundary conditions applied for each of the three infiltration zones are given in Table 5.

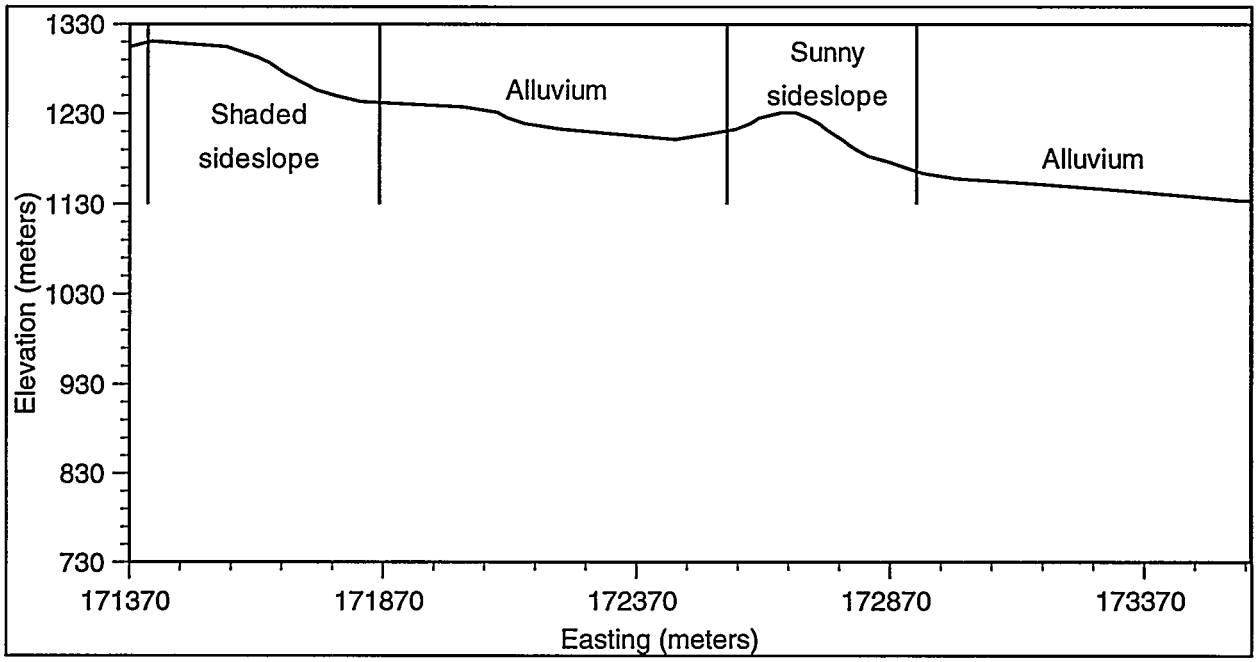

Figure 45. Infiltration Zones

Table 5: Infiltration Zones

| Zone | Drill Hole | Saturation (%) | Porosity | Pressure (meters) |
|---|---|---|---|---|
| shaded sideslope | USW UZN-53 | 85.0 | 0.068 | -77.9 |
| alluvium | USW UZN-54 | 69.0 | 0.09 | -114 |
| sunny sideslope | USW UZN-55 | 30.0 | 0.084 | -519 |

The predictions for volumetric water content at USW UZ-16 are shown for three realizations in Figure 46 along with the measured water contents. The computational results are good considering the coarse mesh used for the model. Plotting the saturations somewhat exaggerates the deficiencies in the model (Figure 47). The calculated volumetric water content of the Topopah vitric caprock is not well resolved and the calculated values for the

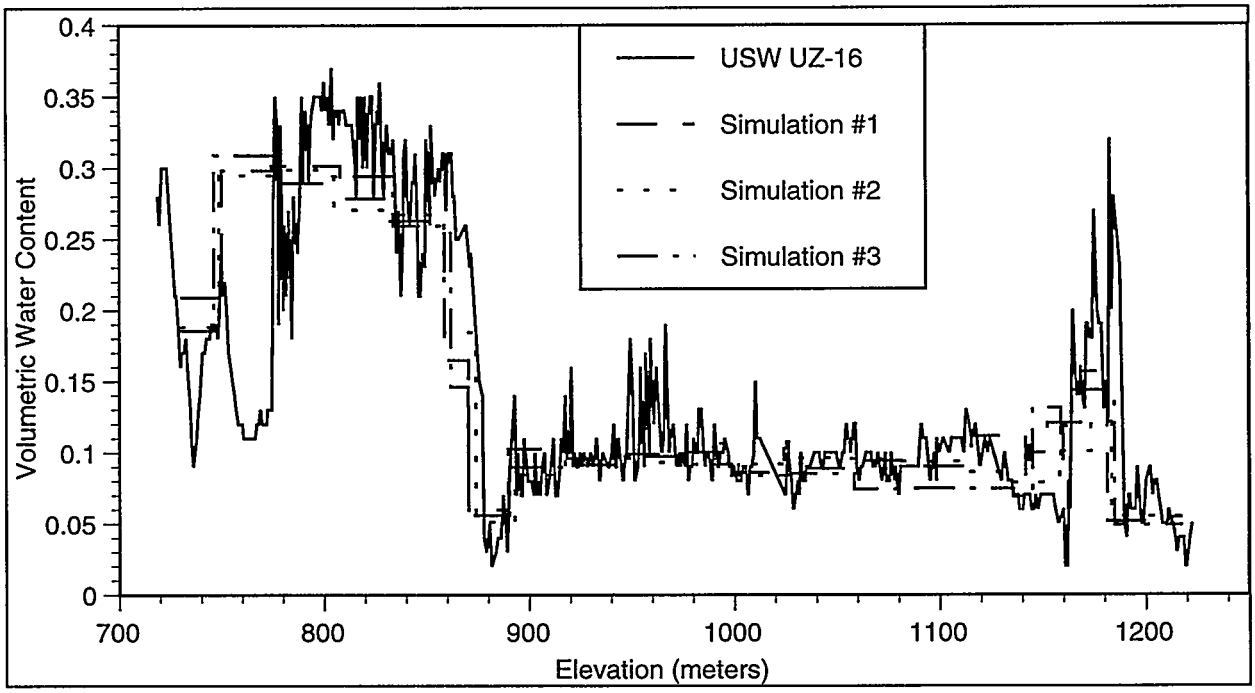

Figure 46. Volumetric Water Contents at USW UZ-16

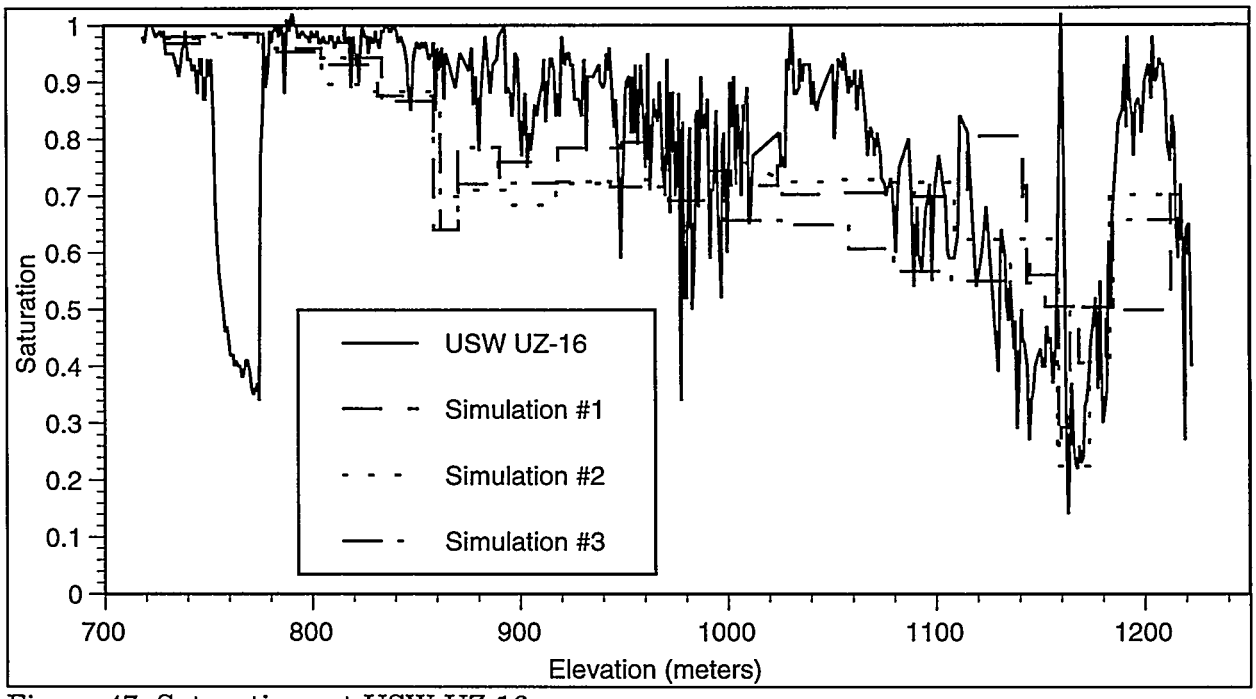

Figure 47. Saturations at USW UZ-16

region immediately below are not as dry as they should be. A finer geostatistical grid and flow grid may help but it may be difficult to resolve such thin features. In the lower part of the drill holes, the simulations do not follow the low volumetric water content in the nonwelded Prow Pass. It is apparent that lumping the nonwelded Prow Pass and Calico Hills

is the source of the problem. In view of these results, in future work the Prow Pass and Calico Hills should be modeled separately and the material properties developed separately. The spike at the Topopah vitric caprock is also not resolved as discussed earlier. The Topopah basal vitrophyre is not completely resolved, but is due to the coarse flow grid. The nonwelded Prow Pass can be seen to be quite different from the zeolitic Calico Hills unit.

The results of the flow simulation for the entire cross sections are shown in Figures 48 through 59. Note that average values for an element are plotted for each variable. The saturations in the Topopah Spring member generally reflect the infiltration zones (Figures 48 through 50). Each of the simulations have seven or eight elements with saturated fractures for at least one and as many as three of the four Gauss points. Refinement of the grid is necessary to determine if these are actually locally saturated zones. The pressures show the dry ridge as a result of the sunny sideslope boundary condition given in Table 5 (Figures 51 through 53). One element with a positive pressure appears in the first simulation; however, the entire element is not saturated (Figure 51). The elements below and to the left have much higher porosity, forming a capillary barrier. The element to the right has slightly higher porosity and average pore size. In addition, the element with positive pressure has a low matrix saturated conductivity compared to its neighbors. The plots of Darcy fluxes show considerable lateral flux in the nonwelded Paintbrush (Figures 54 through 56). The Darcy fluxes below the nonwelded Paintbrush are fairly vertical although the magnitudes vary depending on the saturation of the Topopah Spring member. Exfiltration can be noted where the sunny sideslope boundary is located around the central ridge. Unsaturated conductivity plots (Figures 57 through 59) show high conductivity in the nonwelded Paintbrush and low conductivities near the central ridge.

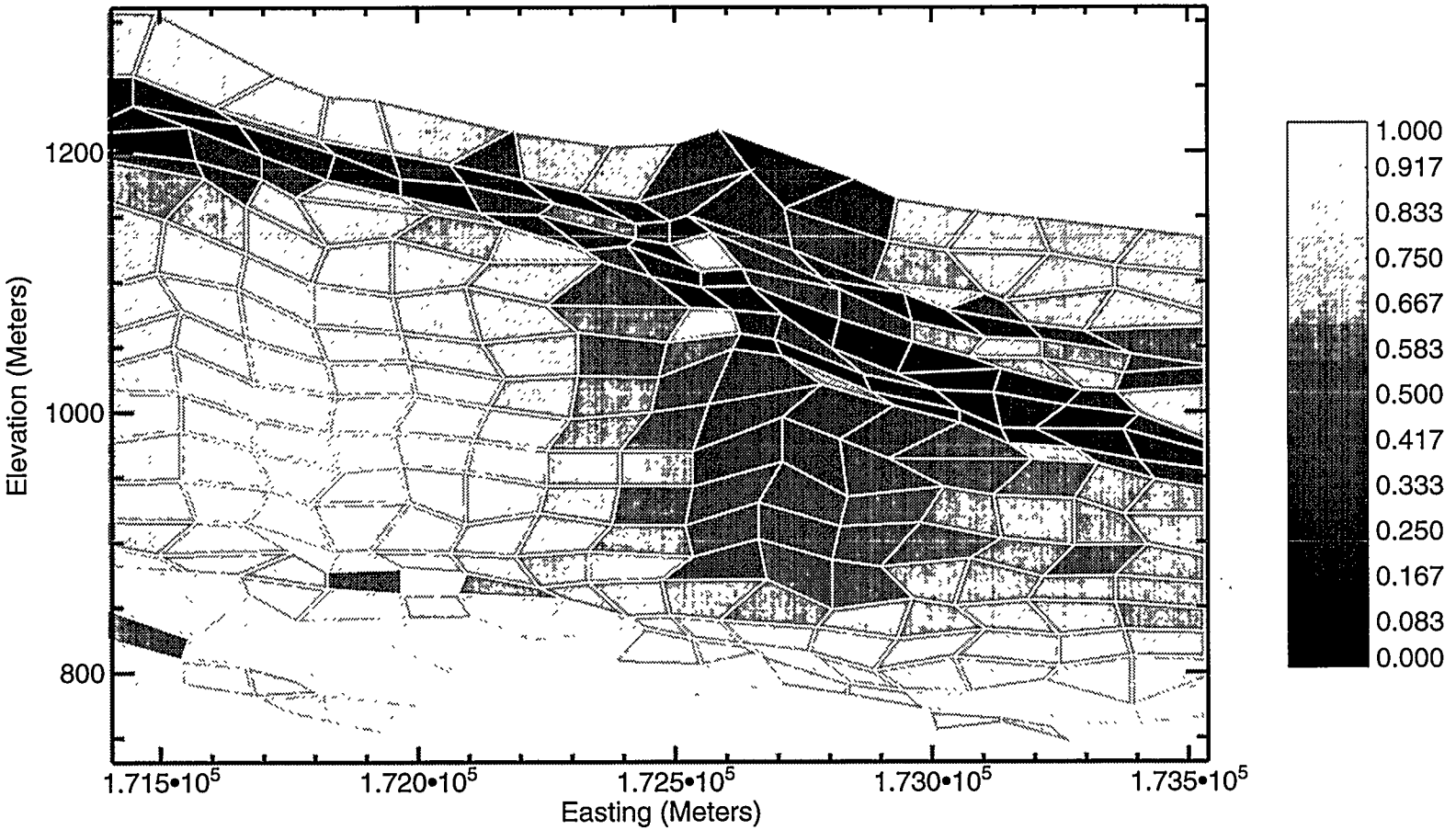


Figure 48. Matrix Saturations for the INTRAVAL Problem, Simulation #1

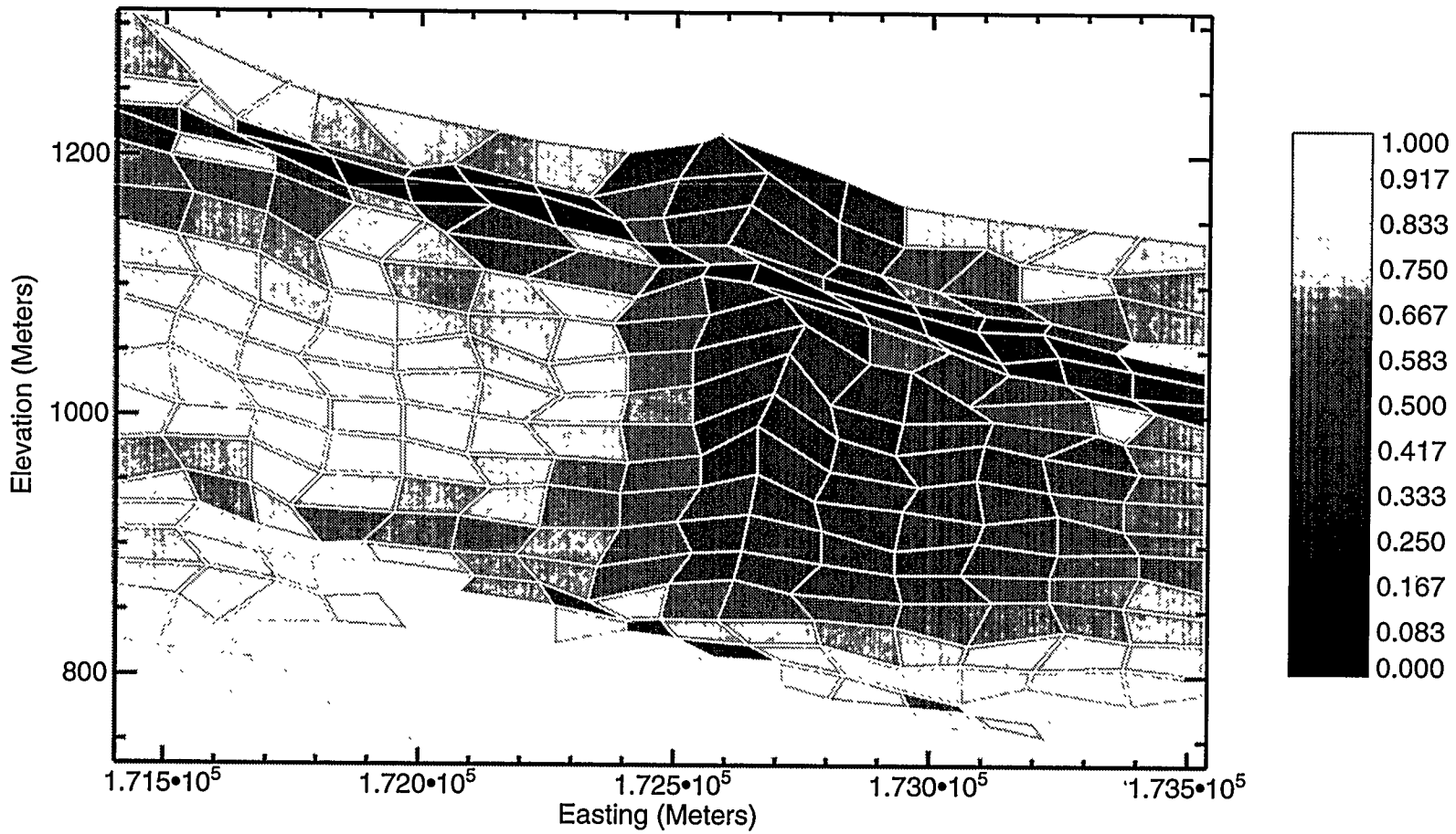


Figure 49. Matrix Saturations for the INTRAVAL Problem, Simulation #2

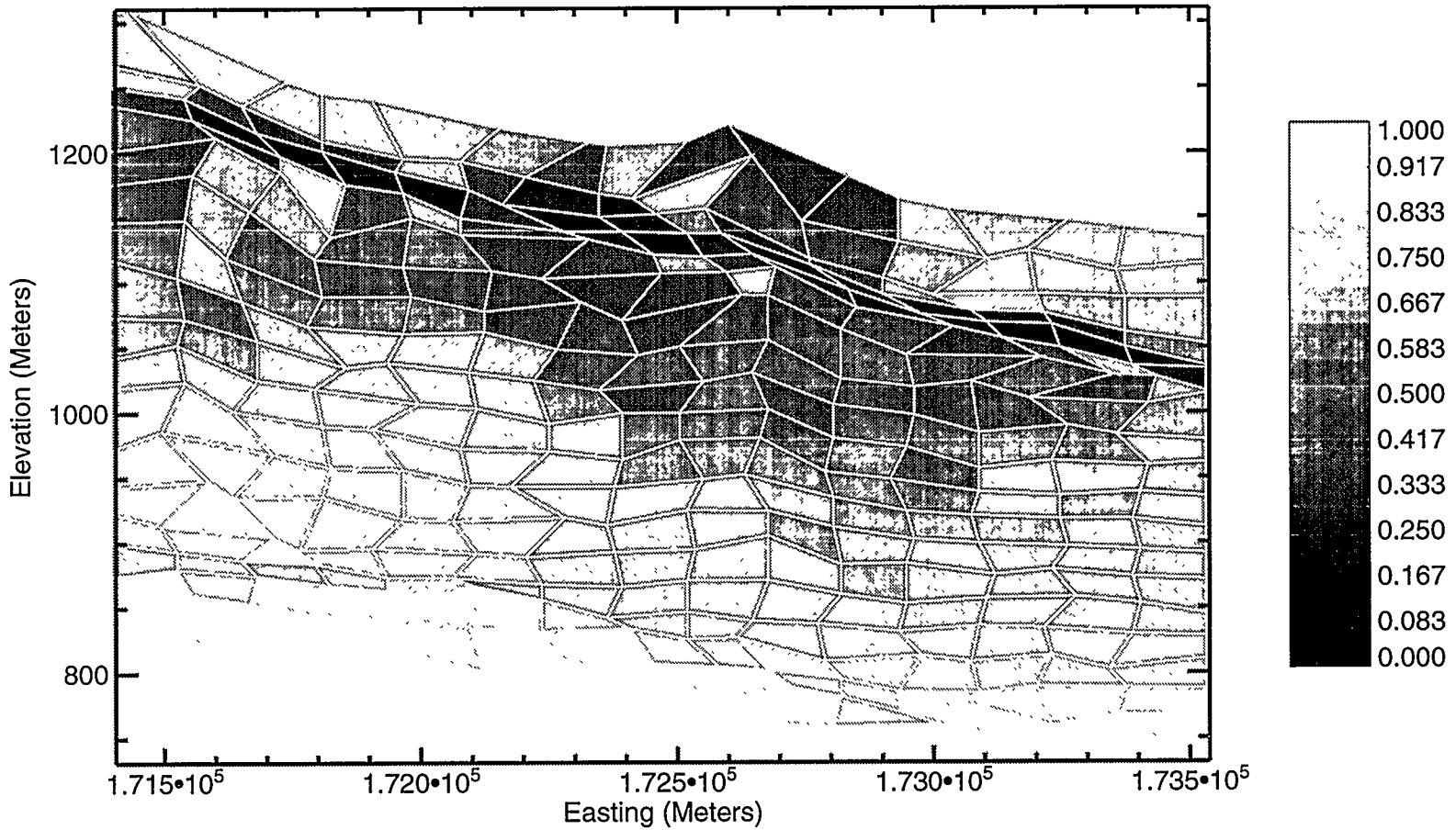


Figure 50. Matrix Saturations for the INTRAVAL Problem, Simulation #3

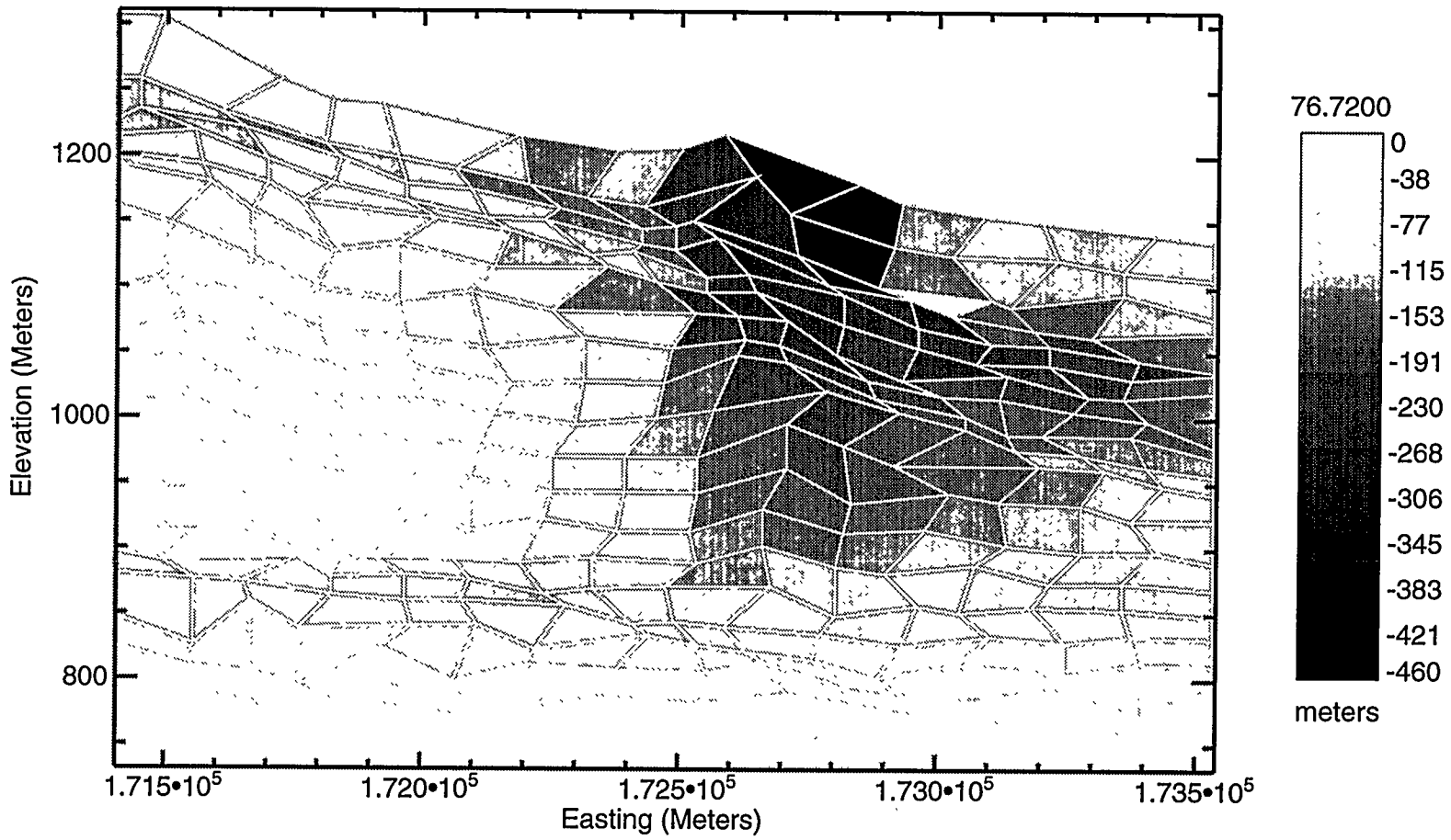


Figure 51. Capillary Pressures for the INTRAVAL Problem, Simulation #1

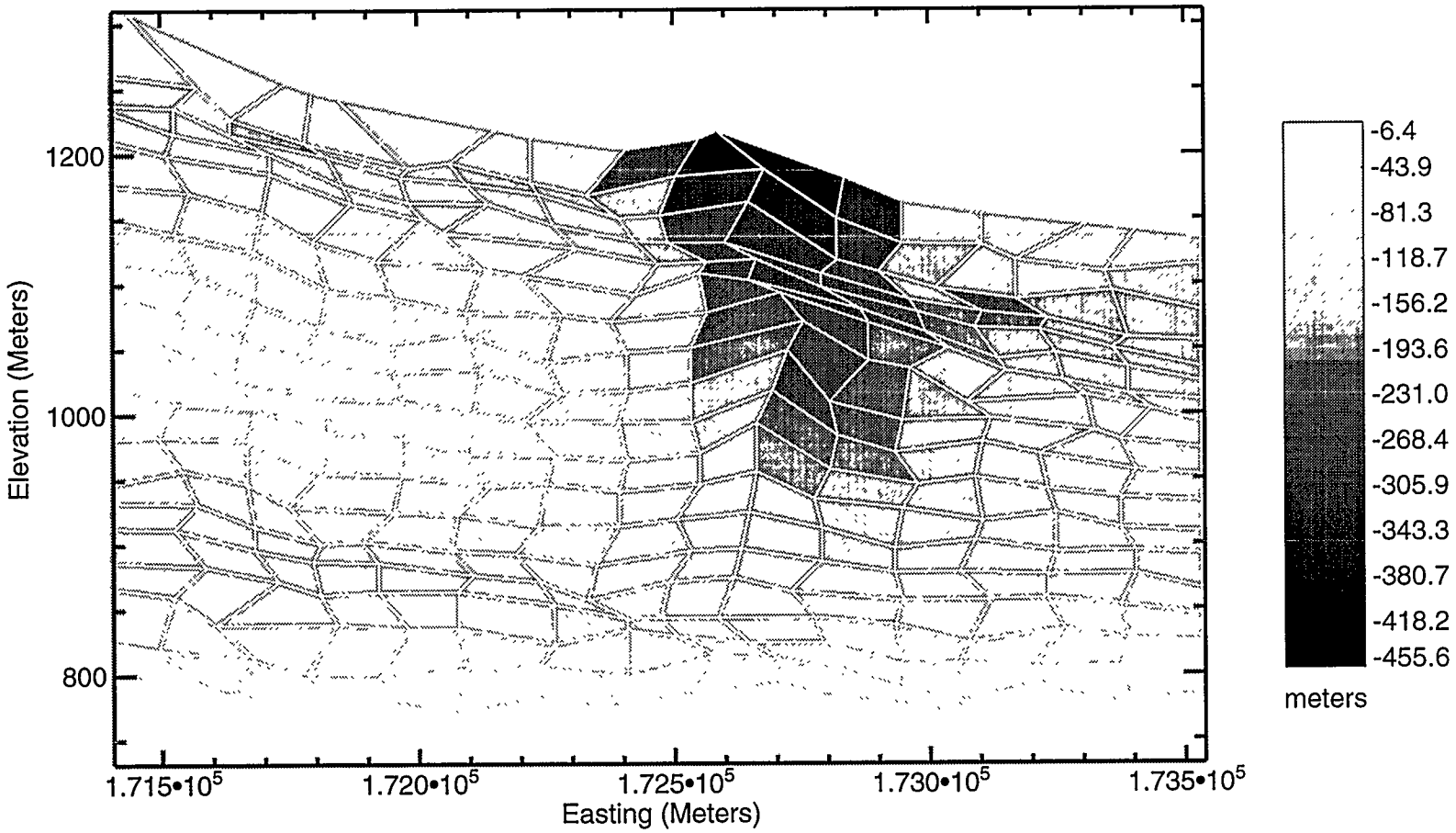


Figure 52. Capillary Pressures for the INTRAVAL Problem, Simulation #2

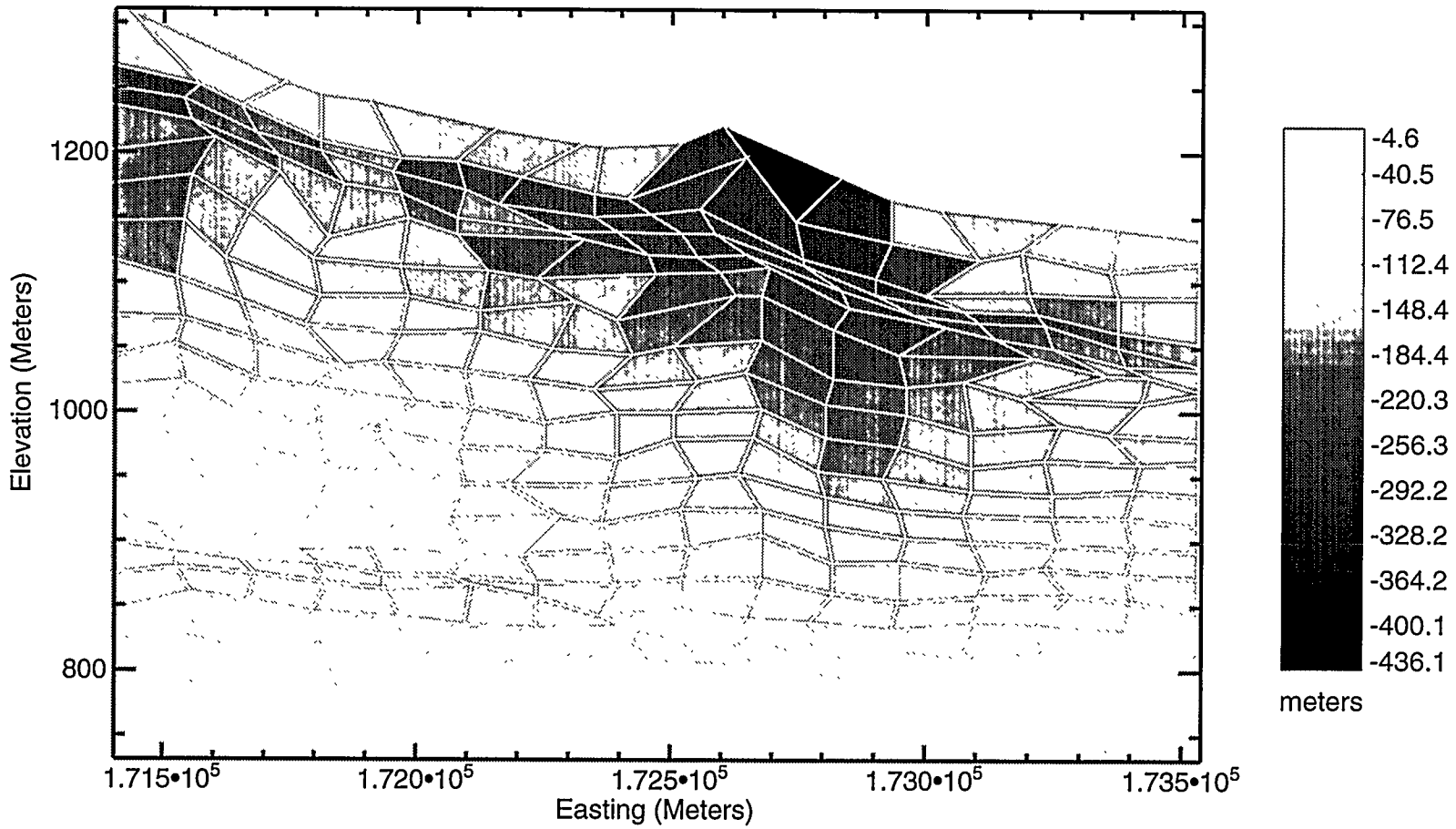


Figure 53. Capillary Pressures for the INTRAVAL Problem, Simulation #3

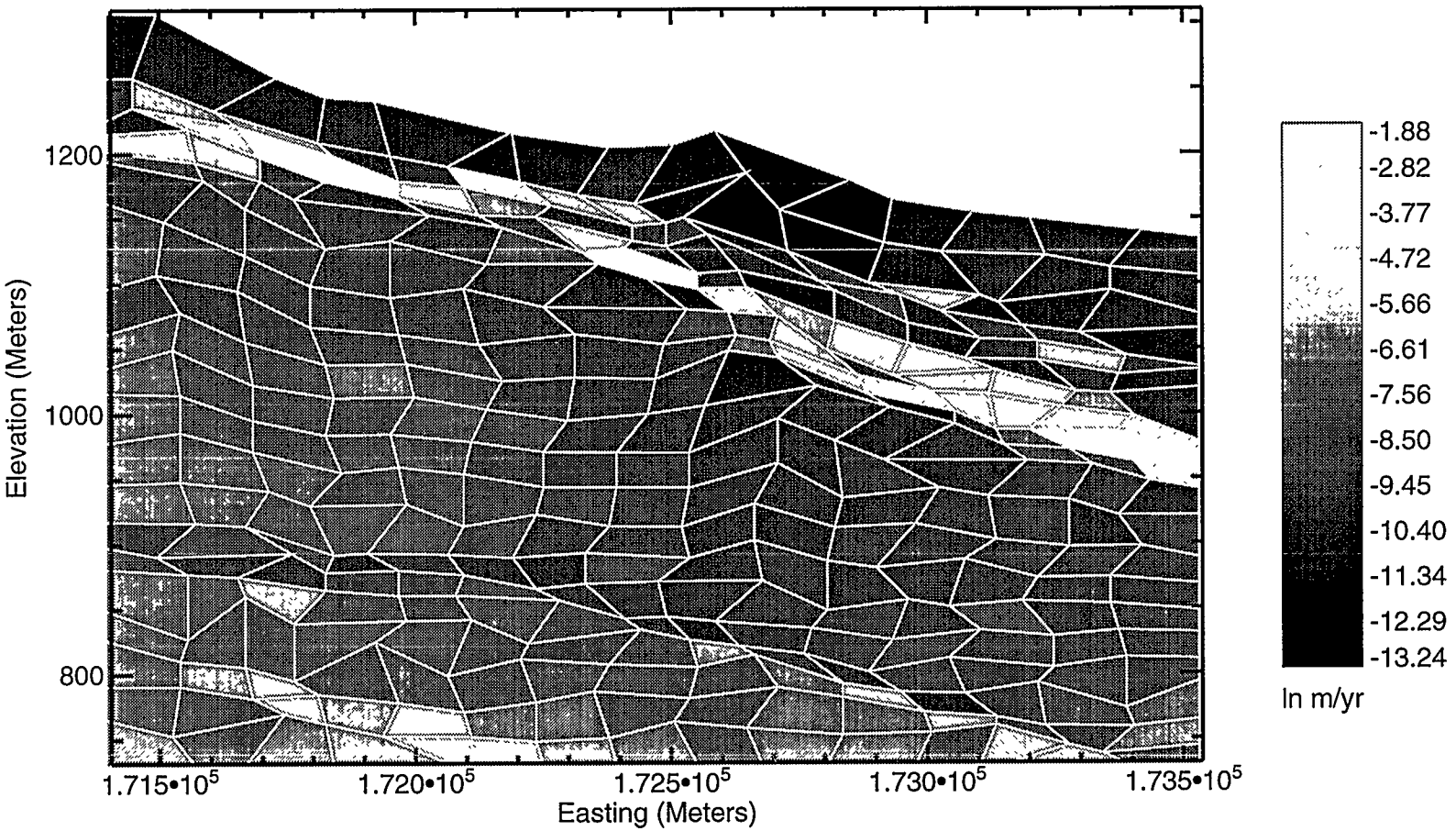


Figure 54. Conductivities for the INTRAVAL Problem, Simulation #1

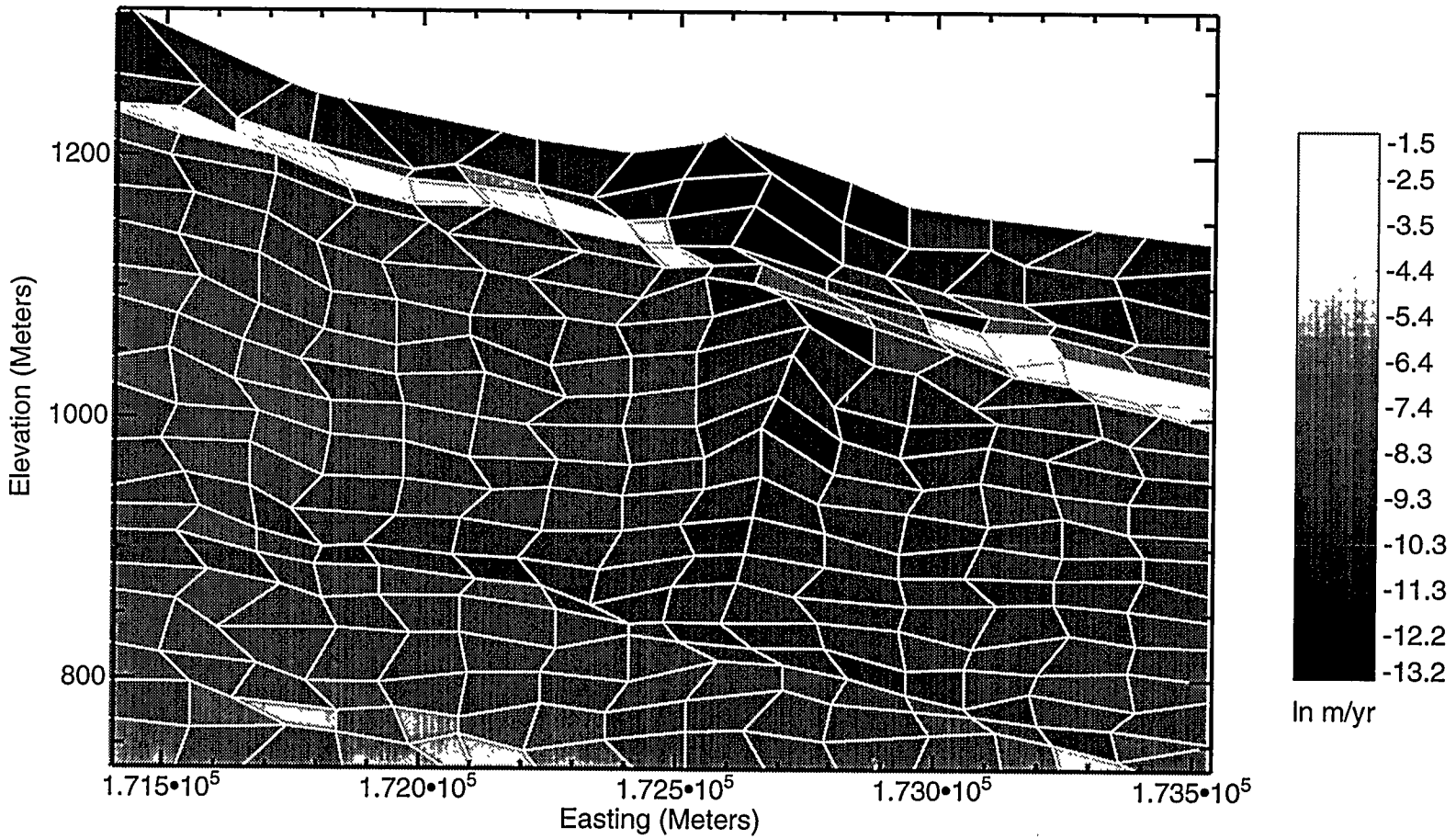


Figure 55. Conductivities for the INTRAVAL Problem, Simulation #2

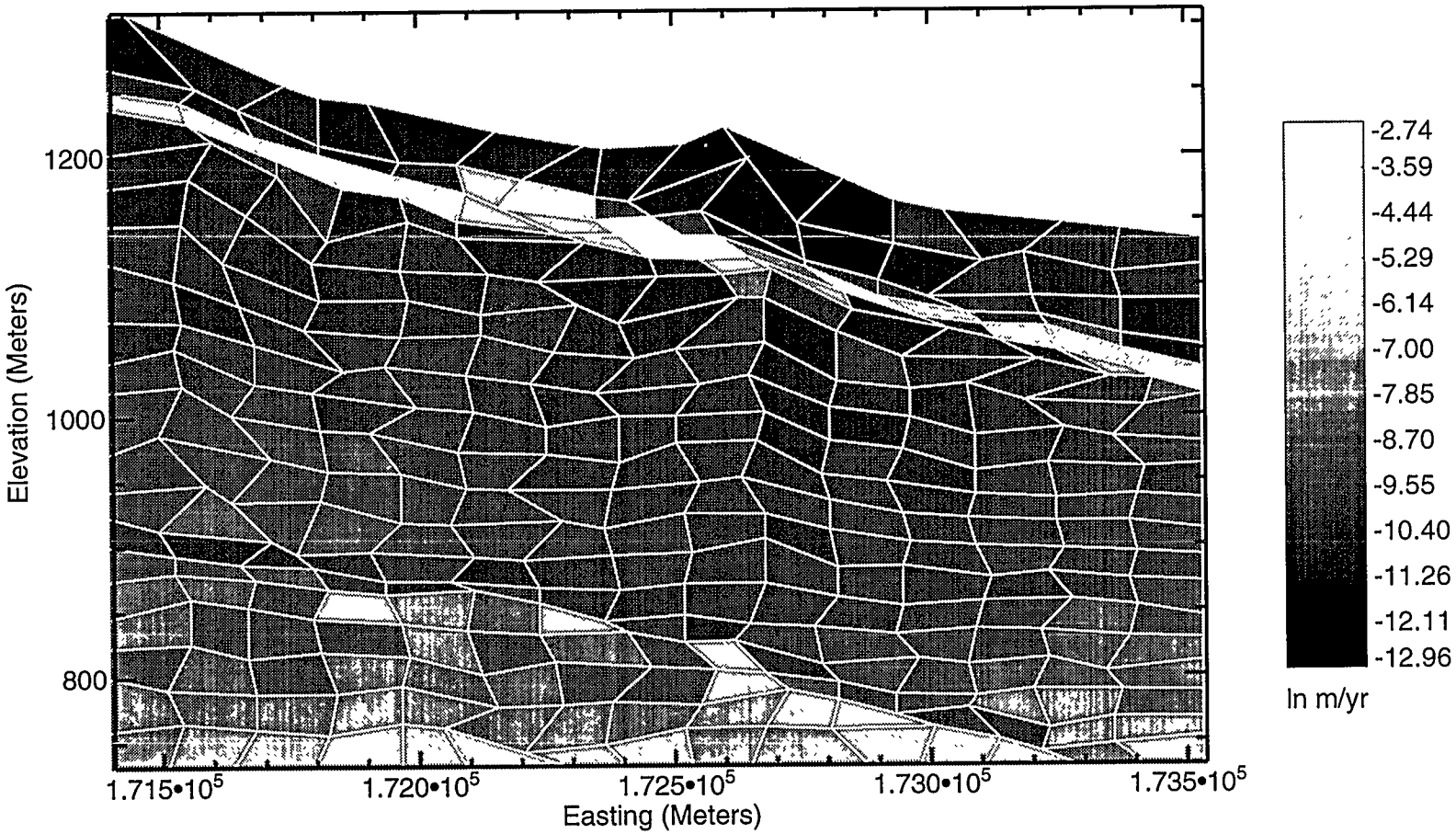


Figure 56. Conductivities for the INTRAVAL Problem, Simulation #3

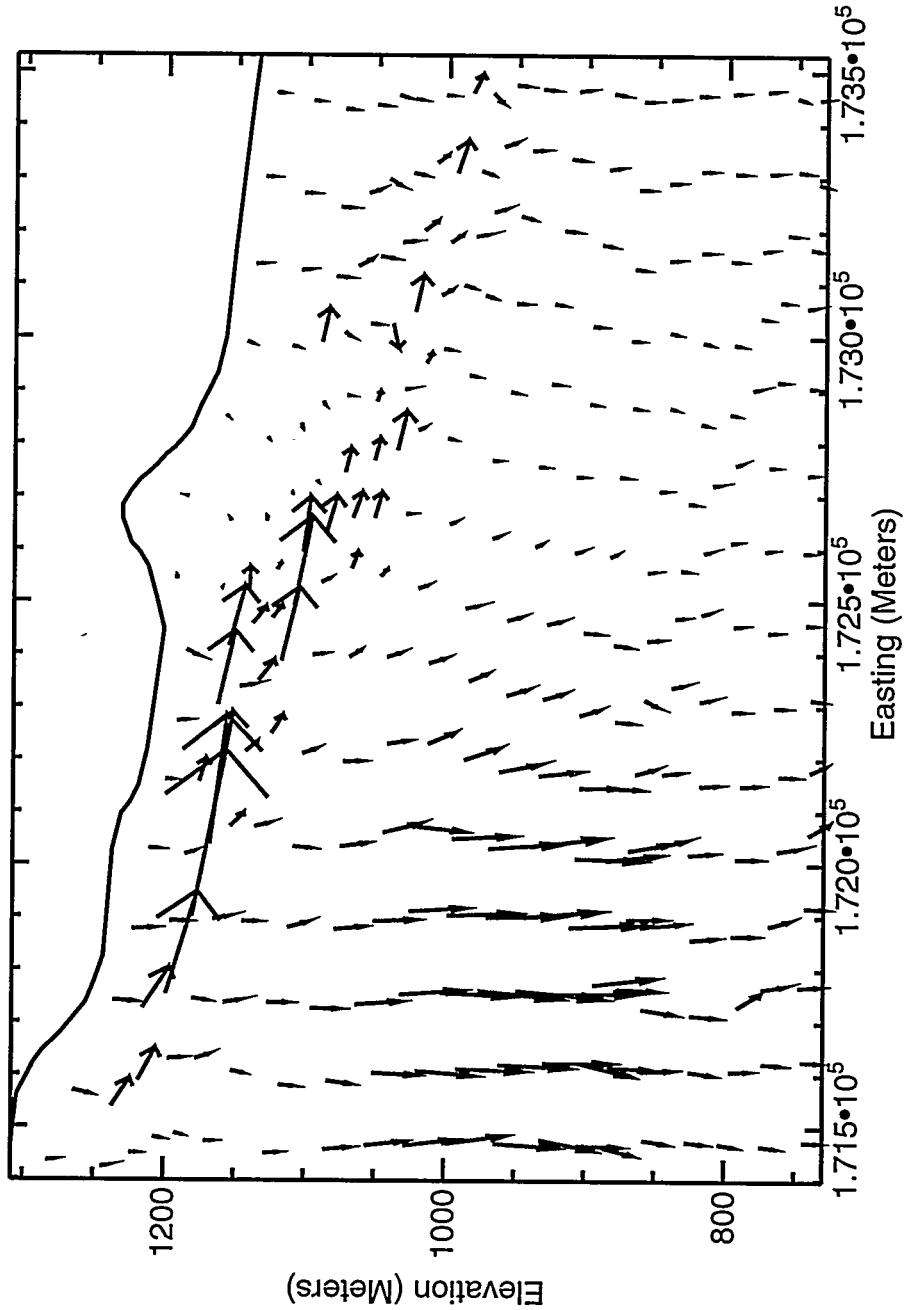


Figure 57. Darcy Fluxes for the INTRAVAL Problem, Simulation #1

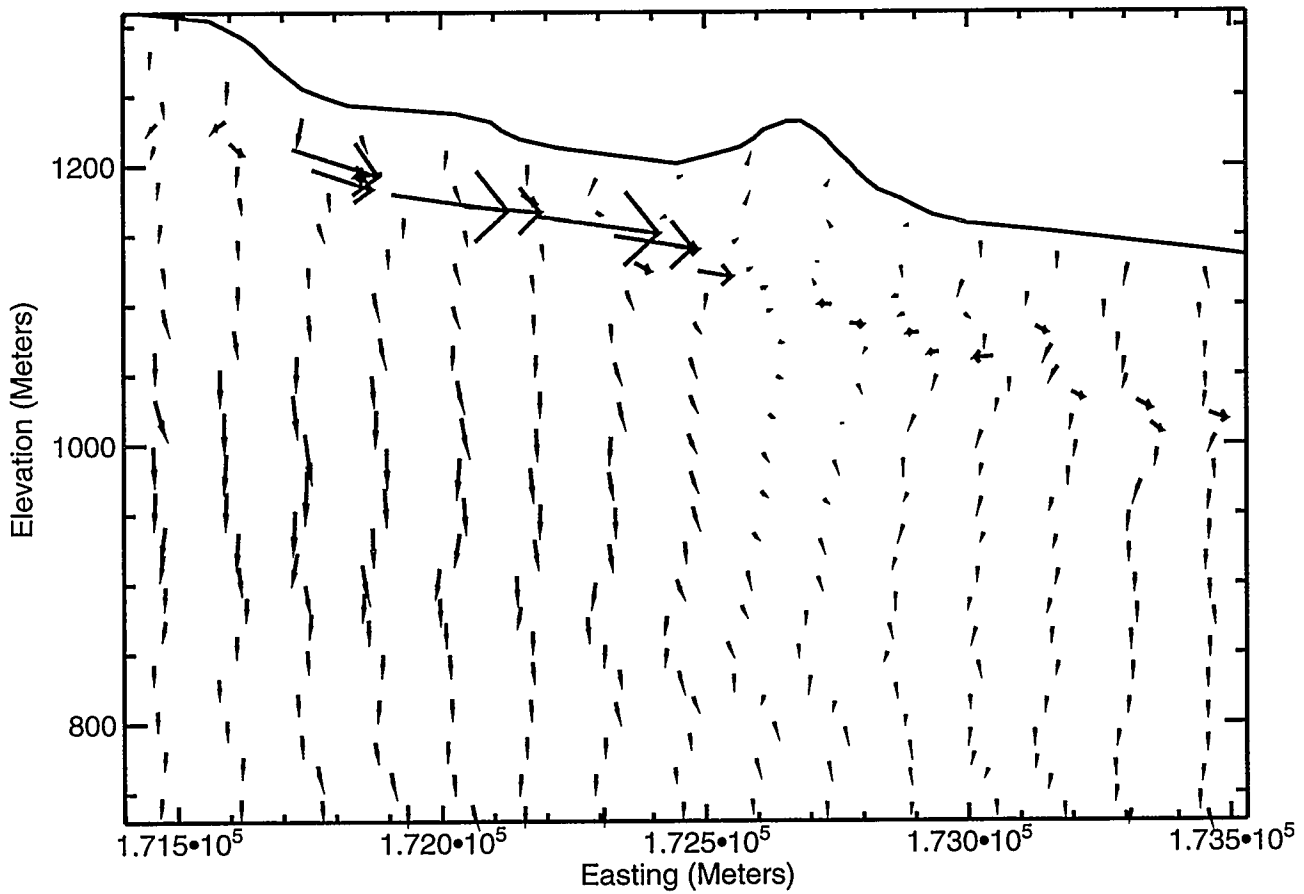


Figure 58. Darcy Fluxes for the INTRAVAL Problem, Simulation #2

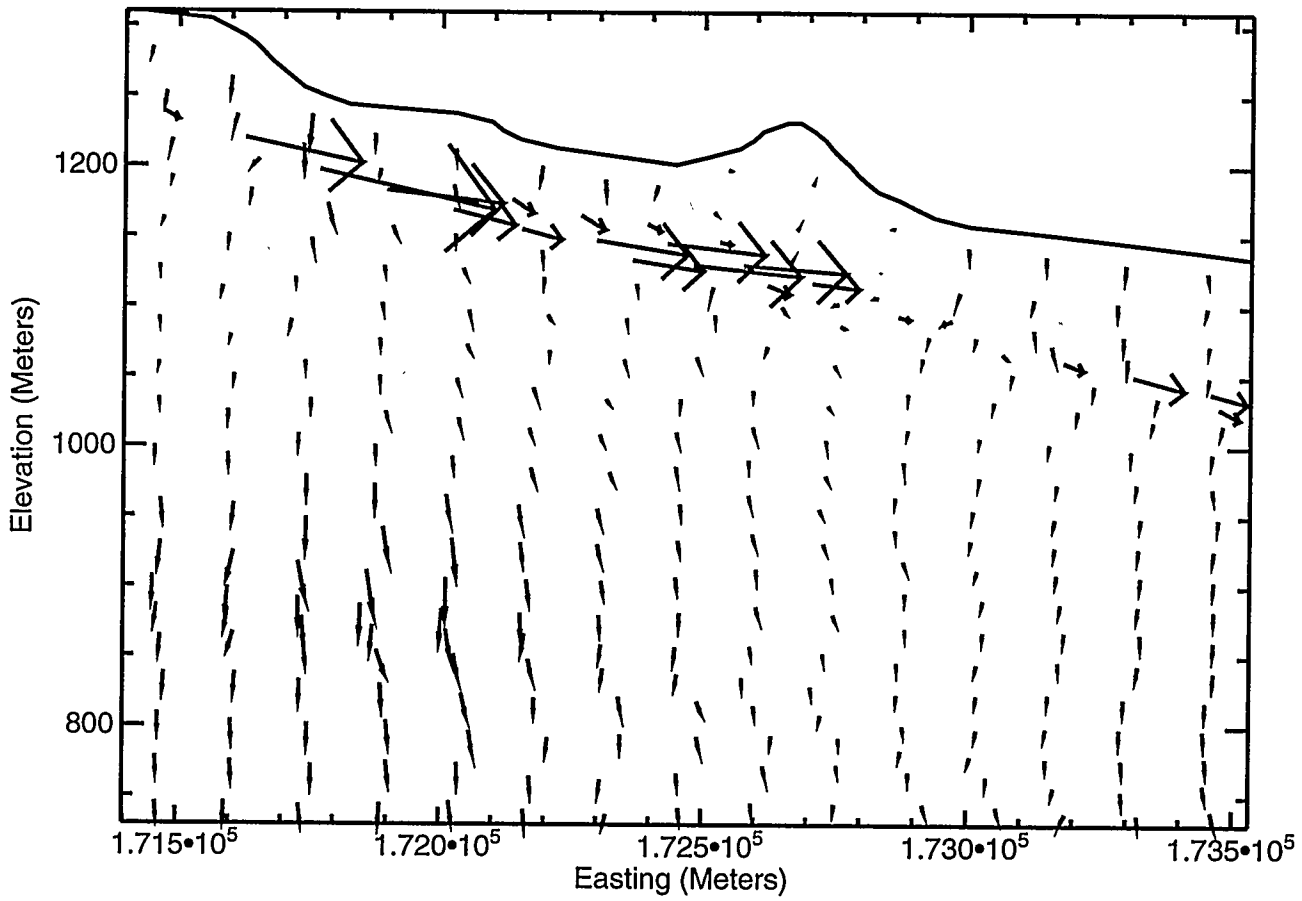


Figure 59. Darcy Fluxes for the INTRAVAL Problem, Simulation #3

# Conclusions

Compliance of a potential nuclear waste repository at Yucca Mountain with the ground water travel time criteria will be determined by the amount of radioactive material that can be transported along fast paths via fluid flow through fractured, porous media. Modeling fast paths requires an understanding of how fracture flow is initiated in unsaturated media. In this study, heterogeneity is investigated as a mechanism for creating locally saturated zones where fracture flow may be initiated. The ability to create regions of local saturation under natural or expected conditions rather than as arbitrary boundary conditions results in models that more closely resemble observations at Yucca Mountain. A reasonable attempt to model the unsaturated heterogeneous conditions at Yucca Mountain has been presented that combines geostatistical methods, upscaling of laboratory scale measurements, and advanced numerical flow modeling. For use in ground water travel time studies the model will require the development of a method for calculating travel times. Once travel times can be calculated these simulations will be suitable for use in more extensive testing of the numerical methods and evaluating the effects on the other parts of the simulations.

Two geostatistical methods, Gaussian simulation and indicator simulation, are used to generate models of heterogeneous media. While use of geostatistical methods for Yucca Mountain is quite challenging, the results are an improvement over homogeneous media used in virtually all previous modeling of Yucca Mountain since the simulations exhibit natural variations in surfaces between hydrogeologic units. Furthermore, a framework has been established to test for sensitivity of flow simulations (and eventually calculation of travel times) to different aspects of heterogeneity.

Use of the incomplete gamma function for the moisture retention curve is introduced. The gamma function then is theoretically representative of the pore size distribution through its relationship with the incomplete gamma function. Fitting the incomplete gamma function to the sparse data characteristic of laboratory data on porous rock is better posed than fitting the van Genuchten model.

The geostatistical adaptive grid procedure succeeds in producing flow grids that conform well to the features of the finer gesostatistical grid based on minimizing heterogeneity within each cell of the flow grid. Reductions in heterogeneity for the worst element averaged well over 50%, which should have an impact on errors in upscaling properties. Constraints on degenerate elements are incorporated into the adaptive grid algorithm.

There are two distinct upscalings considered in this report: from core scale to geostatistical scale and geostatistical scale to computational flow scale. Although the upscaling from core scale to geostatistical scale is minimized, laboratory measurements should be performed to verify whether any adjustments are required to the parameter distributions due to the change in scale. Theoretical formulas for upscaling from the geostatistical scale to computational flow scale have been introduced including simple methods for upscaling the incomplete gamma function. Since measurements of matrix properties at the computational scale are probably not practical, numerical studies should be conducted to verify the theoretical formulas presented. An adaptive grid technique has been introduced to minimize heterogeneity in elements and reduce potential upscaling errors which should minimize the number of numerical studies of upscaling required for verification.

A robust flow code has been assembled and applied to two-dimensional heterogeneous problems. The use of heterogeneous material and a flow code that does not suppress channeling results in locally saturated regions. The predictions of the volumetric water contents at USW UZ-16 match the in-situ measurements quite well except in the nonwelded part of the Prow Pass as discussed in the previous section on the results of the INTRAVAL problem.

There remain opportunities for improving the geostatistical techniques such as removing interfingering of geohydrological units in the indicator simulations. Knowledge regarding relatively constant thickness of hydrogeologic units across faults or fault zones is not incorporated into the geostatistics. Spatial correlations in porosities were not considered in this study due to the size of the flow elements but should be considered in future work especially if smaller flow elements are to be used. Better understanding and measurements of the heterogeneity (spatial continuity) are important to obtain more accurate models of the heterogeneity at Yucca Mountain.

Studies on additional constraints on distortion of the elements and the effects on flow modeling could provide useful information. Also, a grid resolution study is necessary both in terms of examining resolution of heterogeneity and convergence of the flow simulations. A finer geostatistical grid and flow grid may improve the flow models; however, even with fine grids it may be difficult to resolve thin features due to computational limitations. How the locally saturated regions react to grid resolution is an important area that needs to be examined.

In future work the Prow Pass and Calico Hills should be modeled separately and the material properties developed separately. Comparison of measured properties on different

scales at Yucca Mountain is necessary to validate the theoretical scaling formulas. There remains some work in improving the robustness of the flow code, especially in regards to longer execution times for a few of the simulations. Basic understanding of flow modeling has been emphasized in this study and there are many opportunities for increased speed and efficiency that remain.

Demonstrating the ability to produce locally saturated regions is an important step in moving water into fractures where transport can occur relatively quickly. However, the composite porosity model will quickly move the water back into the rock matrix as soon as the water leaves the locally saturated region. Dual permeability models will allow more of a delay in the water returning to the matrix. Maintaining fracture flow for a realistic time period is the next important step after the current investigation of initiation of fracture flow through locally saturated zones. A major difficulty for dual porosity models will be obtaining data that allows the coupling between the matrix and fractures to be adequately (realistically) modeled.

# Appendix A: Derivation of the DUAL Flow Code

Existence and uniqueness of a solution to the discretized equations is important to avoid numerical problems that can cause a code to fail. It is necessary to ensure that the nonlinear iterations are converging to something that is well defined, but it is also important that each nonlinear iteration is well posed to prevent failure of the code to produce a solution. Similiarly, it is important that as the discretization is made finer that the solutions converge to a well defined solution of the partial differential equations.

It is necessary to define the space of functions to which the solution belongs in order to consider the question of existence and uniqueness. The weak formulation of the differential equations used in finite elements can be expressed in terms of inner products. Existence and uniqueness require a complete inner product space which is called a Hilbert space (Oden, 1979).

The Hilbert spaces that shall be used are now introduced. Let $u = u(\mathbf{x})$ be an arbitrary function. Then

$$L^2(\Omega) \equiv \left\{ u : \int_\Omega u^2 \, d\Omega < \infty \right\}, \tag{A.1}$$

where the integration is in the Lebesgue sense. Associated with $L^2(\Omega)$ is the inner product

$$(u,p)_{L^2(\Omega)} \equiv \int_\Omega up \, d\Omega. \tag{A.2}$$

The corresponding norm is

$$\|u\|^2_{L^2(\Omega)} \equiv (u,u)_{L^2(\Omega)}. \tag{A.3}$$

The vector space $[L^2(\Omega)]^n$, where $n$ is the spatial dimension of the problem, is the vector analog of $L^2(\Omega)$. For $\mathbf{v}, \mathbf{q} \in [L^2(\Omega)]^n$ then

$$(\mathbf{v},\mathbf{q})_{[L^2(\Omega)]^n} \equiv \int_\Omega \mathbf{v} \cdot \mathbf{q} \, d\Omega, \tag{A.4}$$

is the inner product. The corresponding norm is

$$\|\mathbf{v}\|^2_{[L^2(\Omega)]^n} \equiv (\mathbf{v},\mathbf{v})_{[L^2(\Omega)]^n}. \tag{A.5}$$

It will also be necessary to consider spaces of functions that possess some degree of differentiability. The first Sobolev space is thus defined as

$$H^1(\Omega)\equiv\left\{u:\nabla u\in\left[L^2(\Omega)\right]^n\right\}. \tag{A.6}$$

The corresponding norm is

$$\|u\|^2_{H^1(\Omega)}\equiv\|u\|^2_{L^2(\Omega)}+\|\nabla u\|^2_{[L^2(\Omega)]^n}. \tag{A.7}$$

For vector functions, an appropriate space possessing a higher degree of differentiability is

$$H^{div}(\Omega)\equiv\left\{\mathbf{v}:\nabla\cdot\mathbf{v}\in L^2(\Omega)\right\}. \tag{A.8}$$

The corresponding norm is

$$\|\mathbf{v}\|^2_{H^{div}(\Omega)}\equiv\|\mathbf{v}\|^2_{[L^2(\Omega)]^n}+\|\nabla\cdot\mathbf{v}\|^2_{L^2(\Omega)}. \tag{A.9}$$

The mixed finite element method uses the variational (or weak) form of Equations (30)

$$\begin{aligned}\left([\rho k(\psi)]^{-1}(\rho\mathbf{q}),\mathbf{v}\right)_{[L^2(\Omega)]^n}+(\nabla(\psi+x_n),\mathbf{v})_{[L^2(\Omega)]^n}=0,\ \forall\mathbf{v}\in H^{div}(\Omega),\\ (\nabla\cdot(\rho\mathbf{q}),u)_{L^2(\Omega)}=0,\ \forall u\in L^2(\Omega),\end{aligned} \tag{A.10}$$

where $\mathbf{v}$ and $u$ are test functions. Green's formula is

$$(u,\nabla\cdot\mathbf{v})_{L^2(\Omega)}+(\nabla u,\mathbf{v})_{[L^2(\Omega)]^n}=(u,\mathbf{v}\cdot\mathbf{n})_{L^2(\Gamma)}, \tag{A.11}$$

which in this case is simply integration by parts. Substituting (A.11) into (A.10)

$$\begin{aligned}\left([\rho k(\psi)]^{-1}(\rho\mathbf{q}),\mathbf{v}\right)_{[L^2(\Omega)]^n}-\left(\psi+x_n,\nabla\cdot\mathbf{v}\right)_{L^2(\Omega)}=-\left(\psi_0+x_n,\mathbf{v}\cdot\mathbf{n}\right)_{L^2(\Gamma_d)},\ \forall\mathbf{v}\in H^{div}(\Omega),\\ -\left(\nabla\cdot(\rho\mathbf{q}),u\right)_{L^2(\Omega)}=0,\ \forall u\in L^2(\Omega),\end{aligned} \tag{A.12}$$

where $\rho\mathbf{q}\in H^{div}(\Omega)$ and $\psi+x_n\in L^2(\Omega)$ are the unknowns.

Theorem (Brezzi, 1974): Given Problem (A.12) with $\Gamma=\Gamma_d$ and $\psi_0+x_n\in L^2(\Omega)$ and the conditions

$$\rho(\psi)k(\psi)\text{ is bounded,} \tag{A.13}$$

$$\inf_{\substack{u\in L^2(\Omega)\\ u\neq 0}}\ \sup_{\substack{\mathbf{v}\in[L^2(\Omega)]^n\\ \mathbf{v}\neq\mathbf{0}}}\ \frac{(\nabla\cdot(\rho\mathbf{v}),u)_{L^2(\Omega)}}{\|u\|_{L^2(\Omega)}\|\mathbf{v}\|_{[L^2(\Omega)]^n}}\geq\beta>0, \tag{A.14}$$

then a unique, bounded solution exists. □

For Condition (A.13), $\rho$ is nearly constant and not of concern. $k(\psi)$ is easily shown to be bounded above by the maximum $k_s$. The problem lies in bounding $k(\psi)$ below. If there is no

residual saturation then $k(\psi)$ is not bounded below as $\psi \to -\infty$. However, since the differential equation is elliptic then for the Dirichlet problem the maximum (minimum) occurs on the boundary by the maximum principle. Thus $\psi$ and $k(\psi)$ are bounded as long as $\psi_0$ and $\psi_0+x_n$ are bounded. Condition (A.14) is the LBB condition (Ladyzhenskaya, 1969; Babuška, 1971; and Brezzi, 1974) and is of more concern after discretization. The discretization is achieved by defining projection operators in terms of the basis functions $\phi_i(\mathbf{x})$ and $\theta_i(\mathbf{x})$ and the scalars $q_i$, $v_i$, $p_i$, and $u_i$,

$$\begin{aligned}
\left(\rho q^{k}\right)_h &= \sum_{i=1}^{b} q_i \phi_i^k(\mathbf{x}), \quad k=1,\ldots,n, \\
\left(v^{k}\right)_h &= \sum_{i=1}^{b} v_i \phi_i^k(\mathbf{x}), \quad k=1,\ldots,n, \\
\left(\psi+x_n\right)_h &= \sum_{i=1}^{c} p_i \theta_i(\mathbf{x}), \\
u_h &= \sum_{i=1}^{c} u_i \theta_i(\mathbf{x}),
\end{aligned} \tag{A.15}$$

where $b$ is the dimension of the basis functions for flux and $c$ is the dimension of the basis functions for pressure. Substituting (A.15) into (A.12) and using

$$\begin{aligned}
B_{ij}^{k} &\equiv \left(\phi_i^k, \phi_j^k\right)_{L^2(\Omega)}, \quad k=1,\ldots,n, \\
D_{ij}^{k} &\equiv -\left(\theta_i, \frac{\partial \phi_j^k}{\partial x_k}\right)_{L^2(\Omega)}, \quad k=1,\ldots,n, \\
g_i &\equiv -\left(\psi_0+x_n, n_k \phi_i^k\right)_{L^2(\Gamma_d)}, \quad k=1,\ldots,n, \\
\mathbf{K} &\equiv diag\left[\rho k(\mathbf{p})\right]^{-1},
\end{aligned} \tag{A.16}$$

the following matrix equations are obtained

$$\begin{bmatrix} \mathbf{KB} & \mathbf{D}^T \\ \mathbf{D} & \mathbf{0} \end{bmatrix} \begin{bmatrix} \mathbf{q} \\ \mathbf{p} \end{bmatrix} = \begin{bmatrix} \mathbf{g} \\ \mathbf{0} \end{bmatrix}. \tag{A.17}$$

Corollary: Let $P_h \subset L^2(\Omega)$ and $Q_h \subset H^{div}(\Omega)$ be the spaces defined by the projection onto the basis functions. Given Problem (A.17) with $\Gamma = \Gamma_d$ and $\psi_0+x_n \in L^2(\Omega)$ and the conditions

$$\rho(\mathbf{p})k(\mathbf{p}) \text{ is bounded,} \tag{A.18}$$

$$P_h \subset \nabla \cdot Q_h, \tag{A.19}$$

then a unique solution exists. □

Proof: (Robey, 1990).

In addition there is a requirement for convergence as the mesh parameter h grows small which is beyond the scope of this work.

The flux boundary conditions are more difficult to incorporate than the pressure boundary condition. The normal fluxes at the boundary can be set to the desired value using Lagrange multipliers; however, then the pressure at the boundary cannot be specified. Currently, the pressure is not dealt with in the code. In special circumstances, a singular set of equations can result. The direct solver employed is capable of solving the system despite such a singularity (Robey, 1990).

An example of such a special circumstance is a two dimensional problem with a rectangular grid, constant pressure boundary conditions at the top and bottom, and identical constant flux boundary conditions on either side (one of those simple test problems). Consider, for simplicity, that the hydraulic conductivities are constant. For the lateral flow, then the lateral pressure drop is known and the coefficient of the $x$ term of the basis functions cannot be independently specified. No rank deficiency has been detected for any of the adapted grids employed so far.

It is convenient to work at the element level. Let $N_i$ be the basis functions for the hydraulic head and $\mathbf{B}_i$ the basis functions for the Darcy fluxes. The integration in Equation (A.16) is performed on a master element (see Figure 12) with local coordinates $\{\xi_i\}=\{\xi,\eta\}$. The element matrices are given by

$$\left(B_{ij}^{k}\right)^{e} = \int_e [\rho K(\mathbf{p})]^{-1} B_i^{k} B_j^{k} |\mathbf{J}| \, de, \; k=1,\ldots,n,$$

$$\left(D_{ij}^{k}\right)^{e} = -\int_e N_i \frac{\partial B_j^{k}}{\partial x_k} \, de, \; k=1,\ldots,n, \tag{A.20}$$

where $|\mathbf{J}|$ is the Jacobian of the transformation from physical space to the master element and where $\mathbf{D}^e$ is a matrix whose entries are $n$-dimensional vectors.

Choice of the basis functions $\mathbf{B}_i$ and $N_i$ determine the rate of convergence by which the discretization approaches the solution of the partial differential equations. Since using more

basis functions requires more work for each element, there is a trade-off of a coarser mesh with more basis functions or a finer mesh with fewer basis functions. Also, choice of the basis functions $\mathbf{B}_i$ and $N_i$ are not independent; Equation (A.19) must be satisfied. The optimum convergence rate is obtained where $P_h = \nabla \cdot Q_h$. The Raviart-Thomas basis functions (Raviart and Thomas, 1977) meet this condition; however, they are limited to rectangular grids which makes them unsuitable in this application. A finer mesh is more likely to be better than a theoretically high convergence rate since the error in computing an effective unsaturated conductivity, Equation (32), is probably a more important contributor to the error term. Equally important is that smaller elements reduce errors due to heterogeneity since all methods are first order if jumps in conductivity are located randomly relative to the grid (Das, *et al.*, 1993).

Two dimensional nodal basis functions for $\mathbf{B}_i$ that allow second order convergence are

$$\begin{aligned} B_1^k &= (1-\xi)(1-\eta)/4, \\ B_2^k &= (1+\xi)(1-\eta)/4, \\ B_3^k &= (1+\xi)(1+\eta)/4, \\ B_4^k &= (1-\xi)(1+\eta)/4. \end{aligned} \tag{A.21}$$

For the bilinear basis functions given by Equation (A.21), the Jacobian of the transformation is given by Equations (3) and (4). The basis functions for $N_i$ that allow second order convergence are

$$\begin{aligned} N_1 &= 1, \\ N_2 &= \xi, \\ N_3 &= \eta. \end{aligned} \tag{A.22}$$

Then the integrations result in

$$(\mathbf{D}^e)^T=\begin{bmatrix}(\mathbf{D}^1)^T\\(\mathbf{D}^2)^T\end{bmatrix}^T=\begin{bmatrix}\frac{y_4-y_2}{2} & \frac{y_3-y_4}{6} & \frac{y_2-y_3}{6}\\ \frac{y_1-y_3}{2} & \frac{y_4-y_3}{6} & \frac{y_4-y_1}{6}\\ \frac{y_2-y_4}{2} & \frac{y_2-y_1}{6} & \frac{y_1-y_4}{6}\\ \frac{y_3-y_1}{2} & \frac{y_1-y_2}{6} & \frac{y_3-y_2}{6}\\ \frac{x_2-x_4}{2} & \frac{x_4-x_3}{6} & \frac{x_3-x_2}{6}\\ \frac{x_3-x_1}{2} & \frac{x_3-x_4}{6} & \frac{x_1-x_4}{6}\\ \frac{x_4-x_2}{2} & \frac{x_1-x_2}{6} & \frac{x_4-x_1}{6}\\ \frac{x_1-x_3}{2} & \frac{x_2-x_1}{6} & \frac{x_2-x_3}{6}\end{bmatrix}. \tag{A.23}$$

$\mathbf{B}^e$ can be evaluated using Gaussian quadrature or, by assuming an effective conductivity exists, using analytical integration. In the absence of a clear difference, analytical integration is used since there are advantages when used with the current solver. The $\mathbf{B}^e$ matrix is

$$(\mathbf{B}^k)^e=\frac{1}{9}\begin{bmatrix}4j_0-2j_1-2j_2 & 2j_0-j_2 & j_0 & 2j_0-j_1\\ 2j_0-j_2 & 4j_0+2j_1-2j_2 & 2j_o+j_1 & j_0\\ j_0 & 2j_0+j_1 & 4j_0+2j_1+2j_2 & 2j_0+j_2\\ 2j_0-j_1 & j_0 & 2j_0+j_2 & 4j_0-2j_1+2j_2\end{bmatrix}, \tag{A.24}$$

where $j_0, j_1$, and $j_2$ are defined in Equation (4).

The global matrices are obtained by assembling the element matrices (and thus implicitly defining $\phi$ and $\theta$ of Equations (A.15)). Equation (A.12) requires that $\rho\mathbf{q}$ be in $H^{div}(\Omega)$ or

$$\nabla\cdot(\rho\mathbf{q})\in L^2(\Omega). \tag{A.25}$$

Note that functions in $H^{div}(\Omega)$ are not as smooth as those in $[H^1(\Omega)]^n$ since the sum of partial derivatives must be in $L^2(\Omega)$ rather than each partial derivative belonging to $L^2(\Omega)$. Since the projection onto the element is the space of polynomials which is infinitely differentiable, the

lack of smoothness must occur at the element boundaries. Let $\mathbf{q}_1 \in H^{div}(\Omega)$ be possibly discontinuous across an arbitrary element boundary. Then

$$q_1 = \begin{cases} q_1^1, & \mathbf{x} \in \Omega_1^e, \\ q_1^2, & \mathbf{x} \in \Omega_2^e, \end{cases} \tag{A.26}$$

where the superscript refers to the element. In the distributional sense, the partial derivative in two dimensions is

$$\frac{\partial q_1}{\partial x_1} = \begin{cases} \dfrac{\partial q_1^1}{\partial \xi}\dfrac{\partial \xi}{\partial x_1} + \dfrac{\partial q_1^1}{\partial \eta}\dfrac{\partial \eta}{\partial x_1}, & \mathbf{x} \in \Omega_1^e, \\ \dfrac{\partial q_1^2}{\partial \xi}\dfrac{\partial \xi}{\partial x_1} + \dfrac{\partial q_1^2}{\partial \eta}\dfrac{\partial \eta}{\partial x_1}, & \mathbf{x} \in \Omega_2^e, \\ \delta(q_1^2 - q_1^1) n_1^2, & \mathbf{x} \in \Gamma_{12}^e, \end{cases} \tag{A.27}$$

where $n_1^i$ is the first component of the normal to the ith element boundary. A similar equation applies to the other component of $\mathbf{q}$. For Equation (A.25) to be satisfied then the following condition must be true

$$\delta\left(q_1^2 - q_1^1\right) n_1^2 + \delta\left(q_2^2 - q_2^1\right) n_2^2 = 0. \tag{A.28}$$

This condition is simply continuity of normal flux across the element boundary.

There are several ways to set up the matrix equations with different solvers applicable. One approach is to solve the first equation of Equation (A.17) for $\mathbf{q}$ and substitute into the second equation to obtain

$$\mathbf{D}(\mathbf{KB})^{-1}\mathbf{D}^T\mathbf{p} = \mathbf{D}(\mathbf{KB})^{-1}\mathbf{g}. \tag{A.29}$$

The matrix on the left hand side is symmetric and typically positive definite which allows many linear solvers and preconditioners to be applied. However, the Jacobian may not be easy to compute and it may be more difficult to take advantage of structure. Instead, DUAL uses a variant of Equation (A.17) called the *mixed hybrid method* (Fraeijs de Veubeke, 1965) where the assembly constraint for the Darcy flux is replaced with Lagrange multipliers. This formulation results in a block diagonal $\mathbf{B}$ which can be factored element-by-element, a fact that is used by the direct solver. The resulting equations are

$$\begin{bmatrix} \mathbf{KB} & \mathbf{D}^T & \mathbf{C}^T \\ \mathbf{D} & \mathbf{0} & \mathbf{0} \\ \mathbf{C} & \mathbf{0} & \mathbf{0} \end{bmatrix} \begin{bmatrix} \mathbf{q} \\ \mathbf{p} \\ \lambda \end{bmatrix} = \begin{bmatrix} \mathbf{g} \\ \mathbf{0} \\ \mathbf{f} \end{bmatrix}, \tag{A.30}$$

where **f** is due to flux boundary conditions. The matrix **C** is sparse, with entries consisting of the components of the normal vectors of Equation (A.28).

# Appendix B: Direct Null Space Solver

The direct solver used is a null space method (Heath, 1976 and Robey, 1992). First the equations are reformulated. Since **B** is block diagonal the Cholesky decomposition $\mathbf{B} = \mathbf{L}\mathbf{L}^T$ can be computed efficiently element by element. Since **K** is a diagonal matrix, then the first row can be multiplied by $\mathbf{L}^{-1}$ to obtain

$$\begin{bmatrix} \mathbf{K} & \mathbf{L}^{-1}\mathbf{D}^T & \mathbf{L}^{-1}\mathbf{C}^T \\ \mathbf{D}\mathbf{L}^{-T} & \mathbf{0} & \mathbf{0} \\ \mathbf{C}\mathbf{L}^{-T} & \mathbf{0} & \mathbf{0} \end{bmatrix} \begin{bmatrix} \mathbf{L}^T\mathbf{q} \\ \mathbf{p} \\ \lambda \end{bmatrix} = \begin{bmatrix} \mathbf{L}^{-1}\mathbf{g} \\ \mathbf{0} \\ \mathbf{f} \end{bmatrix}. \tag{B.1}$$

Define the matrices

$$\begin{aligned} \mathbf{A} &\equiv \begin{bmatrix} \mathbf{L}^{-1}\mathbf{D}^T & \mathbf{L}^{-1}\mathbf{C}^T \end{bmatrix}, \\ \mathbf{s} &\equiv \mathbf{L}^T\mathbf{q}, \\ \mathbf{g} &\equiv \mathbf{L}^{-1}\mathbf{g}, \\ \mathbf{t} &\equiv \begin{bmatrix} \mathbf{p} \\ \lambda \end{bmatrix}, \\ \mathbf{f} &\equiv \begin{bmatrix} \mathbf{0} \\ \mathbf{f} \end{bmatrix}. \end{aligned} \tag{B.2}$$

Then the matrix equations can be expressed

$$\begin{bmatrix} \mathbf{K} & \mathbf{A} \\ \mathbf{A}^T & \mathbf{0} \end{bmatrix} \begin{bmatrix} \mathbf{s} \\ \mathbf{t} \end{bmatrix} = \begin{bmatrix} \mathbf{g} \\ \mathbf{f} \end{bmatrix}. \tag{B.3}$$

The matrix **A** is, in general, a rectangular *mxp* matrix with *m* greater than or equal to *p*. The rank of **A** is $r \le p$. A sparse QR decomposition (Golub and Van Loan, 1983) of **A** requires both row and column pivoting

$$\mathbf{P}(\mathbf{Q}^T\mathbf{K}^{-1/2}\mathbf{A})\Pi = \begin{bmatrix} \mathbf{R} & \mathbf{M} \\ \mathbf{0} & \mathbf{0} \end{bmatrix}, \tag{B.4}$$

where **R** is an *rxr* upper triangular matrix and **M** has columns linearly dependent on the

columns of **R**. **P** and Π are permutation matrices that represent row and column pivoting. Partitioning of $\mathbf{QP}^T = [\,\mathbf{Y}\ \mathbf{Z}\,]$ results in

$$\mathbf{K}^{-1/2}\mathbf{A}\Pi=\mathbf{Y}[\mathbf{R}\ \ \mathbf{M}]. \tag{B.5}$$

**Y** has $r$ columns which form a basis for the range space of **A**. **Z** is $m$x($m$-$r$) and the columns of **Z** form a basis for the null space of $\mathbf{A}^T$.

Since the columns of **Y** and **Z** form a basis for an m-dimensional space then any m-dimensional vector can be expressed uniquely as a linear combination of the columns of **Y** and **Z**. The m-dimensional vector $\mathbf{K}^{1/2}\mathbf{s}$ can thus be expressed in terms of the unknowns **y** and **z**

$$\mathbf{K}^{1/2}\mathbf{s}=\mathbf{Y}\mathbf{y}+\mathbf{Z}\mathbf{z}. \tag{B.6}$$

The second row of Equation (B.3) can be written

$$(\mathbf{A}^T\mathbf{K}^{-1/2})(\mathbf{K}^{1/2}\mathbf{s})=\mathbf{f}. \tag{B.7}$$

Substituting Equations (B.5) and (B.6) results in

$$\mathbf{R}^T\mathbf{y}=\Pi^T\mathbf{f}. \tag{B.8}$$

**y** is easily determined since $\mathbf{R}^T$ is lower triangular. The first row of Equation (B.3) is multiplied by $\mathbf{K}^{-1/2}$ to obtain

$$\mathbf{K}^{1/2}\mathbf{s}+\mathbf{K}^{-1/2}\mathbf{A}\mathbf{t}=\mathbf{K}^{-1/2}\mathbf{g}. \tag{B.9}$$

Multiplying by $\mathbf{Z}^T$ results in

$$\mathbf{z}=\mathbf{Z}^T\mathbf{K}^{-1/2}\mathbf{g}, \tag{B.10}$$

which easily obtains **z**. Then **s** can be calculated from Equation (B.6). Multiplying Equation (B.9) by $\mathbf{Y}^T$ results in

$$[\mathbf{R}\ \ \mathbf{M}]\Pi^T\mathbf{t}=\mathbf{Y}^T\mathbf{K}^{-1/2}\mathbf{g}-\mathbf{y}. \tag{B.11}$$

Let $[\mathbf{v}^T\ \mathbf{m}^T] = \Pi^T\mathbf{t}$. Since **m** is the vector of coefficients of any modes that exist due to rank deficiency of **A**, the modes can be eliminated by choosing $\mathbf{m} = \mathbf{0}$ and

$$\mathbf{R}\mathbf{v}=\mathbf{Y}^T\mathbf{K}^{-1/2}\mathbf{g}-\mathbf{y}, \tag{B.12}$$

and

$$\mathbf{t}=\Pi\begin{bmatrix}\mathbf{v}\\ \mathbf{0}\end{bmatrix}. \tag{B.13}$$

Solving for **v** only requires a back substitution.

Since **A** is sparse, Givens rotations are particularly attractive for performing the QR decomposition. Let the Givens rotations be numbered $\mathbf{J}_1,\ldots,\mathbf{J}_n$ in the order they are performed. Then

$$\mathbf{P}\mathbf{J}_n\cdots\mathbf{J}_1=\mathbf{P}\mathbf{Q}^T=\begin{bmatrix}\mathbf{Y}^T\\ \mathbf{Z}^T\end{bmatrix}^T, \tag{B.14}$$

and

$$\mathbf{J}_1^T\cdots\mathbf{J}_n^T\mathbf{P}^T=\mathbf{Q}\mathbf{P}^T=\begin{bmatrix}\mathbf{Y} & \mathbf{Z}\end{bmatrix}. \tag{B.15}$$

Then Equation (B.15) is used to compute Equation (B.6) and Equations (B.10) and (B.11) are computed using Equation (B.14). Therefore, it is never necessary to form **Q**.

The efficiency of the direct solver is dependent on the efficiency of the sparse QR decomposition. While the final structure of **R** is solely dependent on the column ordering, both the row and column ordering impact the amount of computation required to obtain the QR decomposition. A general purpose sparse QR solver is used with a minimum degree column ordering and a variable pair row ordering scheme (Robey and Sulsky, 1994). A problem-specific nested dissection or nested domain decomposition column ordering would probably be more efficient but will require more programming.

# Appendix C: RIB/GENISES Information

Information from the Reference Information Base
Used in this Report

This report contains no information from the Reference Information Base.

Candidate Information
for the
Reference Information Base

This report contains no candidate information for the Reference Information Base.

Candidate Information
for the
Geographic Nodal Information Study
and Evaluation System

This report contains no candidate information for the Geographic Nodal Information Study and Evaluation System.

# References

Atkinson, K. E., 1978, *An Introduction to Numerical Analysis*, John Wiley & Sons, New York, pp. 231-243. (MOL.19940714.0116)

Babuška, I., 1974, "Error Bounds for Finite Element Method," *Numerische Mathematik*, 16, pp. 322-333. (NNA.940629.0002)

Barnard, R. W. and H. A. Dockery, editors, 1991, "Technical Summary of the Performance Assessment Calculational Exercises for 1990 (PACE-90), Volume 1: 'Nominal Configuration' Hydrogeologic Parameters and Calculational Results," *SAND90-2726*, Sandia National Laboratories, Albuquerque, NM. (NNA.910523.0001)

Benjamin, J. R., and C. A. Cornell, 1970, *Probability, Statistics and Decision for Civil Engineers*, McGraw-Hill, Inc., New York. (NNA.890906.0197)

Brezzi, F., 1974, "On the Existence, Uniqueness and Approximation of Saddle-Point Problems Arising From Lagrangian Multipliers," *R.A.I.R.O. Anal. Numer.*, 8, pp. 129-151. (NNA.940203.0005)

Brooks, R. H. and A. T. Corey, 1966, "Properties of Porous Media Affecting Fluid Flow," *Journal of the Irrigation and Drainage Division, Proceedings of the American Society of Civil Engineers*, IR2, pp. 61-88. (NNA.870407.0356)

Das, B., S. Steinberg, D. Zhang and T. Robey, 1994, "Comparison of Numerical Solution Methods for Differential Equations with Discontinuous Coefficients," *Mathematics and Computers in Simulation*, 36, pp. 57-75. (NNA.940607.0147)

Dennis, J. E., Jr., and R. B. Schnabel, 1983, *Numerical Methods for Unconstrained Optimization and Nonlinear Equations*, Prentice-Hall, Inc., Englewood Cliffs, NJ. (NNA.900702.0003)

Deutsch, C. V., and A. G. Journel, 1992, *GSLIB: Geostatistical Software Library and User's Guide*, Oxford University Press, New York. (NNA.930507.0081)

Dudley, A. L., R. R. Peters, J. H. Gauthier, M. L. Wilson, M. S. Tierney, and E. A. Klavetter, 1988, "Total System Performance Assessment Code (TOSPAC) Volume 1: Physical and Mathematical Bases," *SAND85-0002*, Sandia National Laboratories, Albuquerque, NM. (NNA.881202.0211)

Eaton, R. R., 1993, "The Appropriateness of One-Dimensional Yucca Mountain Hydrologic Calculations," *SAND93-0852*, Sandia National Laboratories, Albuquerque, NM. (NNA.930930.0068)

Ewing, R. E., J. V. Koebbi, R. Gonzalez, and M. F. Wheeler, 1983, "Computing Accurate Velocities for Fluid Flow in Porous Media," *Proceedings of TICOM Conference*, Austin TX, pp. 131-136. (MOL.19941020.0001)

Fletcher, R., 1976, "Conjugate Gradient Methods for Indefinite Systems," *Lecture Notes in Mathematics 506*, Springer-Verlag, Berlin. (NNA.940203.0008)

Flint, L. E., and A. L. Flint, 1990, "Preliminary Permeability and Water-Retention Data for Nonwelded and Bedded Tuff Samples, Yucca Mountain Area, Nye County, Nevada," *USGS-OFR-90-569*, U.S. Geological Survey, Denver, CO. (NNA.920225.0002)

Fraeijs de Veubeke, B., 1965, "Displacement and Equilibrium Models in the Finite Element Method," *Stress Analysis*, O. C. Zienkiewicz and G. S. Holister, eds., Wiley, New York, pp. 145-197. (NNA.940203.0009)

Gauthier, J. H., M. L. Wilson, and F. C. Lauffer, 1992, "Estimating the Consequences of Significant Fracture Flow at Yucca Mountain," *High-Level Radioactive Waste Management, Proceedings of the Third International Conference*, pp. 891-898. (NNA.920505.0068)

Golub, G. H., and C. F. Van Loan, 1983, *Matrix Computations*, The Johns Hopkins University Press, Baltimore, MD, pp. 136-188. (NNA.940620.0014)

Heath, M. T., 1976, *Numerical Algorithms for Nonlinearly Constrained Optimization*, Ph.D. Dissertation, Stanford University, Palo Alto, CA. (NNA.940323.0002)

Istok, J. D., A. L. Flint, and L. E. Flint, 1991, "Spatial Variability in Rock Matrix Properties from Surface Outcrop Sampling," *Agronomy Abstracts, Crop Science Society of America, Soil Science Society America*, pp. 222-223. (NNA.920707.0067)

Journel, A. G., and F. Alabert, 1989, "Non-Gaussian Data Expansion in the Earth Sciences," *Terra Nova*, 1, pp. 123-134. (NNA.891208.0051)

Kaasschieter, E. F. and A. J. M. Huijben, 1992, "Mixed-Hybrid Finite Elements and Streamline Computation for the Potential Flow Problem," *Numerical Methods for Partial Differential Equations*, 8, pp. 221-266. (NNA.930125.0073)

Ladyzhenskaya, O. -A., 1969, *The Mathematical Theory of Viscous Flow*, (English Translation of Russian, 2nd Edition), Gordon and Breach, New York. (MOL.19940718.0027)

Kaplan, P. G., 1993, "Pre-Waste-Emplacement Ground-Water Travel Time Sensitivity and Uncertainty Analyses for Yucca Mountain, Nevada," *SAND92-0461*, Sandia National Laboratories, Albuquerque, NM. (NNA.921216.0009)

Kaplan, P. G., E. A. Klavetter, and R. R. Peters, 1989, "Approaches to Groundwater Travel Time," *Proceedings of Waste Management '89*, University of Arizona, Tucson, pp. 493-495. (NNA.920609.0028)

Klavetter, E. A., and R. R. Peters, 1986, "Estimation of Hydrologic Properties of an Unsaturated, Fractured Rock Mass," *SAND84-2642*, Sandia National Laboratories, Albuquerque, NM. (NNA.870317.0738)

Klavetter, E. A., and R. R. Peters, 1987, "An Evaluation of the Use of Mercury Porosimetry in Calculating Hydrologic Properties of Tuffs from Yucca Mountain, Nevada," *SAND86-0286*, Sandia National Laboratories, Albuquerque, NM. (NNA.890327.0056)

Molenaar, H., 1992, *Multigrid Methods for Semiconductor Device Simulation*, Academisch Proefschrift, Centrum voor Wiskunde en Informatica, Amsterdam. (NNA.940203.0041)

Morel, J. E. , J. E. Dendy, M. L. Hall, and S. W. White, 1990, "A Cell-Centered Lagrangian-Mesh Diffusion Differencing Scheme," *LA-UR-90-3582*, Los Alamos National Laboratory, Los Alamos, NM. (NNA.930125.0075)

Mualem, Y., 1976, "A New Model for Predicting the Hydraulic Conductivity of Unsaturated Porous Materials," *Water Resources Research*, 12, pp. 513-522. (NNA.890522.0250)

Nitao, J. J. and T. A. Buscheck, 1991, "Infiltration of a Liquid Front in an Unsaturated, Fractured Porous Medium," *Water Resources Research*, 27, pp. 2099-2112. (NNA.920817.0138)

Nuclear Regulatory Commission (NRC), 1983, "Disposal of High-Level Radioactive Wastes in Geologic Repositories," *Code of Federal Regulations*, Title 10, Part 60, pp. 28194-28220. (NNA.900727.0307)

Oden, J. T., 1979, *Applied Functional Analysis, A First Course for Students of Mechanics and Engineering Science*, Prentice-Hall, Inc., Englewood Cliffs, NJ, pp. 321-330. (MOL.19940714.0117)

Peters, R. R. and E. A. Klavetter, 1988, "A Continuum Model for Water Movement in an Unsaturated Fractured Rock Mass," *Water Resources Research*, 24, pp. 416-430. (NNA.890523.0139)

Peters, R. R., E. A. Klavetter, I. J. Hall, S. C. Blair, P. R. Heller, and G. W. Gee, 1984, "Fracture and Matrix Hydrologic Characteristics of Tuffaceous Materials from Yucca Mountain, Nye County, Nevada," *SAND84-1471*, Sandia National Laboratories, Albuquerque, NM. (NNA.870407.0036)

Popov, E. P., 1976, *Mechanics of Materials, Second Edition*, Prentice-Hall, Inc., Englewood Cliffs, NJ, pp. 126-130. (MOL.19940718.0026)

Press, W. H., B. P. Flannery, S. A. Teukolsky, and W. T. Vetterling, 1988, *Numerical Recipes in C*, Cambridge University Press, Cambridge. (NNA.930125.0077)

Prindle, R., and P. Hopkins, 1990, "On Conditions and Parameters Important to Model Senstitivity for Unsaturated Flow Through Layered, Fractured Tuff: Results of Analyses for HYDROCOIN Level 3, Case 2," *SAND89-0652*, Sandia National Laboratories, Albuquerque, NM. (NNA.900523.0211)

Rautman, C. A., J. D. Istok, A. L. Flint, L. E. Flint, and M. P. Chornack, 1993, "Influence of Deterministic Geologic Trends on Spatial Variability of Hydrologic Properties in Volcanic Tuff," *High-Level Radioactive Waste Management, Proceedings of the Fourth International Conference*, pp. 921-929. (NNA.930702.0012)

Rautman, C. A., and A. L. Flint, 1992, "Deterministic Geologic Processes and Stochastic Modeling," *High-Level Radioactive Waste Management, Proceedings of the Third International Conference*, pp. 1617-1624. (NNA.920505.0069)

Raviart, P. -A., and J. -M. Thomas, 1977, "A Mixed Finite Element Method for Second Order Elliptic Problems," *Mathematical Aspects of Finite Element Methods*, I. Galligani and E. Magenes, eds., Lecture Notes in Mathematics 606, Springer-Verlag, Berlin, pp. 292-315. (MOL.19940718.0028)

Roberts, J. E., and J. -M. Thomas, 1990, "Mixed and Hybrid Methods," *Handbook of Numerical Analysis, Volume II: Finite Element Methods*, P. G. Ciarlet and J. L. Lions, eds., North-Holland, Amsterdam, pp. 523-639. (NNA.940303.0055)

Robey, T. H., 1990, *The Mixed Finite Element Method*, Ph.D. Dissertation, University of New Mexico, Albuquerque, NM. (NNA.930125.0074)

Robey, T. H., 1992, "The Primal Mixed Finite Element Method", *Numerical Methods for Partial Differential Equations*, 8, pp. 357-379. (NNA.940303.0033)

Robey, T. H. and D. L. Sulsky, 1994, "Row Ordering for a Sparse QR Decomposition", *SIAM Journal on Matrix Analysis and Applications*, 15, pp. 1208-1225. (NNA.940203.0045)

Rush, F. E., W. Thordarson, and L. Bruckheimer, 1983, "Geologic and Drill-hole Data for Test Well USW H-1, Adjacent to the Nevada Test Site, Nye County, Nevada," *USGS-OFR-83-141*, U.S. Geological Survey, Reston, VA. (NNA.870519.0103)

Rutherford, B. M., I. J. Hall, R. R. Peters, R. G. Easterling, and E. A. Klavetter, 1992, "Statistical Analysis of Hydrologic Data for Yucca Mountain," *SAND87-2380*, Sandia National Laboratories, Albuquerque, NM. (NNA.910822.0001)

Schenker, A. R., D. C. Guerin, T. H. Robey, C. A. Rautman, and R. W. Barnard, 1994, "Stochastic Hydrogeologic Units and Hydrogeologic Properties Development for Total System Performance Assessments," *SAND94-0244*, Sandia National Laboratories, Albuquerque, NM. (NNA.940204.0199)

Steinberg, S., and P. J. Roache, 1985, "Variational Grid Generation," *Numerical Methods for Partial Differential Equations*, 2, pp. 71-96. (NNA.940607.0148)

Stoker, A. K., W. D. Purtymun, S. G. McLin, and M. N. Maes, 1991, "Extent of Saturation in Mortandad Canyon," *LA-UR-91-1660*, Los Alamos National Laboratory, Los Alamos, NM. (NNA.930125.0076)

Swedish Nuclear Inspectorate, 1992, *INTRAVAL Progress Report Number 9*, Stockholm, Sweden. (NNA.940203.0042)

van der Vorst, H. A., 1992, "Bi-CGSTAB: A Fast and Smoothly Converging Variant of Bi-CG for the Solution of Nonsymmetric Linear Systems," *SIAM Journal of Scientific and Statistical Computing*, 13, pp. 631-644. (NNA.930614.0258)

van Genuchten, R., 1978, "Calculating the Unsaturated Hydraulic Conductivity with a New Closed Form Analytical Model," *Water Resources Bulletin*, Princeton University Press, Princeton University, Princeton, NJ. (HQS.880517.1859)

Voss, C., 1992a, *Data Set #1, Yucca Mountain Test Case, INTRAVAL*, Golder Associates, Inc., Redmond, WA. (NNA.940113.0033)

Voss, C., 1992b, *Data Set #2, Yucca Mountain Test Case, INTRAVAL*, Golder Associates, Inc., Redmond, WA. (MOL.19941021.0001)

Voss, C., 1993a, *Data Set #3, Yucca Mountain Test Case, INTRAVAL*, Golder Associates, Inc., Redmond, WA. (MOL.19941021.0002)

Voss, C., 1993b, *Data Set #4, Yucca Mountain Test Case, INTRAVAL*, Golder Associates, Inc., Redmond, WA. (MOL.19941021.0003)

Voss, C., 1993c, *Final Data Set, Yucca Mountain Test Case, INTRAVAL*, Golder Associates, Inc., Redmond, WA. (MOL.19941021.0004)

Warren, J. E., and H. S. Price, "Flow in Heterogeneous Media," *Society of Petroleum Engineering Journal*, 1, pp. 153-169. (HQZ.870228.2033)

Wilson, M. L., J. H. Gauthier, R. W. Barnard, G. E. Barr, H. A. Dockery, E. Dunn, R. R. Eaton, D. C. Guerin, N. Lu, M. J. Martinez, R. Nilson, C. A. Rautman, T. H. Robey, B. Ross, E. E. Ryder, A. R. Schenker, S. A. Shannon, L. H. Skinner, W. G. Halsey, J. Gansemer, L. C. Lewis, A. D. Lamont, I. R. Triay, A. Meijer, and D. E. Morris, 1994, "Total-System Performance Assessment for Yucca Mountain -- SNL Second Iteration (TSPA-1993)," *SAND93-2675*, Sandia National Laboratories, Albuquerque, NM. (NNA.940112.0123)

Yang, I. C., A. K. Turner, T. M. Sayre, and P. Montazer, 1988, "Triaxial Compression Extraction of Pore Water from Unsaturated Tuff, Yucca Mountain, Nevada," *USGS/WRIR-88-4189*, U.S. Geological Survey, Denver, CO. (NNA.890309.0161)

# Yucca Mountain Site Characterization Project

# Distribution List

1 D.A. Dreyfus (RW-1)
Director
OCRWM
US Department of Energy
1000 Independence Avenue SW
Washington, DC 20585

1 L.H. Barrett (RW-2)
Acting Deputy Director
OCRWM
US Department of Energy
1000 Independence Avenue SW
Washington, DC 20585

1 J.D. Saltzman (RW-4)
Office of Strategic Planning and International Programs
OCRWM
US Department of Energy
1000 Independence Avenue SW
Washington, DC 20585

1 J.D. Saltzman (RW-5)
Office of External Relations
OCRWM
US Department of Energy
1000 Independence Avenue SW
Washington, DC 20585

1 Samuel Rousso (RW-10)
Office of Program and Resource Mgt.
OCRWM
US Department of Energy
1000 Independence Avenue SW
Washington, DC 20585

1 J. C. Bresee (RW-10)
OCRWM
US Department of Energy
1000 Independence Avenue SW
Washington, DC 20585

1 R.M. Nelson (RW-20)
Office of Geologic Disposal
OCRWM
US Department of Energy
1000 Independence Avenue, SW
Washington, DC 20585

1 S. J. Brocoum (RW-22)
Analysis and Verification Division
OCRWM
US Department of Energy
1000 Independence Avenue SW
Washington, DC 2585

1 D. Shelor (RW-30)
Office of Systems and Compliance
OCRWM
US Department of Energy
1000 Independence Avenue, SW
Washington, DC 20585

1 J. Roberts (RW-33)
Director, Regulatory Compliance Division
OCRWM
US Department of Energy
1000 Independence Avenue, SW
Washington, DC 20585

1 G. J. Parker (RW-332)
Reg. Policy/Requirements Branch
OCRWM
US Department of Energy
1000 Independence Avenue, SW
Washington, DC 20585

1 R. A. Milner (RW-40)
Office of Storage and Transportation
OCRWM
US Department of Energy
1000 Independence Avenue, SW
Washington, DC 20585

1 S. Rousso (RW-50)
Office of Contract Business Management
OCRWM
US Department of Energy
1000 Independence Avenue, SW
Washington, DC 20585

1 T. Wood (RW-52)
Director, M&O Management Division
OCRWM
US Department of Energy
1000 Independence Avenue, SW
Washington, DC 20585

4 Victoria F. Reich, Librarian
Nuclear Waste Technical Review Board
1100 Wilson Blvd, Suite 910
Arlington, VA 22209

5 R.M. Nelson Jr, Acting Project Manager
Yucca Mountain Site Characterization Office
US Department of Energy
P.O. Box 98608--MS 523
Las Vegas, NV 89193-8608

1 C. L. West, Director
Office of External Affairs
DOE Nevada Field Office
US Department of Energy
P.O. Box 98518
Las Vegas, NV 89193-8518

8 Technical Information Officer
DOE Nevada Field Office
US Department of Energy
P.O. Box 98518
Las Vegas, NV 89193-8518

1 P. K. Fitzsimmons, Technical Advisor
Office of Assistant Manager for Environmental Safety and Health
DOE Nevada Field Office
US Department of Energy
P.O. Box 98518
Las Vegas, NV 89193-8518

1 D. R. Elle, Director
Environmental Protection and Division
DOE Nevada Field Office
US Department of Energy
P.O. Box 98518
Las Vegas, NV 89193-8518

1 Repository Licensing & Quality Assurance
Project Directorate
Division of Waste Management
US NRC
Washington, DC 20555

1 Senior Project Manager for Yucca Mountain
Repository Project Branch
Division of Waste Management
US NRC
Washington, DC 20555

1 NRC Document Control Desk
Division of Waste Management
US NRC
Washington, DC 20555

1 Philip S. Justus
NRC Site Representive
301 E Stewart Avenue, Room 203
Las Vegas, NV 89101

1 E. P. Binnall
Field Systems Group Leader
Building 50B/4235
Lawrence Berkeley Laboratory
Berkeley, CA 94720

1 Center for Nuclear Waste
Regulatory Analyses
6220 Culebra Road
Drawer 28510
San Antonio, TX 78284

3 W. L. Clarke
Technical Project Officer - YMP
Attn: YMP/LRC
Lawrence Livermore National
Laboratory
P.O. Box 5514
Livermore, CA 94551

1 J. A. Blink
Deputy Project Leader
Lawrence Livermore National
Laboratory
101 Convention Center Drive
Suite 820, MS 527
Las Vegas, NV 89109

4 J. A. Canepa
Technical Project Officer - YMP
N-5, Mail Stop J521
Los Alamos National Laboratory
P.O. Box 1663
Los Alamos, NM 87545

1 H. N. Kalia
Exploratory Shaft Test Manager
Los Alamos National Laboratory
Mail Stop 527
101 Convention Center Dr., #820
Las Vegas, NV 89101

1 N. Z. Elkins
Deputy Technical Project Officer
Los Alamos National Laboratory
Mail Stop 527
101 Convention Center Dr., #820
Las Vegas, NV 89101

5 L. E. Shephard
Technical Project Officer - YMP
Sandia National Laboratories
Organization 6302, M/S 1333
P.O. Box 5800
Albuquerque, NM 87185

1 J. F. Devine
Asst Director of Engineering Geology
US Geological Survey
106 National Center
12201 Sunrise Valley Drive
Reston, VA 22092

1 L. R. Hayes
Technical Project Officer
Yucca Mountain Project Branch
MS 425
US Geological Survey
P.O. Box 25046
Denver, CO 80225

1 V. R. Schneider
Asst. Chief Hydrologist--MS 414
Office of Program Coordination
and Technical Support
US Geological Survey
12201 Sunrise Valley Drive
Reston, VA 22092

1 J. S. Stuckless
Geologic Division Coordinator
MS 913
Yucca Mountain Project
US Geological Survey
P.O. Box 25046
Denver, CO 80225

1 D. H. Appel, Chief
Hydrologic Investigations Program
MS 421
US Geological Survey
P.O. Box 25046
Denver, CO 80225

1 E. J. Helley
Branch of Western Regional Geology
MS 427
US Geological Survey
345 Middlefield Road
Menlo Park, CA 94025

1 R. W. Craig, Chief
Nevada Operations Office
US Geological Survey
101 Convention Center Drive
Suite 860, MS 509
Las Vegas, NV 89109

1 D. Zesiger
US Geological Survey
101 Conventional Center Drive
Suite 860, MS 509
Las Vegas, NV 89109

1 G. L. Ducret, Associate Chief
Yucca Mountain Project Division
US Geological Survey
P.O. Box 25046
421 Federal Center
Denver, CO 80225

1 A. L. Flint
US Geological Survey
MS 721
P.O. Box 327
Mercury, NV 89023

1 D. A. Beck
Water Resources Division, USGS
6770 S Paradise Road
Las Vegas, NV 89119

1 P. A. Glancy
US Geological Survey
Federal Building, Room 224
Carson City, NV 89701

1 Sherman S.C. Wu
US Geological Survey
2255 N. Gemini Drive
Flagstaff, AZ 86001

1 J. H. Sass - USGS
Branch of Tectonophysics
2255 N Gemini Drive
Flagstaff, AZ 86001

1 DeWayne Campbell
Technical Project Officer - YMP
US Bureau of Reclamation
Code D-3790
P.O. Box 25007
Denver, CO 80225

1 J. M. LaMonaca
Records Specialist
US Geological Survey
421 Federal Center
P.O. Box 25046
Denver, CO 80225

1 W. R. Keefer - USGS
913 Federal Center
P.O. Box 25046
Denver, CO 80225

1 M. D. Voegele
Technical Project Officer - YMP
SAIC
101 Convention Center Drive
Suite 407
Las Vegas, NV 89109

2 L. D. Foust
Nevada Site Manager
TRW Environmental Safety Systems
101 Convention Center Drive
Suite 540, MS 423
Las Vegas, NV 89109

1 C. E. Ezra
YMP Support Office Manager
EG&G Energy Measurements Inc
MS V-02
P.O. Box 1912
Las Vegas, NV 89125

1 Jan Docka
Roy F. Weston Inc
955 L'Enfant Plaza SW
Washington, DC 20024

1 Technical Information Center
Roy F. Weston Inc
955 L'Enfant Plaza SW
Washington, DC 20024

1 D. Hedges, Vice President, QA
Roy F. Weston Inc
4425 Spring Mountain Road
Suite 300
Las Vegas, NV 89102

1 D. L. Fraser, General Manager
Reynolds Electrical &
Engineering Co, Inc
MS 555
P.O. Box 98521
Las Vegas, NV 89193-8521

1 B. W. Colston, President and
General Manager
Las Vegas Branch
Raytheon Services Nevada
MS 416
P.O. Box 95487
Las Vegas, NV 89193-5487

1 R. L. Bullock
Technical Project Officer - YMP
Raytheon Services Nevada
Suite P-250, MS 403
101 Convention Center Drive
Las Vegas, NV 89109

1 Paul Eslinger, Manager
PASS Program
Pacific Northwest Laboratories
P.O. Box 999
Richland, WA 99352

1 A. T. Tamura
Science and Technology Division
OSTI
US Department of Energy
P.O. Box 62
Oak Ridge, TN 37831

1 Carlos G. Bell Jr
Professor of Civil Engineering
Civil and Mechanical Engineering
Dept.
University of Nevada, Las Vegas
4505 S Maryland Parkway
Las Vegas, NV 89154

1 P. J. Weeden, Acting Director
Nuclear Radiation Assessment Div.
US EPA
Environmental Monitoring
Systems Lab
P.O. Box 93478
Las Vegas, NV 89193-3478

1 ONWI Library
Battelle Columbus Laboratory
Office of Nuclear Waste Isolation
505 King Avenue
Columbus, OH 43201

1 T. Hay, Executive Assistant
Office of the Governor
State of Nevada
Capitol Complex
Carson City, NV 89710

3 R. R. Loux
Executive Director
Agency for Nuclear Projects
State of Nevada
Evergreen Center, Suite 252
1802 N. Carson Street
Carson City, NV 89710

1 C.H. Johnson
Technical Program Manager
Agency for Nuclear Projects
State of Nevada
Evergreen Center, Suite 252
1802 N. Carson Street
Carson City, NV 89710

1 John Fordham
Water Resources Center
Desert Research Institute
P.O. Box 60220
Reno, NV 89506

1 David Rhode
Desert Research Institute
P.O. Box 60220
Reno, NV 89506

1 Eric Anderson
Mountain West Research-
Southwest Inc
2901 N Central Avenue #1000
Phoenix, AZ 85012-2730

1 The Honorable Cyril Schank
Chairman
Churchill County Board of
Commissioners
190 W First Street
Fallon, NV 89406

1 Dennis Bechtel, Coordinator
Nuclear Waste Division
Clark County Department of
Comprehensive Planning
301 E Clark Avenue, Suite 570
Las Vegas, NV 89101

1 Juanita D. Hoffman
Nuclear Waste Repository
Oversight Program
Esmeralda County
P.O. Box 490
Goldfield, NV 89013

1 Eureka County Board of
Commissioners
Yucca Mountain Information
Office
P.O. Box 714
Eureka, NV 89316

1 Brad Mettam
Inyo County Yucca Mountain
Repository Assessment Office
Drawer L
Independence, CA 93526

1 Lander County Board of
Commissioners
315 South Humbolt
Battle Mountain, NV 89820

1 Vernon E. Poe
Office of Nuclear Projects
Mineral County
P.O. Box 1026
Hawthorne, NV 89415

1 Les W. Bradshaw
Program Manager
Nye County Repository
P.O. Box 429
Tonopah, NV 89049

1 Florindo Mariani
White Pine County Nuclear
Waste Project Office
457 Fifth Street
Ely, NV 89301

1 Judy Foremaster
City of Caliente Nuclear Waste
Project Office
P.O. Box 158
Caliente, NV 89008

1 Phillip A. Niedzielski-Eichner
Nye County Nuclear Waste
Repository Project Office
P.O. Box 221274
Chantilly, VA 22022-1274

1 Jason Pitts
Lincoln County Nuclear Waste
Project Office
Lincoln County Courthouse
Pioche, NV 89043

1 Economic Development Dept.
City of Las Vegas
400 E. Stewart Avenue
Las Vegas, NV 89101

1 Commmunity Planning and
Development
City of North Las Vegas
P.O. Box 4086
North Las Vegas, NV 89030

1 Community Development and
Planning
City of Boulder City
P.O. Box 61350
Boulder City, NV 89006

1 Commission of the European
Communities
200 Rue de la Loi
B-1049 Brussells
BELGIUM

2 M. J. Dorsey, Librarian
YMP Research and Study Center
Reynolds Electrical &
Engineering Co Inc
MS 407
P.O. Box 98521
Las Vegas, NV 89193-8521

1 Amy Anderson
Argonne National Laboratory
Building 362
9700 S Cass Avenue
Argonne, IL 60439

1 Steve Bradhurst
P.O. Box 1510
Reno, NV 89505

1 Michael L. Baughman
35 Clark Road
Fiskdale, MA 01518

1 Glenn Van Roekel
Director of Community
Development
City of Caliente
P.O. Box 158
Caliente, NV 89008

1 Ray Williams, Jr
P.O. Box 10
Austin, NV 89310

1 Nye County District Attorney
P.O. Box 593
Tonopah, NV 89049

1 William Offutt
Nye County Manager
Tonopah, NV 89049

1 Charles Thistlethwaite, AICP
Associate Planner
Inyo County Planning Department
Drawer L
Independence, CA 93526

1 R. F. Pritchett
Technical Project Officer - YMP
Reynolds Electrical &
Engineering Company Inc
MS 408
P.O. Box 98521
Las Vegas, NV 89193-8521

1 Dr. Moses Karakouzian
1751 E Reno #125
Las Vegas, NV 89119

5 Dr. Thomas Robey
Spectra Research Institute
1613 University Blvd, NE
Albuquerque, NM 87102

1 J. H. Gauthier
Spectra Research Institute
1613 University Blvd, NE
Albuquerque, NM 87102

1 Alan Dudley
Spectra Research Institute
1613 University Blvd, NE
Albuquerque, NM 87102

| | MS | |
|---|---|---|
| 1 | 1325 | L.S. Costin, 6313 |
| 2 | 1330 | G.M. Gerstner-Miller, 6352<br>100/12544/SAND93-7109/QA |
| 20 | 1330 | WMT Library, 6352 |
| 1 | 1324 | P.B. Davies, 6115 |
| 1 | 0827 | P.J. Hommert, 1502 |
| 1 | 1375 | D.A. Dahlgren, 4400 |
| 1 | 1326 | H.A. Dockery, 6312 |
| 5 | 0899 | Technical Library, 13414 |
| 1 | 0619 | Technical Publications, 13416 |
| 10 | 0100 | Document Processing for<br>DOE/OSTI, 7613-2 |
| 1 | 9018 | Central Technical Files, 8523-2 |



*U.SGOVERNMENT PRINTING OFFICE 1994-0-673-031/00024